Control System Development for a Gastric Retention and Injection Device for Autonomous Urgent Care Therapy

Halithan Çetin

May 9, 2023

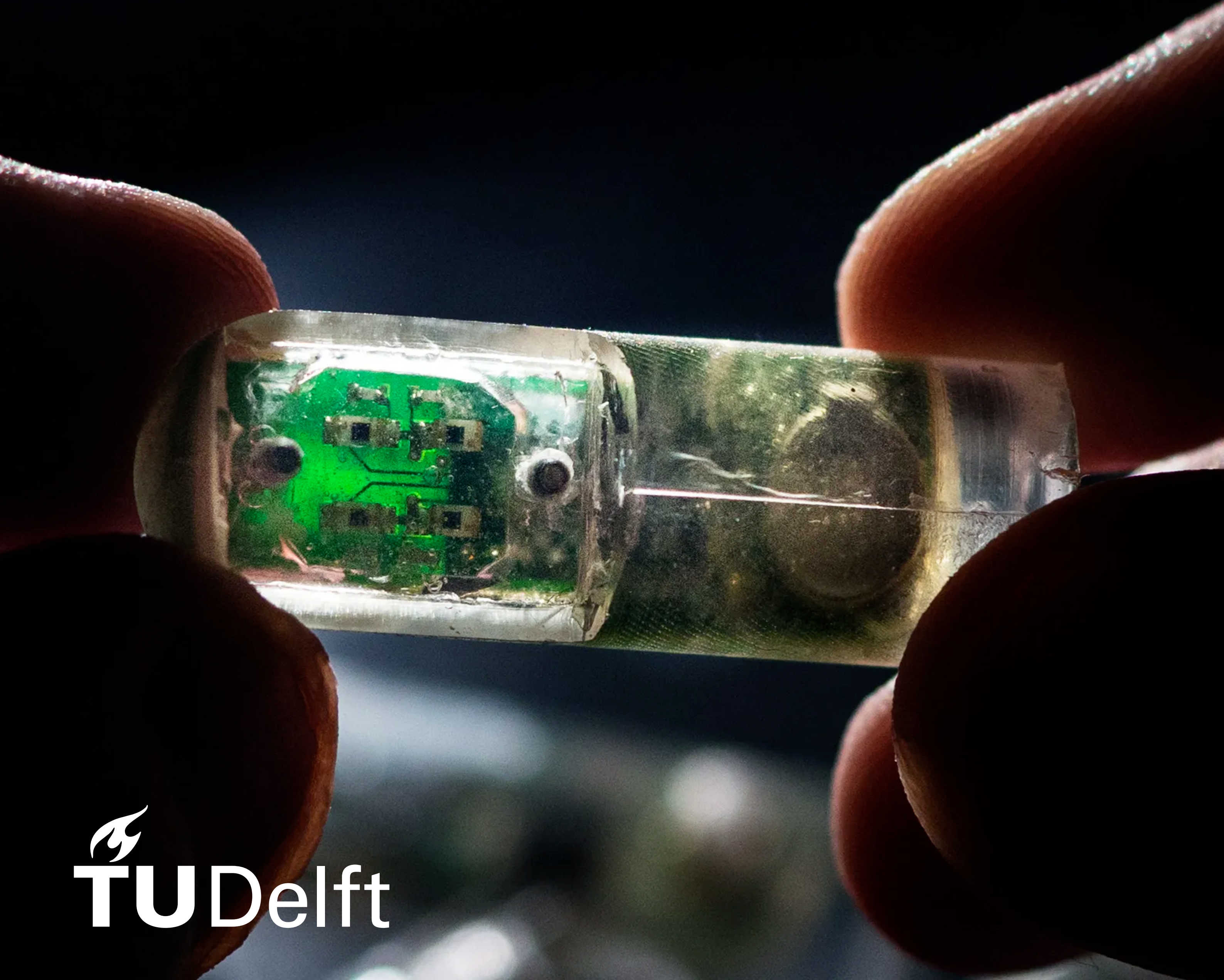

Cover: Ingestible electronic device by Lillie Paquette, MIT (Modified)

Control System Development for a Gastric Retention and Injection Device for Autonomous Urgent Care Therapy

MASTER OF SCIENCE THESIS

Halithan Çetin

May 9, 2023

Faculty of Faculty of Mechanical, Maritime and Materials Engineering (3mE) · Delft
University of Technology

Daily Supervisor MIT:	H.W. Huang, PhD
Supervisor TU Delft:	M. Mazo, PhD
Supervisor TU Delft:	S. Pequito, PhD
Medical-side Assistance MIT:	James D. Byrne, MD, PhD
Principal Investigator MIT:	C.G. Traverso, MD, PhD, MBBCH

TU Delft Delft University of Technology

BWH BRIGHAM AND WOMEN'S HOSPITAL

HARVARD MEDICAL SCHOOL

Massachusetts Institute of Technology

Abstract

Time-sensitive medical emergencies resulting from the entry of harmful agents into the body require immediate and urgent medical attention to prevent irreversible symptoms or fatalities. However, the current process for urgent care relies on human intervention, which can introduce significant delays and potentially compromise the effectiveness of treatment. Recent advancements in harmful agent detection sensors and ingestible device technology present an opportunity to explore the development of an ingestible device that can autonomously detect and immediately treat medical emergencies caused by harmful agents.

The concept of an autonomous device for urgent care therapy necessitates a system that can achieve gastric retention and facilitate on-demand delivery of macromolecule drugs. Despite numerous proposals for gastric residence and macromolecule drug delivery systems, their controllability capabilities fall short. One of the primary challenges is ensuring the correct orientation of the device for effective injection into the stomach wall. Researchers have developed an ingestible device guided by a microactuator, designed for gastric retention and injection. However, the current prototype of the device lacks a control system, essentially being a body without a brain.

This thesis delves into the design and implementation of a control system for an urgent care therapy device. The proposed control system is designed by individually examining the sensor system, the actuator system, and the decision making system. The viability of the proposed control system is demonstrated using the example of gamma radiation poisoning. The system integrates three distinct sensors: a harmful agent sensor, a power monitor, and an inertial measurement unit (IMU). The collected data is fed into the decision making system, which is capable of detecting the urgent care condition, battery depletion, and device misorientation. If the urgent care therapy need has been confirmed, the actuator control system will steer the device to correct its orientation and trigger the injection of the macromolecule drug into the stomach wall.

The proposed system provides orientation estimation with an accuracy of 2 degrees and features an adaptable sensor and needle system, enhancing its adaptability across various applications. The device's battery life extends up to 19 days, underscoring its potential as a viable autonomous tool for urgent care therapy. This research concludes that the proposed autonomous urgent care therapy device is a feasible solution in the treatment of time-sensitive medical emergencies resulting from the entry of harmful agents into the body, complementing existing healthcare strategies.

Contents

List of Figures

List of Tables

Preface and Acknowledgements

As I complete this thesis, I also conclude my time at TU Delft. The past years have been incredible, and looking back, I can truly say that I have grown as a student, engineer, and person. I am grateful for the opportunities Delft has provided me. The possibilities often seemed endless as the university expanded far beyond the campus. From my first year working on cars with flywheels for energy conservation to progressing toward modeling and scientific engineering, I've enjoyed numerous responsibilities. Through extracurricular activities, I've been able to organize memorable events and make lasting friendships. As the cherry on top, I even had the opportunity to spend a year abroad in Boston.

My year in Boston began during the COVID pandemic, shortly after the borders reopened, marking my first time outside Europe and studying abroad. In my first week, I was captivated by the city while strolling alongside the frozen Charles River. Boston's beauty and vibrant community were truly inspiring. I quickly realized the uniqueness of MIT and Harvard.

Thank you, Henwei, for granting me this opportunity. Before this year, I didn't even know how to solder a chip, but through your guidance, I've developed a strong passion for electrical engineering and robotics. Medical engineering has always been an interest of mine, and you provided me with the chance to contribute to the development of novel devices.

Thank you, Sergio and Manuel, for guiding me throughout the thesis process. Your mentorship elevated my work and, after a gap year during COVID, reminded me how to apply my control engineering knowledge to create an impact in device development. Your patience and dedication not only improved my research but also helped me grow as a researcher.

Thank you, Giovanni, for creating the lab that made all of this possible. This lab brings together students from various disciplines worldwide, allowing me to meet an amazing group of colleagues and lifelong friends. I sincerely appreciate the lab events you hosted to make us feel at home.

Special thanks to my colleagues from the ingestible device team: P. Fritz for the mechanical aspects, D. Werder for the electrical aspects, and C. McLymore for the gamma radiation aspects. Also, a shout out to all the other lab members, the Dimick Street, Hacking Medicine, the E-Club, and VISTA who made my time in Boston unforgettable.

To the financial contributors—the Dutch2USA, the Vreedefonds, Schuurman Schimmel van Outeren Stichting, and Fundatie van Renswoude—I extend my gratitude. As a first-generation student, I never expected to travel this far, this long, and this early in life. Visiting the United States had been a long-held dream of mine. Thank you for placing your trust in me and making this dream a reality.

Lastly, I would like to thank my family back home. Being abroad for the first time was challenging, especially with the many unforeseen events that occurred during that year. Mom, Dad, Ada, Hans, and Janne, your support helped me through it all.

Rotterdam, The Netherlands
May 9, 2023

Halithan Çetin

Chapter 1

Introduction

This chapter serves as an introduction to the thesis topic and the structure of the thesis report. To start, Section 1-1 provides the necessary background information on the research topic. Next, Section 1-2 summarizes the background information to formulate a concise research motivation. Finally, Section 1-3 provides an overview of the structure of the thesis report.

1-1 Advancing Urgent Care with Autonomous Ingestible Devices: Challenges and Future Directions

To contextualize our research, we first describe the challenges of time-sensitive emergency conditions. In an attempt to overcome these challenges, we continue by proposing a device for autonomous detection and drug delivery. Lastly, we focus on *ingestible* devices for autonomous detection and drug delivery, where we explore current research efforts in the field of ingestible devices and how they can serve as autonomous urgent care therapy devices.

1-1-1 Urgent Care for Time-Sensitive Emergencies

Time-sensitive emergencies resulting from the entry of harmful agents into the body, such as severe allergic reactions [1], food poisoning [2], radiation poisoning [3], and opioid overdose [4], demand prompt and urgent medical attention. These examples illustrate that rapid administration of an appropriate antidote or symptom suppressor is critical to prevent irreversible symptoms or fatalities. Yet, the existing process for urgent care entails multiple steps that may result in considerable delays or even preclude treatment altogether.

From the onset of the illness to the final diagnosis and treatment, several stages require human intervention and coordination, leading to bottlenecks and possible errors. Recognizing the need for urgent care therapy typically occurs only after the illness has progressed to the point of producing symptoms. Underestimation of these symptoms or patient unwillingness to receive treatment can further delay the treatment process. Typically, the correct diagnosis and application of the right treatment heavily depend on the medical expertise of the patient. In some cases, such as when the patient is unconscious or in shock, a bystander must recognize the need for treatment. If the patient or bystander is unable to diagnose and provide the treatment themselves, the patient will generally require a visit to the emergency department (ED) of a hospital.

1-1-2 Exploring the Potential of Autonomous Systems for Urgent Care Therapy

The challenges associated with human intervention and coordination in urgent care situations highlight the need for automated solutions. A device capable of detecting the onset of an illness and autonomously providing treatment could address the need for early patient intervention and bridge the gap until more appropriate healthcare can be accessed. Such a device would be particularly useful in extreme situations, such as military or highly remote environments, where appropriate self-care, bystander assistance, and/or access to medical facilities may not be possible. Furthermore, individuals with chronic medical conditions requiring immediate treatment in emergency situations could greatly benefit from such a device.

Autonomous treatment systems have already been proven successful in the medical field in the form of implantable controllable drug delivery devices. These devices are engineered technologies for targeted delivery and controlled release of therapeutic agents, such as closed-loop glucose monitoring devices, also known as "artificial pancreases". For example, Medtronic PLC's Minimed^{TM} 780G has been highly effective in treating type 1 diabetes. The device features a pump that provides automatic insulin delivery based on glucose measurements from an on-body sensor [5]. Systems like these directly measure the agent of interest, in this case glucose, to detect specific episodes and disease profiles.

When we narrow down from autonomous treatment systems to autonomous treatment systems for *urgent care* therapy, we notice that the current systems rely on the measurement of physiological data instead of the direct measurement of the agent of interest. An example of such a device is the seizure-detection wearable from Tang and collaborators [6]. This system uses physiological data, such as body temperature, as a proxy for urgent care detection by monitoring the symptoms most likely to occur during the respective urgent care conditions. One of the main drawbacks of urgent care devices that use detection through physiological data, or a proxy in general, is the potential for misdiagnosis due to similar symptoms with different origins, resulting in the delivery of unwanted medication. Additionally, because of their symptom-based response, they may miss the opportunity to provide treatment at the onset of the condition, when the onset precedes the production of symptoms. Therefore, these devices may not be suitable for conditions that need immediate treatment and are presented through non-specific symptoms.

Although sensors for the direct detection of harmful agents have been developed, no examples of their utilization in autonomous urgent care therapy devices could be found. In the current examples, these sensors are used for monitoring purposes only. Examples of harmful agent detection sensors are sensors for the detection of organophosphates [7], gamma radiation [8], and chemicals related to food poisoning [9]. Integrating these harmful agent detection sensors into autonomous drug delivery devices could offer more targeted and timely treatment options, overcoming the limitations of physiological data-based systems for urgent care therapy.

For the above-mentioned harmful agent sensor systems, direct contact between the harmful agent and the sensor is required. Harmful agents primarily enter the body through the respiratory and digestive systems. Consequently, simple integration of these sensors into current implantable devices is not feasible as these devices are generally implanted into the subcutaneous area and thus are not in direct contact with harmful agents. Moreover, the need for surgical installation makes implantable devices less desirable for short-term use and raises the barrier to widespread adoption due to the requirement for medical expertise and costs associated with implantation [10]. To realize an autonomous urgent care therapy device capable of direct harmful agent detection as well as targeted and timely treatment, we need to incorporate the harmful agent detection sensors into a device located in an area where direct detection is possible. This device should also not require any surgical intervention for use. An ingestible device, which is swallowed by the user and is located in the digestive system, could be a viable option.

1-1-3 Ingestible Devices for Urgent Care Detection and Treatment

Ingestible devices offer a promising platform for urgent care therapy devices due to their non-invasive nature and their location within the patient. By being swallowed and operating from within the gastrointestinal (GI) tract, they enable new opportunities for patient monitoring [11]. The GI tract, illustrated in Figure 1-1, is a series of interconnected hollow organs forming a twisted tube that facilitates ingestion, digestion, and absorption of food and fluids. These organs include the mouth, esophagus, stomach, small intestine, large intestine, rectum, and anus [12].

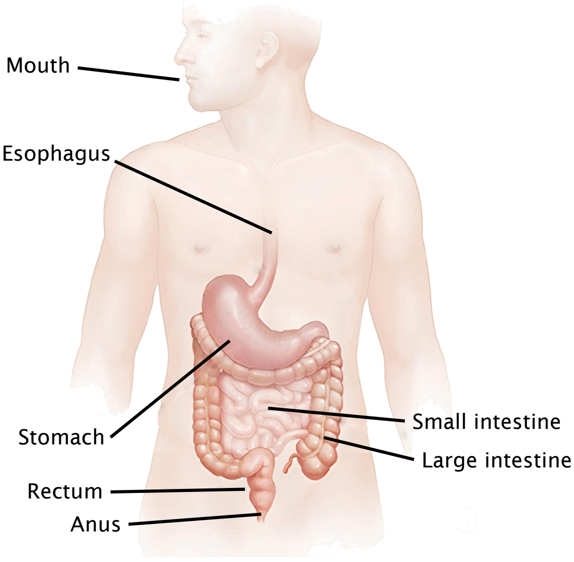

Figure 1-1: Anatomy of the gastrointestinal tract.

The ability of ingestible devices to detect toxins in the gastric region makes them particularly appealing to detect harmful agents. These devices offer the potential for early detection of ingested harmful agents, such as food allergies or organophosphate poisoning [2]. In addition, they can measure the concentration of harmful agents that strongly affect organs near the chest area, such as in cases of radiation exposure [13]. Beyond toxin detection, ingestible devices offer the ability to monitor a range of biomarkers unique to the digestive system, including temperature, gastric activity, pH, and glucose levels [11, 14]. Additionally, the size and shape differences between organs of the GI tract allow for localization of the device within the GI tract, as well as for prolonged residency within certain organs, for example the stomach [15]. These abilities could facilitate patient monitoring as well as localized, long-term monitoring and therapy within the gastric system. Additionally, ingestible devices can monitor more general biomarkers, such as heart rate and respiratory rate [16], which could provide valuable feedback for closed-loop drug delivery.

The therapeutic potential of the GI tract is extensive, encompassing both localized and systemic treatments. An example of localized treatment is the targeted placement of a patch within the intestines to facilitate wound healing, while an example of systemic treatment is drug delivery from within the GI tract for a body-wide impact [17]. Of particular interest is the possibility of delivering macromolecule drugs via the GI tract [18]. Macromolecules, such as proteins, are large-scale molecules that play a crucial role in the treatment of many urgent care conditions. Examples are atropine against organophosphate poisoning [19], sargramostim against radiation poisoning [3], and epinephrine against anaphylaxis [20].

For effective autonomous urgent care therapy, a device should be capable of both direct harmful agent detection and autonomous macromolecule drug delivery. Additionally, to enable long-term operability, the device should be able to remain in (a specific area within) the GI tract. A system that combines these features of monitoring, drug delivery, and retention is currently lacking [21]. The next step in addressing this need is to assess the current state-of-the-art ingestible devices and identify the challenges towards the development of an autonomous urgent care therapy solution. Such a device has the potential to save lives and reduce the burden on healthcare institutions, making it a promising approach in the field of medical technology.

1-2 Research Motivation and Research Context

To summarize Section 1-1, time-sensitive medical emergencies resulting from the entry of harmful agents into the body require immediate and urgent medical attention to prevent irreversible symptoms or fatalities. However, the current process for urgent care heavily depends on human intervention, which can lead to significant delays and potentially compromise the effectiveness of treatment. Recent advancements in harmful agent detection sensors and ingestible device technology present an opportunity to explore the development of an ingestible device to autonomously detect and immediately treat medical emergencies caused by harmful agents. This innovation would not only improve the efficiency and effectiveness of urgent care therapy, but also has the potential to save lives in emergency situations.

In response to this need, the Traverso Lab at Massachusetts Institute of Technology (MIT) and Harvard Medical School (HMS) (from hereon referred to as "the lab") initiated a research initiative to develop an autonomous urgent care therapy device. The lab has already made progress in designing the mechanism of an ingestible system for retention and macromolecule drug delivery. However, the current state of the device can be likened to a body without a brain, lacking a control system to govern its operation.

1-3 Thesis Outline

In this thesis, we will focus on developing the control system, or the "brain," of this autonomous device. We begin by conducting a literature review on autonomous ingestible drug delivery devices in Chapter 2 to gain insights into existing methodologies and challenges. Based on the literature findings, we derive our thesis statement, which outlines the research challenges and objectives that form the basis for subsequent chapters.

In Chapter 3, we introduce the system architecture, setting the stage for the exploration of individual research challenges. Chapter 4 focuses on data processing techniques that transform raw sensor data into usable data for actuator control and decision making. Chapter 5 delves into the development of the actuator control system. Chapter 6 introduces the decision making system that utilizes sensor data to direct the sensing- and actuator system. Chapter 7 consolidates thesis results and reflects on the research objectives. Chapter 8 recognizes limitations, suggests improvements, and proposes future research directions.

Research Contributions of the Team Members and Author

This thesis is a component of a broader research initiative led by the Traverso Lab under the supervision of Dr. Hen-Wei Huang and Dr. James Byrne, MD. The research initiative aims to develop a novel ingestible autonomous urgent care therapy device. To acknowledge the role of the author within the research team, the author's specific contributions will be stated at the beginning of each chapter.

In general, while other team members focused on the physical mechanisms and electrical circuitry, the author focused on the development of the control system. Herein the development of the control system involved conducting hardware benchmarking, designing and developing sensor data processing pipelines, actuator control systems, and decision making systems. The author designed his own custom circuitry for each experimental setup.

In the context of the thesis documentation, Chapter 2, Chapter 4, Chapter 5, and Chapter 6 are exclusively the author's contributions. Chapter 3 outlines the components of the device under consideration and mainly includes collaborative work. All figures, tables, and algorithms presented in this thesis have been created by the author, except where noted in the caption.

Chapter 2

Literature Background and Thesis Statement

Having established the purpose of this thesis, our next goal is to investigate the development of an ingestible autonomous urgent care therapy system. To begin, we examine the current state-of-the-art in this field through a literature review in Section 2-1. This review evaluates the limitations of existing devices, addresses safety concerns associated with the most promising technologies, and identifies design challenges related to the control system.

Drawing from the literature findings, we formulate the thesis statement in Section 2-2. The thesis statement presents the overarching thesis goal and breaks it down into a series of research challenges to be tackled. For each research challenge, we establish a set of design criteria, derived from the literature, which must be met to ensure the feasibility of the proposed system in achieving the overarching thesis goal.

Research Contributions to the Literature Review and Thesis Statement

All content of this chapter is the sole contribution of the author.

2-1 Research Efforts on Ingestible Technology for Autonomous Urgent Care Therapy

The development of an autonomous urgent care therapy device necessitates an ingestible system with long-term gastric residency, the ability to detect harmful agents, and the capacity to deliver macromolecule drugs based on sensor data. As discussed in Chapter 1, detecting harmful agents using ingestible devices is feasible. In this section, we focus on existing closed-loop technologies to better understand the integration of harmful agent detection systems in current devices, paving the way for autonomous urgent care therapy.

To develop an ingestible device for autonomous urgent care therapy, we first examine the current technologies to closed-loop drug delivery in Section 2-1-1. This leads us to further examine current research efforts on gastric retention systems in Section 2-1-2 and ingestible macromolecule drug delivery systems in Section 2-1-3. After identifying the most promising techniques, we delve into the safety concerns of electric ingestible devices in Section 2-1-4 and gastric injection in Section 2-1-5. Finally, we consider general factors influencing patient willingness to adopt ingestible technologies in Section 2-1-6.

At the end of each section, we highlight our main findings in **bold caption**. These main findings form the basis of our thesis statement.

2-1-1 State-of-the-Art Closed-Loop Drug Delivery Devices

Closed-loop drug delivery systems offer targeted and timely drug administration and have been realized in portable formats such as wearable, implantable, and ingestible devices. Since therapy capabilities may differ between formats, we first examine state-of-the-art closed-loop drug delivery devices in general before focusing on ingestible devices specifically.

The Accu-Chek Insight insulin pump serves as an example of a closed-loop drug delivery device for macromolecule drug delivery. The Accu-Chek Insight comprises an insulin pump and a continuous glucose monitoring device that work in tandem to maintain optimal blood glucose levels for patients with diabetes. The continuous glucose monitoring device measures blood glucose levels and transmits the data to the insulin pump, which then administers the appropriate amount of insulin. Although this device is externally worn, it demonstrates the potential of closed-loop macromolecule drug delivery [22].

The IntelliCap®, shown in Figure 2-1, represents an ingestible closed-loop drug delivery device. Utilizing a drug delivery capsule, the IntelliCap releases medication based on changes in pH and temperature readings. However in the scope of urgent care therapy, the IntelliCap is limited by its inability to achieve long-term gastric residency (+24h) and deliver macromolecule drugs [23].

No closed-loop drug delivery devices capable of both long-term retention and macromolecule drug delivery were found during the literature research. **Thus, while closed-loop drug delivery systems have been developed for long-term use and macromolecule drug delivery applications, an ingestible format incorporating the necessary mechanisms is currently lacking.** To better understand these limitations, we will investigate novel retention mechanisms and macromolecule drug delivery mechanisms in the following sections.

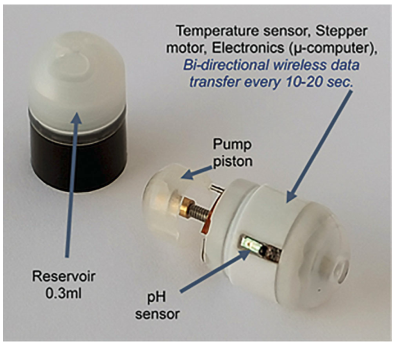

Figure 2-1: The IntelliCap® represents an ingestible closed-loop drug delivery device [23].

2-1-2 Controllability Challenges in Gastric Retention Systems

Gastric retention systems enable ingestible devices to operate from the stomach for extended periods. Extended operation is important for our application, as the timing of urgent care conditions is unpredictable. Furthermore, research indicates that minimizing patient interactions leads to higher patient adherence and improved drug efficacy [24]. In this section, we will review the current literature on gastric retention systems, focusing on their controllability limitations and their implications for urgent care applications.

Bellinger's gastric residency vehicle, shown in Figure 2-2, employs a unique folded structure that expands within the stomach, increasing its size and ensuring gastric retention. However, the device faces controllability limitations, as its retention time depends on the material properties of the leg system. The current design was found to work with retention times up to 14 days [25].

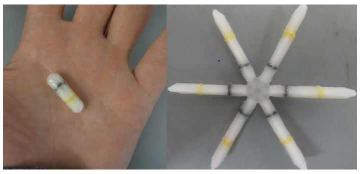

Figure 2-2: Bellinger's gastric residency vehicle [25].

The Accordion Pill operates through a chemical reaction between stomach acid and a magnesium component, generating gas and inflating a balloon-like structure to ensure gastric retention. However, for this system as well, the retention time depends solely on the chemical reaction rate, rendering the device unable to adjust residency time based on sensor data. The current design was tested up to a retention time of 8 hours [26].

The Expandable Gastro-Retentive device, shown in Figure 2-3, integrates a hydrogel and a shape-memory alloy (SMA) to achieve gastric retention. SMA is a metal that can be deformed when cold but returns to its pre-deformed ("remembered") shape when heated. Upon contact with gastric fluids, the hydrogel swells, causing the device to expand, while the SMA maintains its shape. However, similarly to the previous examples, this device requires external activation to control the SMA, making it less suitable for sensor-driven applications. Here retention was only tested for durations up to 4 hours [27].

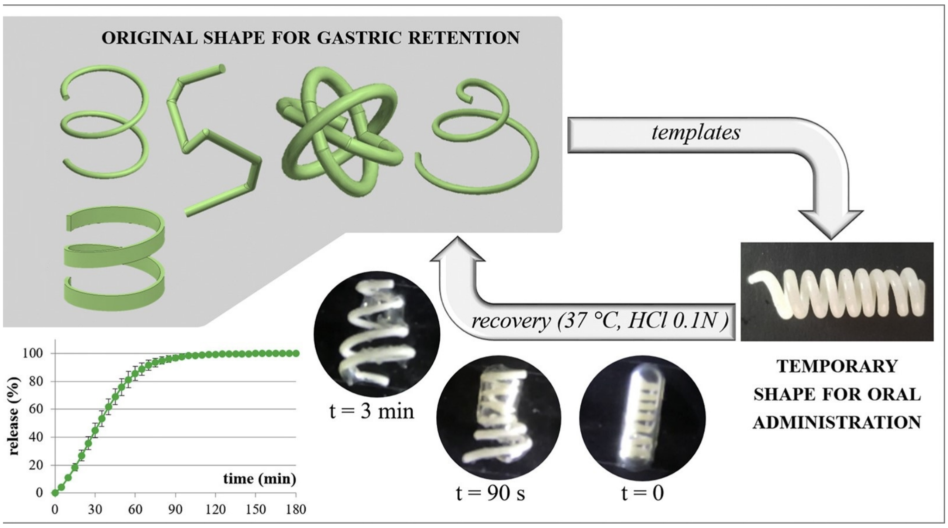

Figure 2-3: The Expandable Gastro-Retentive device [27].

Despite an extensive literature search, no other examples of gastric retention systems with controllable retention mechanisms were found. Similarly, the literature review conducted by Mau on ingestible devices for long-term gastrointestinal residency showed no research efforts on controllable drug delivery mechanisms [15]. **From these findings we conclude, that while various gastric retention systems have been proposed in the literature, they share a common limitation in controllability.** This limitation hinders the development of a closed-loop control system capable of adjusting the residency time of an ingestible device based on sensor data. **A potential solution to address the controllability limitation could involve developing a gastric retention system that incorporates an electrical actuator.** An electrically actuated retention system could offer precise control over retention time and adaptability to sensor data.

2-1-3 Controllability Challenges in Ingestible Macromolecule Drug Delivery Technology

As mentioned in Section 1-1-3, macromolecule medicines play a crucial role in the treatment of various urgent care conditions. Ingestible drug delivery systems have the potential to provide targeted macromolecule therapies without human intervention, enhancing therapeutic efficacy and enabling more widespread usability. The literature presents several systems, each with unique characteristics and limitations.

One example is the self-orienting millimeter-scale applicator (SOMA) device, which employs a chemically-triggered macromolecule drug delivery mechanism. This device is shown below in Figure 2-4. Designed for single delivery events, this device utilizes a chemical reaction between stomach acid and a component within the device to release the macromolecule drug. Although the SOMA device represents a significant advancement in ingestible drug delivery, its primary limitation is its lack of controllability. The inability to controllable drug delivery makes the SOMA unsuitable for urgent care therapy where the drug release time should be dictated according to sensor data [28].

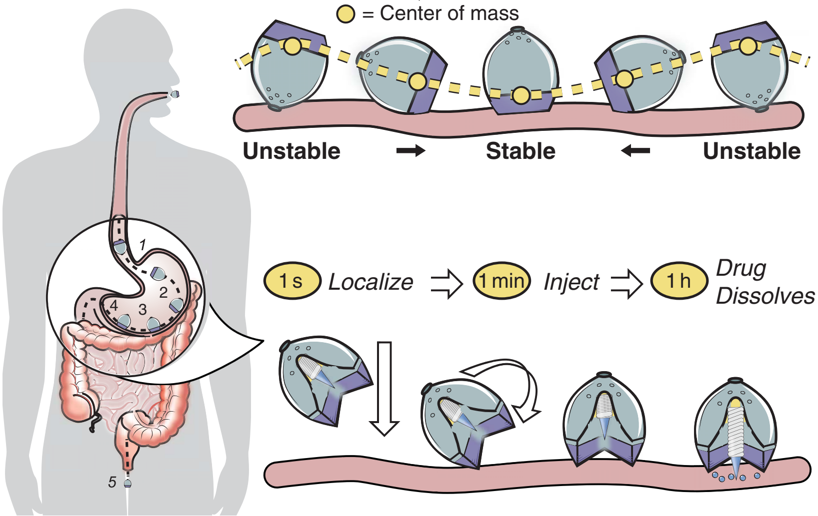

Figure 2-4: The self-orienting millimeter-scale applicator [28].

Hydrogel-based systems have also been proposed for macromolecule drug delivery. These systems rely on the swelling and deswelling properties of hydrogels to achieve controlled drug release. However, the drug release rate in these systems primarily depends on factors such as hydrogel material properties and environmental conditions, limiting their adaptability for autonomous urgent care therapy [29].

Another approach to macromolecule drug delivery involves the use of micro- and nano-carriers. These carriers can encapsulate and protect macromolecule drugs, allowing for targeted and controlled release [30]. However, here too, the release mechanisms are based on external stimuli or specific environmental conditions.

In conclusion, gastric macromolecule drug delivery has shown potential for targeted and timely drug administration. **However, a common limitation of existing macromolecule drug delivery systems is their lack of controllability, which poses challenges for realizing an effective closed-loop drug delivery system.** Among the drug delivery methods discussed, we will further investigate needle injection-based drug delivery, exemplified by the SOMA device. Our decision is guided by the practicality of leveraging existing knowledge and resources within the Traverso lab, where the SOMA device was originally developed. Similar to the gastric retention systems discussed in Section 2-1-2, one possible approach to address the controllability issue in gastric macromolecule drug delivery is replacing the chemical trigger mechanism with an electrical actuator.

2-1-4 Safety Concerns in Electrically Controlled Ingestible Devices

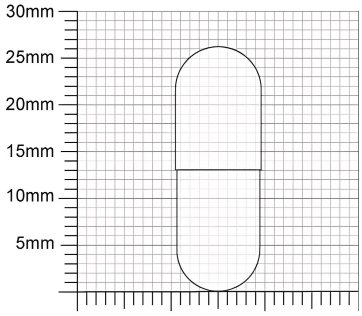

Figure 2-5: Dimensions of the 000 capsule [31].

The gastrointestinal (GI) tract presents a challenging yet delicate environment that demands close attention to both device and patient safety. Gastric fluids with pH levels as low as 1.5 can cause electrical short circuits and corrosion, while stomach motility can impose significant mechanical stress on the device, potentially leading to component failure [32]. Additionally, sharp edges and unintended chemical reactions can pose risks to patients. The United States Food and Drug Administration (FDA) has established guidelines regarding form factor and material selection for ingestible devices to ensure patient safety [11]. These guidelines stipulate that devices should not exceed the dimensions of a 000 capsule (26.1mm in length and 9.91mm in diameter) and must use biocompatible materials or coatings to prevent adverse reactions with gastric fluids.

These constraints on form factor and material selection impact the size and type of batteries that can be used in ingestible devices, limiting available electrical energy. Silver oxide batteries (SOB) are the only type found in FDA-approved ingestible systems. However, they are non-rechargeable, have a low energy density, and prefer a very low current draw compared to lithium-ion batteries (LIB) used in implantable and wearable electronic drug delivery systems. This limitation poses challenges for closed-loop devices, which require both sensing and actuation systems that consume space and energy.

Moreover, the need for small-scale, energy-efficient components restricts the computational, sensor, and actuator capabilities of electrically controlled ingestible devices. These devices often rely on low-power microcontrollers or application-specific integrated circuits, which can further constrain their computational performance. As a result, implementing complex algorithms and processing tasks, such as real-time data analysis and decision-making, becomes challenging in devices with limited processing power and memory. On this, Chen and collaborators looked into the development of novel biomedical devices and frequently highlighted computational efficiency as a key requirement [33].

Ultimately, electrically controlled ingestible devices hold the potential for enhancing diagnostics and treatments, but they face significant challenges in terms of computational complexity and operational lifespan. Addressing these obstacles necessitates inventive strategies to refine the performance of electronic components within such devices. **As we develop our autonomous ingestible system, we must carefully balance the need for high device performance with the energy and computational constraints of the system.**

2-1-5 Safety Concerns of Gastric Injection

If we want to employ a novel medical approach such as the gastric injection system, we first need to consider the safety of the feature. For this reason, we look into the literature on gastric injection. In this section, we review the literature on gastric injection safety, specifically focusing on endoscopic injections.

Gastroenterologists frequently employ needle-based injections during endoscopy procedures to inject substances into the walls of the stomach and intestines, typically using a 5-mm-long 25-gauge needle [34]. A study of 1210 upper endoscopy procedures reported no complications due to perforation, while perforations resulting from lower endoscopy occurred at a rate of less than 1% [35].

In addition to endoscopic injections, ingestible devices have demonstrated promising safety profiles. For example, Abramson and collaborators conducted a safety study on their SOMA device [28]. In this study, the researchers administered 0.3 mg of human insulin to swine via gastric injection ($n = 5$). Histological analysis confirmed that the SOMA device successfully delivered insulin through the mucosa without damaging the outer muscular layer of the stomach. Endoscopies performed one week after dosing revealed no signs of tissue damage or abnormalities resulting from the stomach injections. Furthermore, veterinary staff monitored the swine twice daily and observed no signs of distress or changes in feeding and stooling patterns after administration. To assess the safety implications of potential device malfunctions, the researchers dosed six SOMA prototypes with 3-mm-long protruding 32-gauge stainless steel needles in swine [28]. X-rays conducted over the course of nine days revealed no evidence of gastrointestinal obstruction or other adverse clinical effects.

Despite these encouraging results, several challenges must be addressed before these technologies can advance to clinical use, including ensuring the safety and delivery consistency of the devices. The risk of perforation of the intestinal wall exists if a device designed for delivery in the stomach deploys in the small intestine [18]. As the deliverable dose of the device is constrained by the volume, formulation, and stability of the needle, increasing the depth and width of needle penetration could enhance drug loading but may compromise the gastric mucosa and elevate perforation risk [28].

In conclusion, early studies on gastric injection safety demonstrate a promising safety profile. As we continue to advance these technologies, further research will be necessary to thoroughly assess their long-term safety and efficacy. Nevertheless, **gastric injection technology holds significant potential as a valuable tool for autonomous urgent care therapy and is promising for our urgent care therapy application.**

2-1-6 Factors Influencing Patient Acceptance and Adoption of Ingestible Technologies

The adoption and impact of an ingestible urgent care therapy device are not only dependent on its technical feasibility but also on patient willingness to embrace the technology. If patients are reluctant to use the device, its potential benefits and overall impact may be diminished. Therefore, it is crucial to understand the factors that contribute to patient willingness when developing and implementing ingestible devices. Several studies have explored patient attitudes toward different aspects of ingestible technologies, offering valuable insights into the factors that may influence their acceptance and adoption. These factors encompass perceived benefits, ease of use, data privacy, trust, and ethical considerations.

In a study by Chevance and collaborators, the acceptability and willingness to use digital pills was investigated among patients, the public, and healthcare professionals through a large online survey [36]. While the study demonstrated a generally positive attitude towards digital pills, concerns about data privacy and the invasiveness of the technology were also raised.

Perry and collaborators explored patient preferences for using portable technologies in clinical trials [37]. Participants expressed interest in adopting portable technologies, including ingestible devices, for trial purposes, citing potential benefits such as improved convenience, reduced burden, and better communication with healthcare providers.

Vaz and collaborators conducted a study on the formative acceptance of ingestible biosensors for monitoring adherence to tuberculosis medications [38]. Participants displayed a willingness to use the technology, but highlighted their concerns about cost, privacy, and long-term safety.

Zijp and collaborators evaluated the user acceptability and technical robustness of a smart pill bottle prototype designed to support medication adherence [24]. The study found that users generally accepted the technology and appreciated its potential to enhance medication adherence.

Forma and collaborators evaluated caregiver preferences for health technology tools to monitor medication adherence among patients with serious mental illness [39]. Caregivers preferred digital tools, including ingestible technologies, that could track both medication ingestion and general health. However, they also expressed concerns about data privacy.

Klugman explored the ethical considerations of smart pills and self-acting devices, focusing on issues related to autonomy, truth-telling, and trust [40]. Klugman highlighted the importance of addressing these ethical concerns to ensure the successful integration of ingestible devices in healthcare.

Aldeer reviewed medication adherence monitoring technologies, including ingestible devices, and their potential to improve patient adherence [41]. Aldeer stressed the need for further research on the long-term safety, efficacy, and cost-effectiveness of these monitoring technologies.

In conclusion, the existing literature on patient willingness to adopt ingestible technologies reveals a generally positive attitude toward these devices. Factors such as perceived benefits, ease of use, data privacy, trust, and ethical considerations play a crucial role in shaping patient attitudes. **From a control perspective during the development process, we can help improve the ease of use by limiting the need for external inputs for the device use. Additionally, to enhance trust and acceptance, developing the device as a fully autonomous system may help alleviate concerns related to data transfer safety issues.**

2-2 Thesis Statement

In Section 1-2, we emphasized the potential for creating ingestible devices capable of detecting and treating medical emergencies caused by harmful agents, leveraging advancements in harmful agent detection and ingestible device technology. Our literature review in this chapter validates the potential for ingestible technologies to function as closed-loop drug delivery devices for urgent care therapy. However, existing ingestible retention and injection technologies exhibit controllability limitations. Moreover, enhancing device autonomy and operational lifetime to ensure user-friendliness in current closed-loop technologies remains a challenge.

To tackle the limitations concerning retention and macromolecule drug delivery, the lab has developed a microactuator-driven gastric retention and injection mechanism prototype. This prototype aims to counteract gamma radiation poisoning using a sargramostim injection. The device is built as an adaptable platform that facilitates the possible replacement of the harmful agent sensors and associated medication, rendering it suitable for treating various medical emergencies requiring on-demand macromolecule drug delivery.

In this thesis, we concentrate on developing the device's control system to realize its retention and therapy capabilities while optimizing ease of use in terms of autonomy and operation time. Consequently, we formulate the thesis statement of this research as follows:

"Develop a control system for an ingestible device that can safely reside in the stomach and provide on-demand macromolecule drug delivery to autonomously address medical emergencies caused by harmful agents."

2-2-1 Research Challenges

To achieve the thesis statement outlined above, the following research challenges must be addressed:

- Develop a **sensor system** that ensures accurate and robust input data for actuator control and decision making, while maximizing computational simplicity;
- Develop an **actuator control system** that ensures reliable and timely retention and injection, while maximizing battery operation time;
- Develop a **decision making system** that ensures patient safety and increases injection reliability, while maximizing battery operation time.

In this context, the decision making system represents an algorithm that, at a high level, decides on the usage of the sensor system and actuator system. Based on sensor data and actuator positioning, it determines the device's state and associates that state with a course of action. This course of action includes activating specific sensors and data processing pipelines to assess the environment and device conditions and setting objectives for the actuator system. Examples include monitoring the presence of gamma radiation, battery power, or initiating injection.

The thesis is organized around these research challenges, addressing the development of the sensor system in Chapter 4, the actuator system in Chapter 5, and decision making system in Chapter 6.

2-2-2 Design Criteria

To evaluate the feasibility of the proposed autonomous urgent care therapy device, we need to assess the various functional components of the device. To address this, we established the set of criteria outlined below:

1. Assess the feasibility of the sensor-based decision making system:
    - (a) Evaluate the accuracy of the onboard sensor system in monitoring needle angle, targeting an accuracy of 10 degrees or better[1];
    - (b) Validate the decision making system's ability to guide injections, ensuring injections only occur within stomach tissue;
    - (c) Validate the decision making system's ability to initiate drug delivery based on harmful agent detection without generating false positives or negatives;
    - (d) Validate the decision making system's ability to prevent unwanted retention in the event of component failure.
2. Assess the feasibility of controllable gastric retention and injection:
    - (a) Investigate the injection mechanism's capability to deliver medicine on-demand: within 24 hours for radiation poisoning treatment [3], and within 5 minutes for Anaphylaxis [42];
    - (b) Address all safety concerns related to actuator failure.
3. Evaluate potential barriers to adoption concerning autonomy, long-term operation, and manufacturing:
    - (a) Develop a control system powered by a battery deemed suitable by the FDA for ingestible applications;
    - (b) Optimize energy consumption to achieve a device run time of at least 14 days[2];
    - (c) Ensure user-friendliness through a fully autonomous design that requires no human interaction post-ingestion;
    - (d) Utilize common components for the control system to enable mass production.

The objective of this study is to maximize the feasibility of the autonomous, ingestible device for urgent care therapy while ensuring a long device run time. Upon a thorough investigation of the research objectives listed above, we present our findings in Chapter 7. Furthermore, we provide recommendations in Chapter 8 based on our research, which can guide further development of the system.

Note 1: No literature on the relationship between the angle of injection and the drug efficacy could be found. The 10 degree accuracy threshold should later on be evaluated according to tests with the injector prototype.

Note 2: The device run time is based on the retention time for the longest lasting gastric drug delivery device, that is the 14 day long residence test of Bellinger's retention mechanism discussed in Section 2-1-2.

Chapter 3

System Description

With the thesis statement established, we now focus on the device under consideration. We start by introducing the existing prototype of the innovative retention and injection mechanism in Section 3-1. To allow for active control over this mechanism we present a conceptual control system in Section 3-2. Finally, in Section 3-3, we concretize the conceptual control system. We provide a comprehensive overview of the device and detailed descriptions of each component. This analysis aims to give the reader a clear understanding of the system's design and functionality. This foundation will support the subsequent chapters on the sensor system, actuator system, and decision making system.

Research Contributions to the Component Development and Selection

This chapter primarily focuses on the hardware of the existing prototype. Herein the reorientation and injection mechanism, printed circuit board (PCB), and urgent care detection sensor were developed or selected by other team members. The author collaborated in the selection and testing of components relevant to the reorientation control system, involving the inertial measurement unit (IMU), power monitor, voltage converter, H-bridge, microactuator, microcontroller unit (MCU), and programming language.

3-1 Mechanism Workflow of the Proposed Device

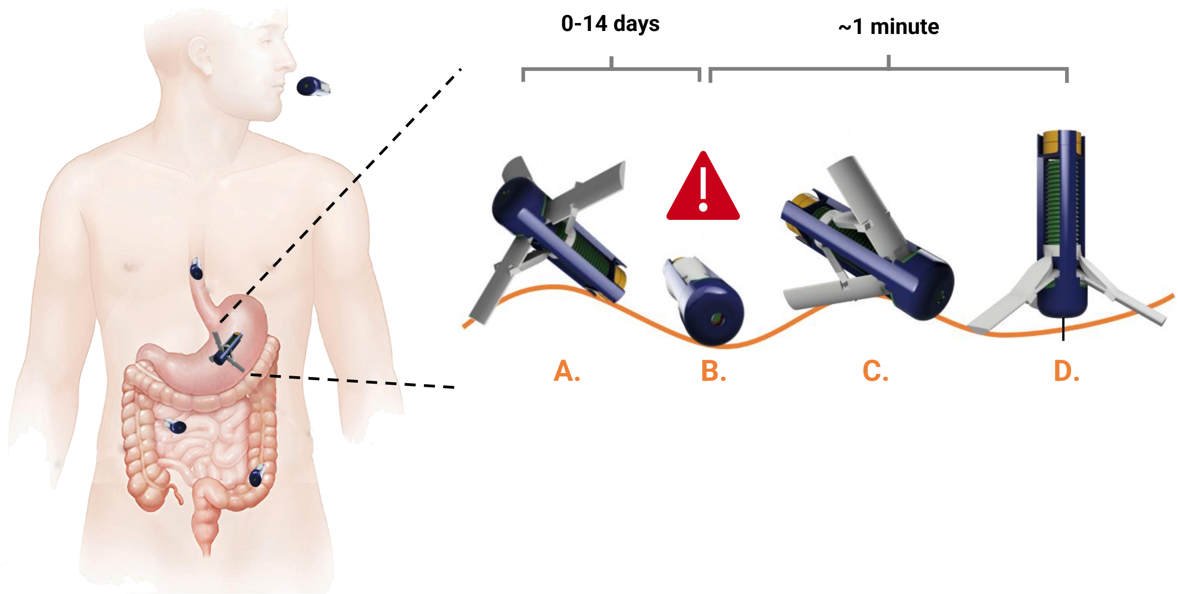

Figure 3-1: Workflow of the proposed ingestible device upon detection of a harmful agent. **A.** Upon entering the stomach, the legs partially unfold to ensure gastric retention. **B.** After detecting a harmful agent, the legs fold in. Subsequently, **C.** the device slowly unfolds until the needle points towards gravity. Finally, **D.** the injection mechanism is triggered.

The lab's objective is to develop a device capable of remaining in the stomach, detecting the presence of harmful agents, and administering a medicine injection into the stomach wall within 10 minutes to minimize damage [3]. To achieve this goal, the Traverso Lab created a conceptual design based on the retention system presented in Bellinger's work [25], combined with Abramson's spring-based injection mechanism [28]. The resulting device remains in the stomach by unfolding its legs and provides a single drug delivery through a spring-loaded biodegradable injector. Unlike passive actuation through a chemical reaction with stomach acid, our mechanism uses an electric motor, enabling controlled retention and on-demand macromolecule drug delivery.

Figure 3-1 illustrates a high-level workflow of the retention and injection mechanism. The device starts in a folded form, small enough to be swallowed. Once in the stomach, the legs unfold to prevent further passage to the small intestines. The device remains in the stomach with its legs unfolded until it detects a harmful agent or the batteries approach depletion. Upon detecting a harmful agent, the device attempts to orient the needle towards the stomach wall, involving three steps: first, the device closes its legs to rest on its side; second, the device unfolds the legs to achieve a standing position with the needle aimed at the stomach wall; finally, the device performs the injection. The device's weight density ensures that the device rests on the stomach wall, facilitating reorientation and gastric injection. Once the battery is near depletion or after an injection, the legs fold in to allow the device to continue passage through the gastrointestinal (GI) tract and exit the body. During exit, the device will localize its environment to inform the patient of success or failure.

A key element of this workflow is the decision making and mechanism steering based on the environment and device orientation, such as responding to low battery power and the subsequent folding of the legs. Moreover, the device should be capable of adapting when the workflow does not proceed as expected. For instance, the round shape of the gastric environment and frequent stomach contractions could cause the device to topple over during reorientation. To facilitate effective decision making and steering, the device must be equipped with a control system. To ensure successful reorientation, the control system should be a closed-loop system capable of responding to sensor feedback.

3-2 Conceptual Design of the Control System for Reorientation and Injection

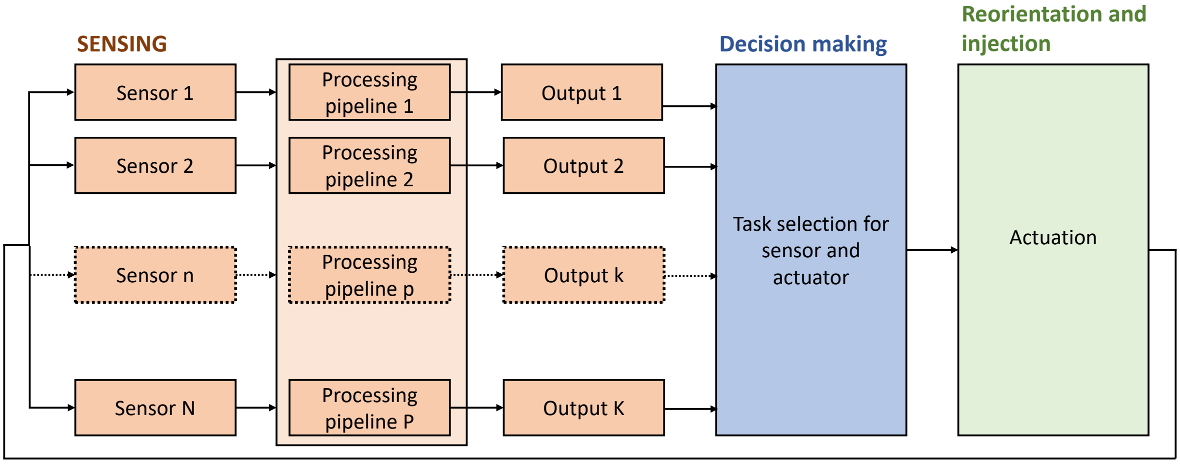

Figure 3-2: Conceptual control system diagram of a closed-loop reorientation and injection system.

Figure 3-2 presents a conceptual control system diagram of the reorientation and injection system required for the operation of the device illustrated in Figure 3-1. This conceptual design provides an overview of the thesis structure and serves as a foundation for outlining the thesis.

The control system is composed of three primary components: the sensor system, the decision making system, and the reorientation and injection system. The sensor system consists of a set of sensors N to monitor a series of outputs K. A set of processing pipelines P transforms the raw sensor data into usable outputs K by employing signal processing and sensor-fusion techniques. The decision-making system utilizes these outputs K to assess the current state of the device and provide guidance for motion control. Furthermore, the decision making system determines if adjustments are needed for the sensor system, such as the (de)activation of specific sensors and data processing pipelines to optimize energy consumption and computational load. Finally, the reorientation and injection system involves steering the actuator based on the input from the decision making system.

3-3 System Design and Components

In this section, we present a comprehensive overview of the system by concretizing our conceptual system diagram from Section 3-2. We provide an overview of the complete design, followed by a detailed examination of each major component group: the sensor system, decision-making system, and actuator system. After having discussed all components, we discuss the powering of these components and the expected device operation time. For each specific component, we justify our selection process according to the criteria from Section 2-1-4: performance, physical footprint, and energy consumption.

3-3-1 Overview of the Physical Design

The research objective of creating an autonomous urgent care therapy device led to the development of an early prototype capable of remaining in the gastric tract, administering medication, and safely passing through the GI tract. The physical design can be split into two components: the main body and the injector, as illustrated in the high-level exploded view presented in Figure 3-3. The main body houses the retention mechanism and all electrical components, which are shielded by a biocompatible coating for protection. On the other hand, the injector features a watertight shell to store the drug content and facilitate drug delivery. These two components can be used independently, providing a modular design for future development.

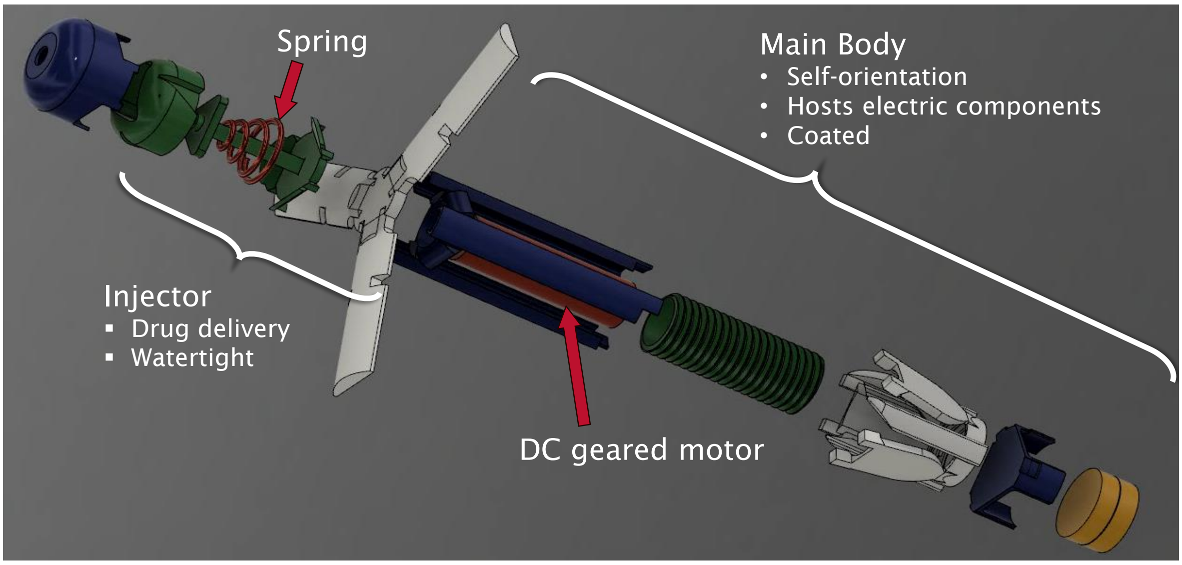

Figure 3-3: Exploded overview of the ingestible autonomous urgent care therapy devices. Designed by P. Fritz.

Not shown in the image is the PCB that hosts the sensor and computational components. To conserve space, we install a flexible PCB within the 3-legged arm system shown in white in Figure 3-3. The bending radius of the PCB is directly related to the thickness. However, reducing the thickness also means less space for layers in the PCB. We present a finalized PCB design in the general results of the study in Chapter 7.

3-3-2 Sensor System Components: Specification and Functionality

In our sensor system, we employ milliscale motion sensors based on microelectromechanical systems (MEMS) technology. MEMS technology facilitates the development of sensors that are compact, lightweight, cost-effective, energy-efficient, and characterized by rapid start-up times. The sensor system is designed with the research objectives for the sensor-based decision making system of Section 2-2-2 in mind: preventing unwanted retention, actuator steering, and urgent care detection.

Figure 3-4 provides an overview of the components of the sensor systems, and with that the topic of this section. Focusing on gamma radiation poisoning in this sensor system, we incorporate a gamma radiation sensor for urgent care detection. Motion control monitoring presents a more complex challenge from a sensor processing perspective, as it requires monitoring both the environment and the device itself. To determine the appropriateness of reorientation, we aim to detect stomach motility using acceleration. Additionally, to assess the success of reorientation, we monitor the device's position using an accelerometer, gyroscope , and potentially a magnetometer. Else we utilize the magnetometer to ensure proper control of our reorientation and injection mechanism, by tracking the motor itself. While implementing these measures, patient safety remains a top priority. We strive to prevent unwanted retention due to low battery power or motor malfunction by employing a power monitor capable of sensing the battery voltage and motor current.

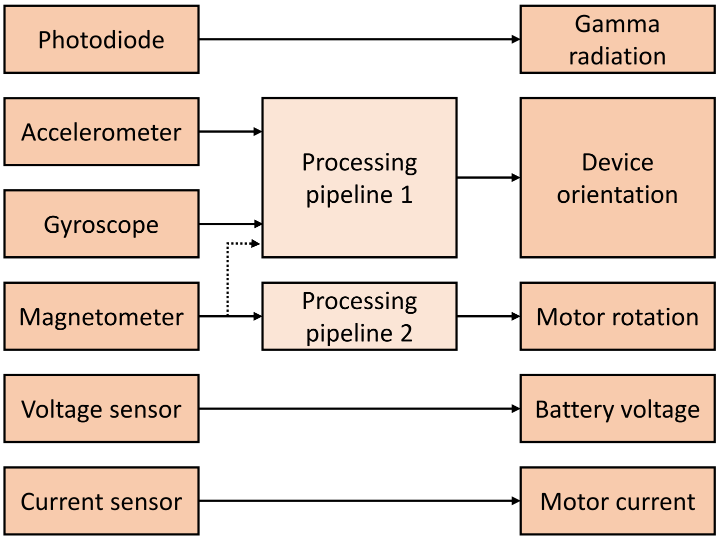

Figure 3-4: Component overview of the sensor system.

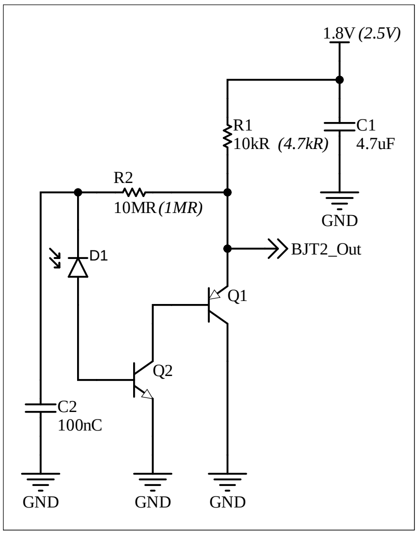

Figure 3-5: Circuit diagram of the gamma sensor [43].

3-3-2-1 PIN Photodiode for Gamma Radiation Detection

Gamma radiation is an electromagnetic wave with a wavelength shorter than 100±nm that can penetrate the human body, making gamma detectors suitable for use in ingestible electronics. Traditionally, Geiger counters are employed for data collection; however, their miniaturization is challenging due to the need for a gas chamber. As an alternative, we propose a gamma sensor design based on a PIN photodiode, with its electrical circuit illustrated in Figure 3-5. PIN photodiodes present a promising alternative for miniaturization, given their small size and high sensitivity [44]. While many PIN diodes exhibit low sensitivity to gamma radiation, a gamma sensor can still be developed by coupling the diode with an amplifier and isolating it from visual light and other electromagnetic signals.

3-3-2-2 Inertial Measurement Unit for Device Orientation and Motor Rotation Tracking

For the injection mechanism to successfully deliver medicine, it is essential to ensure the needle faces the stomach wall before initiating the injection. As mentioned in Section 3-1, the weight density of the device guarantees its proximity to the stomach wall. The reorientation mechanism allows the device to adjust, enabling the needle to face the direction of gravity and consequently, the stomach wall. To confirm the reorientation has occurred correctly and determine if the needle is facing the direction of gravity, we need to monitor the device's orientation.

An IMU is a widely utilized device in robotics for tracking orientation. The IMU is a state-of-the-art integrated circuit comprising multiple sensors for motion tracking. Unlike camera-based or radar-based orientation mechanisms, an IMU does not require communication with external devices, which is advantageous since reliable external communication cannot be guaranteed due to the difficulty of signal propagation through human skin. We selected an IMU with a minimum of a 3-axis accelerometer, 3-axis gyroscope, and a 3-axis magnetometer to ensure accuracy and reliability. This 9-degrees of freedom (DOF) IMU, commonly referred to as a 9-axis IMU, enables determining the device's orientation in all angles, including pitch, yaw, and roll, as illustrated in Figure 3-6. Furthermore, if the magnetometer is not required for orientation tracking we can alternatively use the magnetometer to track the motor. By attaching a magnet to the motor rod we allow the magnetometer to function as a motor encoder.

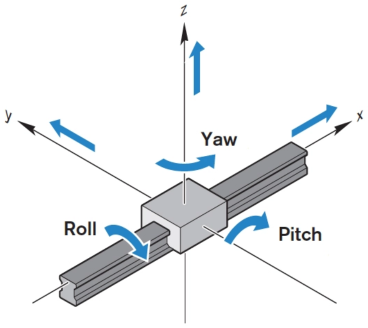

Figure 3-6: Tait Bryan angles: pitch, yaw, and roll [45].

The MEMS accelerometer measures external accelerations a_{ex} and gravity g. These measurements allow us to estimate the device's orientation in terms of pitch and roll using a set of equations. The accelerometer's operation is based on Newton's Second Law of Motion, which states that the total measured force is equal to the product of proof mass and acceleration. Error free accelerometer would measure zero acceleration in all axes during freefall. While when positioned upright on Earth, the accelerometer senses the normal force counteracting gravity, resulting in a measured acceleration in the positive z-direction [46].

The gyroscope measures angular velocity ω in terms of pitch, yaw, and roll. The MEMS gyroscope operates based on the Coriolis effect, a phenomenon that occurs when a moving object experiences a force perpendicular to its motion while in rotation. The gyroscope consists of a miniature vibrating structure oscillated at a resonant frequency. When rotation is experienced, the Coriolis force induces a change in the vibrating structure's motion, which can then be measured [47, 48].

MEMS magnetometers are compact sensors capable of detecting changes in magnetic fields. The sensing element typically comprises a thin film of a magnetoresistive material such as permalloy or a magneto-optical material like garnet. This sensing element alters its electrical or optical properties in response to magnetic fields. A magnetometer can be used to measure the Earth's magnetic field and estimate the device's orientation in the yaw position. Alternatively, the device can detect the location of a magnetic object in its vicinity. In our system, we can utilize this feature by attaching a magnet to the motor and monitoring its movements. However, it is important to note that the presence of a magnetic object can interfere with the Earth's magnetic field, making it impossible to use both magnetic fields simultaneously. Therefore, we must evaluate the necessity of the magnetometer for monitoring the device's orientation. We will focus on this aspect in detail in Chapter 4.

In order to determine the most suitable IMU for our small-scale orientation system, we analyzed three options: the BNO-055 from Bosch Sensortec GmbH, the BMX160 from Bosch Sensortec GmbH, and the ICM20948 from TDK Corporation™. As the IMU is a crucial component for accurate orientation monitoring, it is important to consider factors such as update frequency, accuracy, and power consumption, among others. A summary of these parameters is provided in Table 3-1.

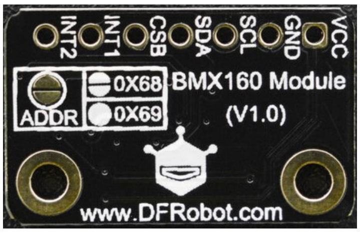

Figure 3-7: BMX160 9-axis IMU from Bosch [49].

The BMX160 emerged as the IMU of choice for our application. With an update rate of 1600 Hz, it outperforms both the BNO-055 (100 Hz) and the ICM20948 (1125 Hz). This high update frequency enables real-time tracking of the device's movements with minimal latency, resulting in a more responsive and accurate system. The BMX160 exhibits a typical energy consumption of 1.56 mA when all sensors are in use, lower than that of the BNO-055 (12.3 mA) and the ICM20948 (3.11 mA). Moreover, the BMX160 consumes a mere 3 µA in sleep mode, making it an energy-efficient option that contributes to the overall power management of the system. When looking at voltage all three systems operate within the same range of 1.71 to 3.6V. This all without compromising measurement accuracy. With an accelerometer accuracy of 0.1% FS, gyroscope accuracy of 0.05% FS, and magnetometer accuracy of 0.2% FS, the BMX160 is on equal foot both with the BNO-055 and the ICM20948.

In conclusion, the BMX160 is the IMU of choice for our small-scale orientation system, because of its relatively high update frequency, high accuracy, and low energy consumption, without compromising in measurement accuracy. These features make it well-suited to deliver reliable estimation, which in turn may reduce the data processing needs and allow for better informed decision making.

Table 3-1: Comparison of IMU options: BNO-055, BMX160, and ICM20948.

Parameter	**BNO-055** [50]	**BMX160** [49]	**ICM20948** [51]
Accelerometer Range	± 16 g	± 16 g	± 16 g
Gyroscope Range	± 2000 dps	± 2000 dps	± 2000 dps
Magnetometer Range	1300 μT	1300 μT	4900 μT
Data Resolution	16 bit	16 bit	16 bit
Current Consumption	12.3 mA	1.56 mA	3.11 mA
Sleep Mode Current	40 µA	3 µA	8 µA
Operating Voltage	2.4 - 3.6 V	1.71 - 3.6 V	1.71 - 3.6 V
Interface	I^{2}C, SPI	I^{2}C, SPI	I^{2}C, SPI
Update Frequency	1000 Hz	3200 Hz	1125 Hz
Accelerometer Accuracy	0.2% FS	0.1% FS	0.1% FS
Gyroscope Accuracy	0.1% FS	0.05% FS	0.05% FS
Magnetometer Accuracy	0.3% FS	0.2% FS	0.15% FS

3-3-2-3 Power Monitor for Battery Capacity Tracking and Motor Current Sensing

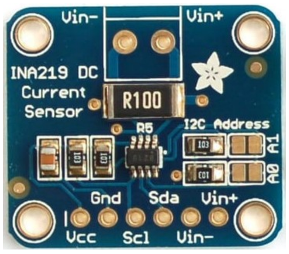

Figure 3-8: INA219 power monitor by TI [52].

One of the main objectives of our sensor-based decision making system is ensuring patient safety and preventing unwanted retention. A power monitor can help address these concerns by measuring the battery voltage to detect low battery power and motor current to detect actuator stalling.

Patient safety and preventing unwanted retention of the device are essential aspects of our ingestible system. One approach to address these concerns is to monitor the battery voltage and motor current, which can be achieved using a power monitor. This integrated circuit measures the voltage, current, and power consumption of a device, allowing for the detection of abnormal behavior in the battery and motor. This information can then be used to take appropriate action, such as reversing actuator movement to prevent harm to the patient or device damage.

The INA219 is the ideal choice for our system due to its integration, high-side current and voltage monitoring, and I2C-compatible interface. This allows for straightforward integration with the microcontroller and accurate readings compared to analog alternatives. The device measures voltage with a 1.25 mV resolution and current with a 0.1 mA resolution, providing precise sensor readings without extensive filtering. Additionally, the INA219 detects short circuits, enhancing safety in case of component failure.

3-3-2-4 Auxiliary Sensors Outside the Scope of the Thesis

While this thesis focuses on closed-loop reorientation, the overall electrical system includes auxiliary sensors for gastric area detection and patient monitoring. Although not directly related to the main objective, these sensors contribute to the system's energy consumption and must be considered in the final device description.

The auxiliary sensors include the BME280, a humidity and pressure sensor for gastric localization, and the SPW2430HR5H-B microphone for heart rate and respiratory rate monitoring. By accounting for the energy requirement of all electrical components, we can better assess the overall power requirement and estimate the operating time of the full device.

3-3-3 Decision Making System Components: Specification and Functionality

The sensor data processed by the components detailed in the previous section provide insights into the urgent care condition, the gastric environment, and the device itself. This sensor data enables informed decision making for preventing unwanted retention, urgent care detection, and actuator steering. Section 3-3-3 illustrates how the decision making system is placed within the control system.

The decision making system needs to be able to adapt to changing conditions within the gastric environment and the device's status. For instance, the system must be able to intelligently manage its power consumption by selectively activating or deactivating sensors and actuators based on the current situation and remaining battery life. Furthermore, the system should be capable of detecting and handling potential failures or malfunctions, such as sensor drift or motor jams to ensure patient safety and device reliability.

The decision making system heavily relies on the algorithms implemented within the ingestible device. Functioning as the central nervous system, the MCU receives and processes sensory inputs and generates appropriate responses through the actuator system. Figure 3-10 illustrates the central role of the MCU within our proposed system and therefore the overall decision making. Consequently, the efficacy of the entire system depends heavily on the proper functioning and programming of the MCU. One of the key aspects of the MCU is the ability to process and fuse data from various sensors in real-time. This requires the implementation of algorithms, such as Kalman filters, that can combine the data from different sensors while accounting for uncertainties and noise.

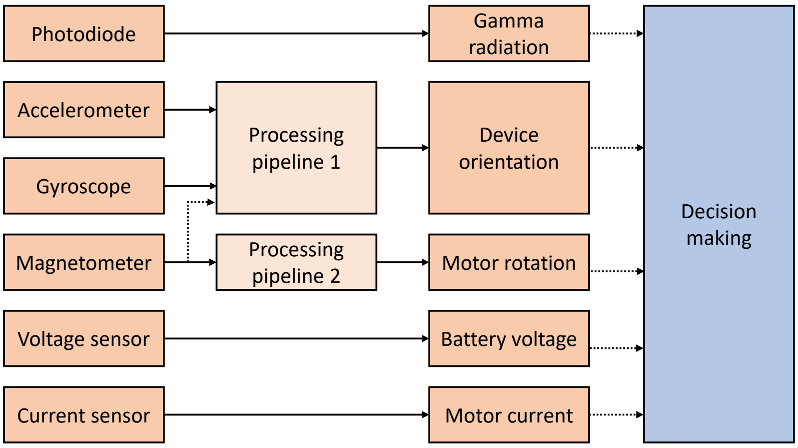

Figure 3-9: Component overview of the closed-loop reorientation and injection system: the sensor system in cascade connection with the decision making system.

While the MCU mainly determines the computational capabilities, the programming language that is used to write the algorithm plays a large role in the computational load. Therefore, in addition to the MCU, we will also be looking into the selection of an appropriate computing language for the implementation of our data processing and control algorithms.

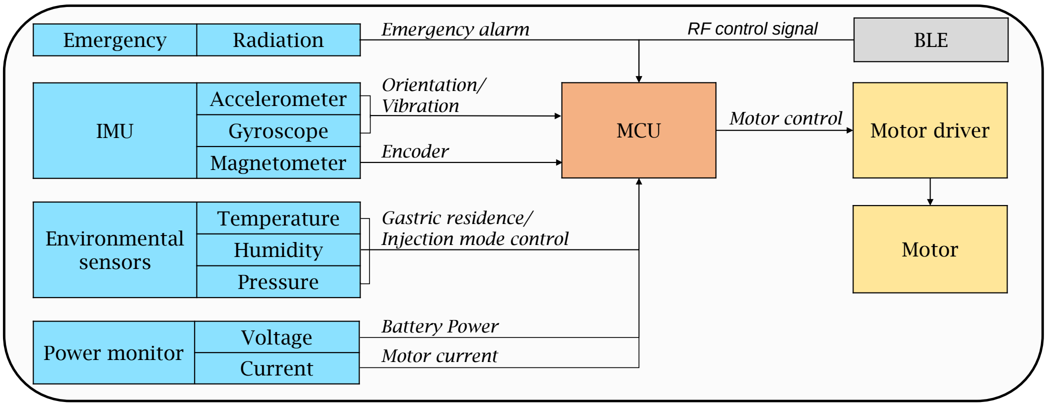

Figure 3-10: Communication circuit of the autonomous urgent care therapy device showing the central role of the MCU, with the sensor system in blue, the actuator system in yellow, the MCU in orange, and the MCU's integrated Bluetooth communication unit in grey.

3-3-3-1 Microcontroller Unit for Data Processing and Component Communication

The MCU is at the core of the processing pipeline, responsible for managing all electrical components, processing information, and performing calculations. In the selection of the MCU we mainly look at the computational capabilities and power consumption. The nRF52840 was chosen for its industry-standard performance across various domains, including consumer technology and medical devices [53]. A key criterion was its high clock speed of up to 64MHz, which ensures efficient computation and enables faster sampling rates for sensors and higher control resolution for actuators.

The nRF52840 features an ARM Cortex-M4F processor and a multiprotocol Bluetooth 5.0 compatible antenna, making it suitable for integration into a wide range of applications. The integrated antenna enables communication with the device even when ingested, making it ideal for radiation poisoning emergencies where rapid response is crucial. Additionally, the chip's 48 configurable general-purpose input/output (GPIO) pins facilitate various digital input/output (I/O) operations, serial, inter-integrated circuit (I^2C), and Serial Peripheral Interface (SPI) communication. The nRF52840's versatility is further enhanced by its broad voltage supply range of 1.7V to 5.5V. The SoC's comprehensive documentation and the availability of several microcontroller main-boards, or feathers, enable rapid prototyping and ease of integration. In summary, the nRF52840's computational capabilities and versatility make it a great choice for our application.

Table 3-2: nRF52840 Microcontroller Characteristics [53].

Parameter	**nRF52840**
Processor	32-bit ARM Cortex-M4F
Operating Frequency	64 MHz
Memory	1 MB flash, 256 kB RAM
Supply Voltage Range	1.7 - 5.5 V
Interfaces	I2C, SPI, ADC, UART, PDM, PWM, QDEC
Bluetooth Version	Bluetooth 5.2
Security Features	AES, ECC, RSA

3-3-3-2 C++ as the Programming Language

The selection of a programming language significantly influences the success of a software development project. The energy and computational capabilities of our system will be low due to the size requirement for ingestion. Therefore, in the selection of a programming language we specifically look at high computational power and efficient memory management. Additionally, we prefer a language that is widely adopted to allow for easier integration and reduce development time. After evaluation, we selected C++ as the programming language of choice.

C++ is renowned for its performance, strong typing, and wide range of applications. Its ability to optimize performance through direct hardware access is critical for resource-constrained real-time applications, such as the reorientation process for needle alignment, which demands rapid processing of IMU data and efficient actuator control. When considering energy and memory efficiency, C++ ranks third, just after C and Rust, and enables relatively easy conversion to C if needed later on [54]. Additionally, C++ provides extensive library support for accelerated development, and compatibility with the nRF52840 MCU, which features a built-in C++ compiler. This compatibility simplifies code integration and reduces development time and effort for implementing the control system [53].

3-3-4 Actuator System Components: Specification and Functionality

The actuator system consists of various components designed to work in unison, providing active control in a compact form. These components include a direct current to direct current (DC-DC) voltage converter, H-bridge, direct current (DC) geared motor, nut, and bolt coupling, reorientation mechanism, and injection mechanism. The primary objectives of the actuator system are to ensure stomach retention, reorient the device, and inject medication.

Figure 3-11 shows in green the component of the actuator system and with that the topic of this section. The DC-DC voltage converter and H-bridge determine the power delivered to the motor, playing an important role in motor control and power consumption management. The DC geared motor converts electrical energy into physical force, serving as the driving force behind the mechanism's movement. The nut and bolt coupling is a compact system that transforms the motor's rotational movement into linear translation, which is utilized for steering the reorientation mechanism and triggering the injection mechanism. The reorientation mechanism, resembling a tripod-like structure, enables stomach retention and reorientation, while the injection mechanism houses a spring-loaded needle responsible for on-demand delivery of macromolecule medication.

In the following sections, we will discuss the specifications and functionalities of each component in detail, emphasizing the rationale behind our choices and their contributions to the overall reliability and performance of the ingestible device. Note that herein the author did not contribute to the development of the purely mechanical components, that are the nut and bolt coupling, reorientation mechanism, and injection mechanism. By understanding the interplay between these components, we can optimize the actuator control system in subsequent chapters.

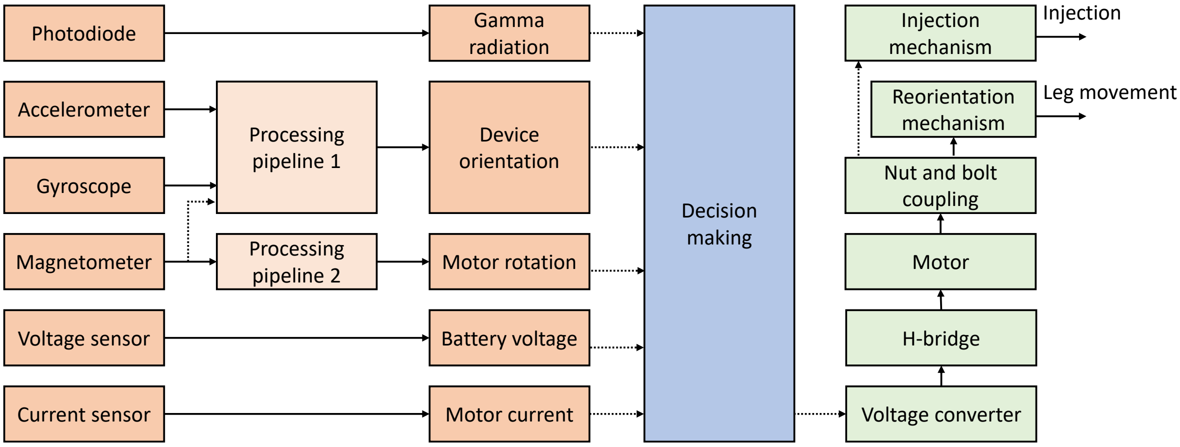

Figure 3-11: Component overview of the closed-loop reorientation and injection system: the sensor system in cascade connection with the decision making system and treatment system.

3-3-4-1 Novel Injection Mechanism for On-demand Gastric Macromolecule Drug Delivery

Inspired by the self-orienting millimeter-scale applicator (SOMA) [28], the Traverso Lab developed a novel spring-loaded injector that enables watertight storage of a biodegradable needle and controlled needle injection. The injector consists of six distinct parts, as shown in Figure 3-12: the biodegradable needle, a revolver that maintains spring tension and can be released to initiate the injection, the needle platform above the spring, the spring causing needle displacement, and the base platform beneath the spring. This injection mechanism is safely housed within an outer shell, as illustrated inFigure 3-3. The outer shell features a thin silicone membrane to ensure watertightness for the biodegradable needle, and the injector's holes are filled with lubricant to maintain complete watertightness.

Drug delivery is initiated by the unlocking action of the nut's prongs when the nut is fully moved towards the injector, and the legs are completely extended. The nut's prongs rotate the revolver, releasing the spring-loaded platform holding the solid-state drug needle. Consequently, the platform's release allows the needle to penetrate the stomach tissue.

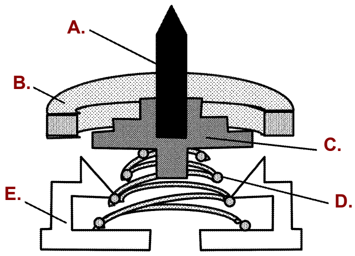

Figure 3-12: Component description of the needle injection mechanism, with **A.** the biodegradable needle, **B.** a revolver that maintains spring tension and can be released to initiate the injection, **C.** the needle platform above the spring, **D.** the spring causing needle displacement, and **E.** the base platform beneath the spring. Adapted from [55].

3-3-4-2 Bolt and Nut Coupling for Rotational to Linear Movement Conversion

Inspired by the classic bolt and nut coupling, the Traverso Lab developed a compact mechanism to convert the motor's rotational movement into linear movement. Herein the bolt's interior is hollow, allowing the motor to be placed inside, conserving space. The smallest bolt dimension that can accommodate the DC geared motor is an M8x1 nut, with a major diameter of 8mm and a pitch of 1mm, as illustrated in Figure 3-13. The nut has a thickness of 4mm, typical for an M8 jam nut [57]. By controlling the bolt and nut coupling, we can manage the leg system for reorientation and needle injector triggering for macromolecule drug delivery.

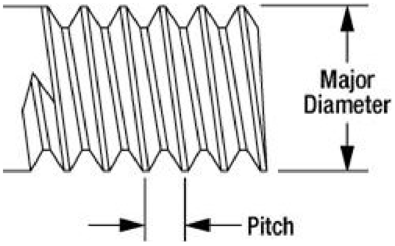

Figure 3-13: Visualization of screw thread dimensions [56].

3-3-4-3 Novel Reorientation Mechanism for Retention and Needle Alignment

The reorientation mechanism features a tripod-like leg system actuated through the bolt and nut coupling system. Herein the nut's linear translation allows for the linear translation of each leg's midpoint, as shown in Figure 3-14. With the legs' beginnings fixed, this permits the rotational movement necessary to accomplish our desired tasks.

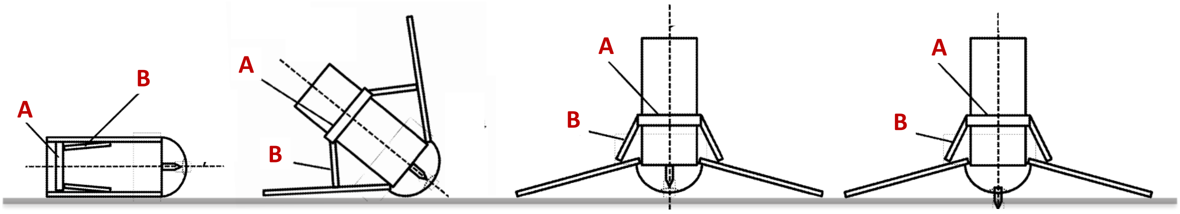

Figure 3-14: Reorientation mechanism workflow: from a resting position (left) to injection (right), with **A.** the screw-nut coupling, and **B.** the nut-leg attachment. Adapted from [55].

3-3-4-4 Direct Current Geared Motor for Mechanism Actuation

DC motors are widely employed in mechatronic systems due to their high driving torque, rapid start and stop capabilities, reversing functionality, variable speeds with different voltage inputs, and ease of control. We selected the Sub-Micro Plastic Planetary Gearmotor from Pololu as our specific DC motor based on low energy consumption, high stall torque, compact size, and proper motor speed.

In our ingestible system, the size of the motor is an important consideration, as it will be one of the device's largest components. The chosen motor offers a compact size and a variety of options with regard to gear ratios. Each gear ratio option presents a balance between size, stall torque, and motor speed, as demonstrated in Table 3-3.

A requirement in the selection of our motor (and gear size) is that the motor must be able to overcome the necessary stall torque. Preferably already at low voltage, to reduce the effects of current spikes. Stall torque is the torque generated by the DC motor when its rotational speed is zero. The motor connects to the bolt and nut coupling system in this drug delivery system. This mechanism depends on friction among various components, which increases the motor's load and requires sufficient stall torque. Insufficient torque may cause the reorientation and injection systems to malfunction. Additionally, the highly acidic gastric fluid could increase friction between components due to material deterioration.

The rotation speed of the motor shaft directly affects the movement speed of the bolt and nut coupling system. However, excessive speed can lead to momentum within the movement, which may cause control overshoot or device instability. Therefore, when selecting a specific motor gear ratio we need to carefully consider the relationship between rotation speed and reliability. To conclude, the Sub-Micro Plastic Planetary Gearmotor from Pololu offers an easily integratable motor that enables rapid control in both directions. A significant advantage of this specific motor is its versatility in the actuator system design, allowing us to choose an appropriate gear ratio according to the mechanism's requirements later on. We will further explore the relationship between the gear ratio and the overall actuator system in Chapter 5.

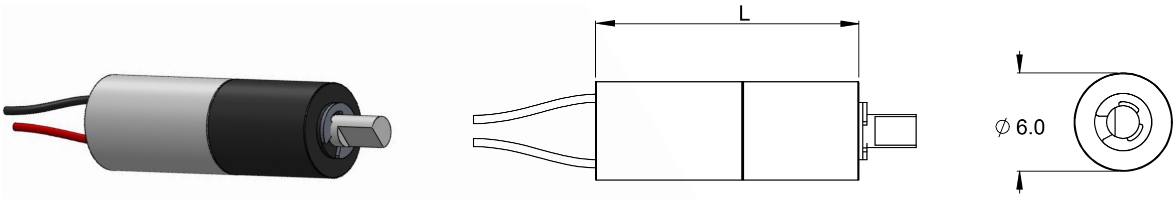

Gear ratio	26:1	136:1	700:1
Length (L)	16.0mm	19.0mm	21.0mm
Nominal Voltage	.3-9V	.3-9V	.3-9V
Stall torque	0.1kg-cm	0.6kg-cm	0.8kg-cm
No-load Speed	2500rpm	500rpm	90rpm

Table 3-3: Dimensions in mm and key specification at 6V of the Sub-Micro Plastic Planetary Gearmotors by Polulu [58].

3-3-4-5 H-Bridge for Microactuator Control

The H-bridge allows for bidirectional motor control, enabling the DC geared motor to provide rotation in both directions which is important to facilitate both folding as unfolding. Furthermore, the H-bridge facilitates pulse width modulation (PWM) based voltage control which comes in handy when wanting to control the motor under voltage ranges that cannot be facilitated by the DC-DC converter. In our case, we utilize the H-bridge for voltage ranges under 0.8V, this is which is particularly useful for fully stopping the microactuator. The DRV8220EVM from Texas Instruments™ (TI) was selected for its high efficiency, exceptional time resolution of less than 1 microsecond, and robust protection features. These protection features, including overcurrent, thermal, and undervoltage protection, help prevent motor and system component damage., thermal, and undervoltage protection, which safeguard the motor and system components from potential damage.

3-3-4-6 Voltage Converter for Microactuator Control

A DC-DC voltage converter is an electronic circuit that converts a DC voltage level from one value to another. In the context of our ingestible device, the primary function of the DC-DC converter is to control the actuator, necessitating a stable and energy-efficient component to ensure consistent operation and extend battery life. Consequently, we selected the MAX77643 from Maxim Integrated™ as the dcdc converter for its high integration level, compact size, high efficiency, and flexible voltage supply management capabilities.

The MAX77643 integrates a high-efficiency step-down converter, low-dropout regulators, and an overvoltage protection circuit in a compact package, which contributes to a reduced overall device footprint. This level of integration makes it an ideal choice for our space-constrained application. Furthermore, the MAX77643 offers up to 91% peak efficiency for the step-down converter, allowing for extended battery life and decreased heat dissipation. Its wide output voltage range (0.8V to 5.5V) ensures compatibility with various microactuators, enabling control over speed and torque. Additionally, the device includes programmable output voltage settings, facilitating precise control over the voltage supply to the microactuator. This feature optimizes performance and protects sensitive components from potential overvoltage or undervoltage damage.

3-3-5 Powering the Ingestible Device

To power our system, we selected the CR1025 Renata battery with a standard discharge voltage of 3V and a rated capacity of 30mAh. We chose the CR1025 Renata as our silver oxide battery (SOB) for its high nominal voltage, rated capacity, and round shape, which nicely fits the cylindrical-shaped main body of the device [59]. As shown in Figure 3-3, the battery can be placed on top of the main body.

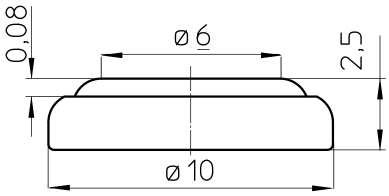

Figure 3-15: Dimensions of the CR1025 Renata in mm [56].

The total stored energy in the two non-rechargeable CR1025 Renata SOBs (E_{batt}) can be calculated using the number of batteries (N), nominal voltage (Voc) in Volt [V], and rated capacity (C_{batt}) in milliampere-hour [mAh]: $E_{\text{batt}} = N \cdot V_{\text{oc}} \cdot C_{\text{batt}} = 2 \cdot 3 \cdot 30 = 180$ milliwatt-hour [mWh]. Furthermore, 180mWh is equal to 648 joules [J] or watt-second [Ws].

The CG-320B/M3 by Panasonic is a suitable lithium-ion battery (LIB) for our experiments due to its high cycle life, nominal voltage of 3.7V, and rated capacity range of 90-240mAh. Additionally, this battery has a self-discharge time of 3 years, making it an efficient option for experimental use. However, there are safety risks associated with using LIBs, such as the risk of thermal runaway, which necessitates a mandatory protection circuit for safe operation.

Table 3-4: Summary of the battery types of the thesis: Renata CR1025 SOB, and the CG-320B/M3 by Panasonic LIB.

Battery type	Cycle life	V_{oc} [V]	C_{batt} [mAh]	Safety risks	Applications
CR1025 (SOB)[60,61]	N/A	3	30	Hazardous when ruptured	Implantable and ingestible
CG-320B/M3 (LIB)[60–62]	500-2000	3.7	90-240	Risk of thermal runaway; requires a protection circuit	Implantable

In conclusion, the CR1025 Renata silver oxide battery provides a suitable power source for our ingestible device, offering high nominal voltage, rated capacity, and a shape that fits well within the system's design constraints. Utilizing the CG-320B/M3 for experimental purposes allows for more practical testing while maintaining the overall performance and design goals of the final system.

Chapter 4

Sensing and Data-processing

In this chapter, we focus on our first research challenge described in Section 2-2-1:

- *Develop a* ***sensor system*** *that is accurate, robust, and energy-efficient to provide high-quality data for decision making and actuator control.*

After providing context to the challenges of our sensor system in Section 4-1, we discuss our approach to overcoming them in the rest of the chapter. Subsequently, we delve into the theory on and justify the data processing methods that we intend to utilize in our data processing pipeline, specifically on calibration in Section 4-2 and signal processing in Section 4-3. Then, in Section 4-4, we describe and justify the development of our final processing pipeline, including our testing methodology and parameter selection. Lastly, we present the results of our final sensor system in Section 4-5.

As a refresher to Section 3-3 and to provide more direction for this chapter, an overview of the focus group of this chapter is presented in color in Figure 4-1.

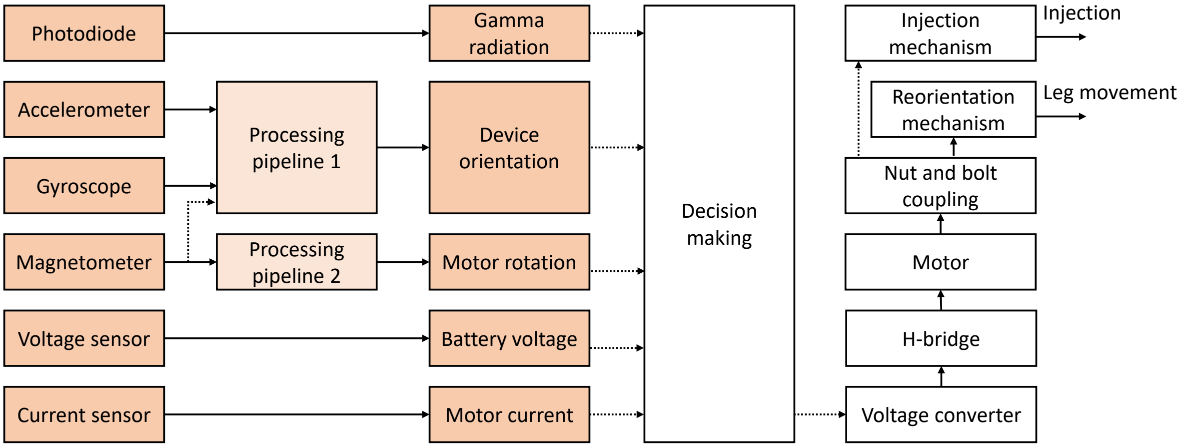

Figure 4-1: Component overview of the closed-loop reorientation and injection system, highlighting the focus of this chapter in color: the sensor system.

> **Research Contribution to the Sensor System Development**
> This chapter is dedicated to the design, development, and testing of the data processing pipelines, which were realized through the sole contribution of the author.

4-1 Errors and Limitations of the Sensor Systems

In this section, we will examine the errors and limitations of sensor systems, focusing on common sensor error types, component characteristics, and their impact on the overall system performance. By understanding these issues, we can develop strategies for mitigating their effects and enhance the accuracy and reliability of our sensor system.

4-1-1 Common Sensor Error Types

For the decision making process to be as reliable as possible we need to make sure that its input data is as accurate as possible. However, in practice, raw sensor data is never fully free of noise, due to internal sensor errors but also external influences. In our case, movement artifacts and temperature differences are known to attenuate sensor signals, resulting in significant noise [63]. Sensor error can greatly impact the ability to extract useful information from the data. To better understand the errors that can affect our system, we will examine the most common types of sensor error, specifically focusing on bias, scale factors, and random noise.

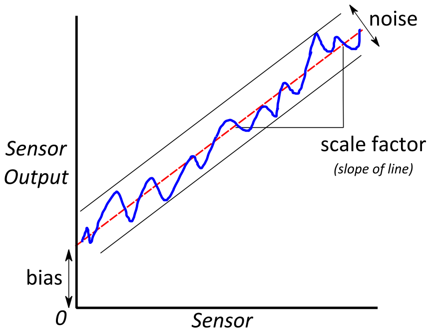

Figure 4-2: Common sensor error types.

Bias is a constant difference between the measured output of the sensor and the actual value of the physical input. This can be illustrated by the example of an IMU that is stationary and level, where the vertical axis should measure the effect of gravitational acceleration with a nominal value of 9.81 m/s^2. However, if the measurement is biased, the IMU may report a value such as 9.72 m/s^2, resulting in a bias error. The accuracy of the sensor can be improved by calibrating the sensor before use.

Scale factor error describes the relationship between the input and output of the sensor, which ideally should be linear. However, due to scale factor error, the actual output may be proportional to the input but scaled by a factor. For instance, if the input is 10 m/s^2, but there is a 5% scale factor error, the output measurement may be 10.5 m/s^2, resulting in a 50,000 ppm error. Scale factor errors can also be mitigated by performing appropriate calibration before use.

Sensor noise refers to the inherent random fluctuations or errors in the measurements obtained from a sensor. Signal filtering techniques, such as low-pass, high-pass, or band-pass filtering, can be used to attenuate high-frequency noise and isolate the relevant signal components. Signal averaging can also be employed to reduce the impact of random noise in the measurements by averaging multiple readings of the same variable. Additionally, statistical signal processing techniques, such as Kalman filtering or particle filtering, can be used to estimate the underlying signal from noisy measurements. These methods leverage statistical models of the system to estimate the true state of the system, even in the presence of noise. The choice of filter should be carefully considered, as they can strongly differ in their precision and computational load. For this reason, we will further investigate filtering methods in Section 4-3.

4-1-2 Component Characteristics and Limitations

In this section, we discuss the characteristics and limitations of our sensor system. We do this by focusing on an individual sensor or the microcontroller unit (MCU) in each subsection.

4-1-2-1 Limitations of the Inertial Measurement Unit for Orientation Estimation

As mentioned in Section 3-3-2-2, we aim to utilize the inertial measurement unit (IMU) for orientation and motor speed monitoring. Specifically, the gyroscope enables tracking changes in pitch, yaw, and roll, the accelerometer allows for pitch and roll estimation with reference to the Earth, and the magnetometer allows us to estimate yaw with reference to the Earth's magnetic field or tracking of motor rotations depending on whether we place a magnet on the motor.

In theory, we should be able to fully track the movement of our device solely through the use of the gyroscope by estimating a new position based on the previous position and the change in angle, a process known as dead reckoning. However, in practice, sensors are never free of noise, which leads to small errors in the measurements. In dead reckoning, this error accumulates over time, causing drift as illustrated in Figure 4-3.

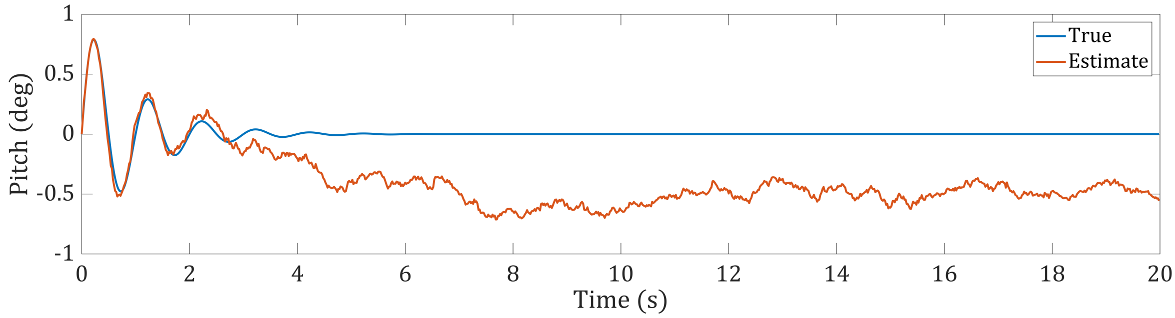

Figure 4-3: Simulation illustrating gyroscope drift.

Alternatively, we can use the magnetometer and accelerometer, where errors are not accumulated since estimations are not based on the previous step. However, in this case, the accelerometer introduces strong high-frequency errors due to double integration, as depicted in Figure 4-4.

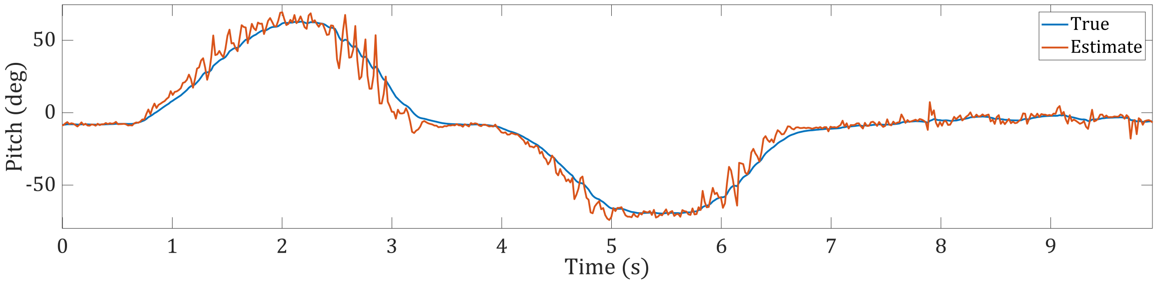

Figure 4-4: Simulation demonstrating accelerometer high-frequency error.

4-1-2-2 Limitations of the PIN Photodiode for Gamma Radiation

The PIN Photodiode typically does not require any filtering, as noise is relatively low compared to the threshold used for gamma radiation detection. More on this in Section 6-2-2.

4-1-2-3 Limitations of the Power Monitor for Voltage and Current Draw

Similarly to the PIN Photodiode, the noise of the power monitor is relatively low compared to the data accuracy that we require for decision making. The INA219 is capable of measuring voltage with a resolution of 1.25 mV and measuring current with a resolution of 0.1 mA, while our decision making will be based on a 0.1V range and 1A range. More on this in Section 6-2-1 and Section 5-5.

4-1-2-4 Insight into the Microcontroller Unit for Data Processing

The incorporation of a MCU in our system is driven by the need for a compact device with low power consumption and high-speed data processing capabilities. However, MCUs have limitations concerning real-time data processing, primarily due to their restricted processing power, random-access memory (RAM), and flash memory. For instance, the microprocessor utilized in our system features only a single processor, which limits parallel computing tasks such as running algorithms and collecting sensor data simultaneously.

Considering these limitations, we must account for the computational burden of algorithms when selecting and developing them. In addition to processing power constraints, the limited memory capacity of MCUs can also pose challenges in handling large data sets. After computational efficiency, preference should be given to algorithms that consume minimal memory resources.

4-2 IMU Calibration for Bias Correction

In order to mitigate bias and scale factor error, calibration of our device is necessary. While calibration of IMU systems typically involves executing a step-by-step program prior to sensor usage, which includes comparing IMU estimations with real movement, our device must be operational without necessitating any human intervention. Furthermore, transitioning from an external environment to the gastric environment can affect sensor dynamics, warranting additional calibration once inside the stomach.

Since reliable movement of the mechanism within the stomach is infeasible, we must focus on stationary calibration methods. Unfortunately, this precludes addressing scale factor errors and only allows for bias removal. Common approaches for bias removal include estimating the mean of the function and eliminating the offset that indicates movement. For gyroscopes, this involves estimating the mean to identify the offset. In the case of accelerometers, the process is more complex due to the constant influence of gravity on readings. Thus, gravity components must first be estimated from the sensor by identifying the direction of gravity and removing 9.80665 m/s^2 from that direction. Once gravity is known, it can be removed from sensor readings to estimate the mean offset. The calculated mean offset can then be utilized to calibrate IMU readings.

For magnetometers, calibration to remove hard iron and soft iron distortions is necessary. Hard iron distortions are caused by magnetic fields unrelated to the Earth's magnetic field, while soft iron distortions arise from the magnetometer's sensitivity to the magnetic field's orientation. Magnetometer calibration would require collecting measurements while rotating the sensor in various orientations. Since reliable device rotation is unachievable, magnetometer calibration will not be performed.

Gyroscope calibration entails estimating the mean offset **b_gyr** by measuring stationary sensor output:

$$\mathbf{b\_gyr} = \frac{1}{N}\sum_{i=1}^{N} \boldsymbol{\omega_i}, \tag{4-1}$$

where $\omega_{\mathbf{i}}$ represents a vector containing the raw gyroscope output in the stationary state in the x, y, and z directions and N is the number of samples taken.

For accelerometer calibration, the mean offset **b_acc** is estimated by first removing the gravity component from sensor readings and then calculating the mean of the stationary output:

$$\mathbf{a}' = \mathbf{a} - \mathbf{g}, \tag{4-2}$$

where **a** represents the raw accelerometer output in the stationary state in the x,y,z direction and **g** is the estimated direction of gravity. The mean offset is then calculated as:

$$\mathbf{b\_acc} = \frac{1}{N}\sum_{i=1}^{N} \mathbf{a}'_{\mathbf{i}}. \tag{4-3}$$

The mean offset can then be employed to digitally calibrate sensor readings:

$$\begin{aligned} \boldsymbol{\omega_c} &= \boldsymbol{\omega} - b_{\boldsymbol{\omega}} \\ \mathbf{a_c} &= \mathbf{a}' - \mathbf{b\_acc}, \end{aligned} \tag{4-4}$$

where $\boldsymbol{\omega}$ and **a** are the raw gyroscope and accelerometer outputs, respectively, and $\boldsymbol{\omega_c}$ and $\mathbf{a_c}$ are the calibrated outputs.

Next, we can rewrite these equations into Algorithm 1 and Algorithm 2, to allow for onboard computation by the MCU. Algorithm 1 takes in the raw accelerometer array **A** and gyroscope array $\boldsymbol{\Omega}$ from an IMU sensor, and returns the accelerometer bias **b_acc**, gyroscope bias **b_gyr**, and gravity vector **g**. Algorithm 2 takes in a matrix X of size $m \times n$, and returns a vector $\overline{\mathbf{x}}$ of size m containing the mean of each row of X.

```
Algorithm 1: IMU Calibration with Accelerometer-Based Tilt Sensing
  Input: Accelerometer array $\mathbf{A}$, gyroscope array $\boldsymbol{\Omega}$
  Output: Accelerometer bias $\mathbf{b\_acc}$, gyroscope bias $\mathbf{b\_gyr}$, gravity vector $\mathbf{g}$
  $\mathbf{g} \leftarrow 9.80665 * \text{mean\_rows}(\mathbf{A})/|\mathbf{A}|$
  $\mathbf{b\_gyr} \leftarrow \text{mean\_rows}(\boldsymbol{\Omega})$
  $\mathbf{b\_acc} \leftarrow \text{mean\_rows}(\mathbf{A}) - \mathbf{g}$
  return $\mathbf{b\_acc}, \mathbf{b\_gyr}, \mathbf{g}$
```

```
Algorithm 2: Mean of Rows Calculation
  Input: Matrix $X$ of size $m \times n$
  Output: Vector $\overline{\mathbf{x}}$ of size $m$ containing the mean of each row of $X$
  $\overline{\mathbf{x}} \leftarrow \text{zeros}(m)$
  for $i \leftarrow 1$ to $m$ do
      $\overline{\mathbf{x}}(i) \leftarrow \frac{1}{n}\sum_{j=1}^{n} X(i,j)$
  end
  return $\overline{\mathbf{x}}$
```

4-3 Signal Processing Techniques

4-3-1 Enhanced Orientation Estimation through Sensor Fusion

4-3-1-1 Importance of the Orientation Representation Method

Orientation estimation methods are developed within the context of specific orientation representations. An orientation representation is a mathematical construct used to describe the orientation of a rigid-body in three-dimensional space. Choosing a suitable orientation representation is an essential first step to ensure reliability and computational efficiency. Various methods of attitude representation exist, each with its own advantages and disadvantages. In this section, we focus on the well-known Euler angles representation and the unit quaternion representation.

The most well-known method of describing orientation is through a set of three Euler angles. Euler angles match the intuitive human visual representation of movement, making them easy to understand and use [64]. Movement in the Euler angle representation is commonly described through Tait–Bryan angles: pitch, roll, and yaw, denoted by ϕ, θ, and ψ. This terminology further enhances the intuitiveness of Euler angles. Even when attitude estimation is performed using another orientation model, the final visual representation is often converted back to Euler angles for clarity.

The problem with this parameterization is that it has singularities at pitch values of $\theta = \frac{\pi}{2} + k\pi$, with $k \in \mathcal{Z}$. In the case of orientation estimation, singularity would result in the estimator being unable to distinguish pitch, roll, and yaw from each other, leading to highly inaccurate orientation estimation. This phenomenon is also known as gimbal lock. To overcome these singularities, other attitude representations have been developed, such as quaternions and rotation vectors [65].

In this thesis, we focus on the quaternion representation. Quaternion representations are free of singularities and computationally less demanding than Euler-based orientation estimation models. A quaternion is a 4-tuple that extends complex numbers with broad applications in mathematics, particularly in representing orientation and rotation. The fundamental idea is that each rotation can be represented as a rotation around a single axis (a vector in space) by a specific angle. Given such an axis $K = [k_x, k_y, k_z]^T$ and an angle θ, one can calculate the so-called Euler parameters or unit quaternion:

$$q_1 = k_x \sin\tfrac{\theta}{2} \; q_2 = k_y \sin\tfrac{\theta}{2} \; q_3 = k_z \sin\tfrac{\theta}{2} \; q_4 = \cos\tfrac{\theta}{2}. \tag{4-5}$$

These four quantities are constrained by the relationship

$$q_1^2 + q_2^2 + q_3^2 + q_4^2 = 1. \tag{4-6}$$

Multiplying two quaternions requires only 16 multiplications and 12 additions, in contrast to multiplying two rotation matrices, which necessitates 27 multiplications and 18 additions. This makes quaternion operations computationally more efficient. Moreover, the quaternion representation does not suffer from singularities for specific joint angles, making the approach computationally more robust. In the physical world, this means that quaternions are not prone to gimbal lock. However, the constraint on the norm of unit quaternions makes them challenging to include in estimation algorithms. For iterative optimization algorithms, this is often solved by simply re-normalizing the quaternions after each iteration. Nonetheless, each normalization results in information loss and introduces errors. In our case we will save the data in a 16-bit configuration, resulting in a worst-case data loss of 0.1%. As we aim for our accuracy to be within a 5-degree range, we regard this loss of data as negligible without compromising computational complexity.

4-3-1-2 Sensor-fusion

As discussed in Section 4-1-2, a gyroscope can estimate the orientation through dead reckoning. However, gyroscopes are prone to drift, causing their values to deviate over time. In contrast, an accelerometer can measure the device's position relative to the Earth without error accumulation, but it is susceptible to high-frequency errors, and distinguishing gravitational pull from linear acceleration can be challenging.

Sensor fusion addresses these issues by combining data from both sensors to complement each other. In our example, the gyroscope tracks rapid changes in orientation, while the accelerometer compensates for error accumulation. A common filter for data fusion is the Kalman Filter, but it requires substantial computational power, which is unsuitable for our ingestible system.

Quaternion-based complementary filters can be employed instead of relying on Euler angle-based inputs. The Mahony filter is an example of a complementary filter using quaternion representation, which estimates the direction of gravity from the accelerometer and calculates the error signal by taking the cross product between the estimated direction and the measured direction of field vectors [66]. Another alternative is the Madgwick filter, which uses a gradient descent algorithm to approach the gravity component and is optimized using a Newton optimization method that computes the gradient directly from the quaternion representation of motion [67].

A comparison between the Mahony and Madgwick filters reveals that the Madgwick filter requires fewer mathematical operations, resulting in a lower computational load. Moreover, accuracy results demonstrate that Madgwick outperforms Mahony in heading orientation, as evidenced by the lower error root-mean-square error (RMSE) of the Euler angles compared to the ground truth. However, Mahony's execution time is not necessarily shorter than Madgwick's, taking approximately 5% longer [68]. Consequently, we selected the Madgwick filter due to its superior accuracy and lower computational load.

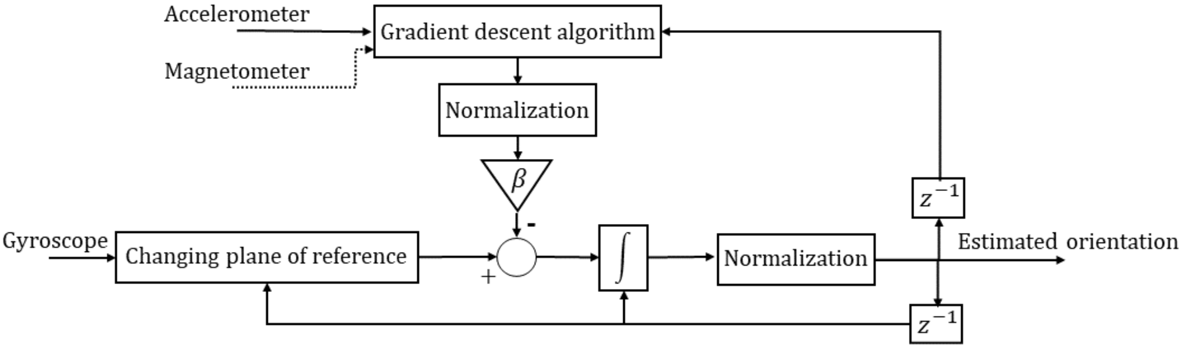

Figure 4-5: Madgwick filter block diagram.

Figure 4-8 illustrates a block diagram of the Madgwick filter. The system comprises a block named Gradient Descent Algorithm, a Newton optimization method that computes the Jacobian of a function. In this instance, it calculates the Jacobian of the previously estimated quaternion and the reference direction of Earth's magnetic field. The Jacobian is subsequently multiplied by the raw accelerometer data to estimate the direction of gravity, which is added to the gyroscope data by the weighted factor, and then normalized. In equation form, the Madgwick filter can be described as

$$\boldsymbol{q}_{k+1} = \boldsymbol{q}_k + \frac{1}{2}\boldsymbol{q}k \otimes \boldsymbol{\omega}\Delta t - \beta\frac{\nabla f(\boldsymbol{q}_k)}{||\nabla f(\boldsymbol{q}_k)||}\Delta t, \tag{4-7}$$

where $\boldsymbol{q}_{k+1}$ is the updated quaternion orientation at time step $k+1$, $\boldsymbol{q}_k$ is the quaternion orientation at time step k, $\boldsymbol{\omega}_{measured}$ is the measured angular velocity from the gyroscope, Δt is the time step interval between two consecutive measurements, β is the weighted factor used to blend the accelerometer and gyroscope data, $\nabla f(\boldsymbol{q}_k)$ is the gradient of the objective function from the accelerometer data with respect to the quaternion orientation at time step k, and $||\nabla f(\boldsymbol{q}_k)||$: The magnitude of the gradient vector.

Similarly to the figure, the equation shows how the quaternion orientation is updated using the measured angular velocity and the gradient of the objective function with respect to the quaternion orientation. The term $\frac{1}{2}\boldsymbol{q}\boldsymbol{k} \otimes \boldsymbol{\omega measured}\Delta t$ represents the integration of the gyroscope data, while the term $-\beta\frac{\nabla f(\boldsymbol{q}_k)}{||\nabla f(\boldsymbol{q}_k)||}\Delta t$ represents the correction applied to the quaternion orientation using the accelerometer data, weighted by the factor β. In this way, the Madgwick filter combines the gyroscope and accelerometer data to obtain an accurate and stable estimation of the orientation, overcoming the individual limitations of each sensor.

4-3-1-3 Limited Benefit of the Magnetometer for Reorientation, and the Final Madgwick Filter Description

Magnetometers are typically employed to determine a device's yaw angle. However, the cylindrical shape of our device allows for reorientation without affecting the injection mechanism, rendering the use of a magnetometer unnecessary. Furthermore, although yaw estimation can enhance the accuracy of Earth's position estimation by rectifying accelerometer input, the potential benefits of a magnetometer do not significantly improve roll and pitch estimation for the Madgwick filter. Results show that the improvement in estimation accuracy is less than 1% [67].

Considering the negligible benefits of using the magnetometer for yaw estimation, we have decided to exclude it from our final motion tracking pipeline. This decision reserves the magnetometer for alternative applications, such as motor tracking. Now that we have fully described our wanted complementary filter, we can look into its onboard implementation. For that, we constructed the following algorithm:

Algorithm 3: Madgwick Filter Algorithm

```
Input: Quaternion estimate $\mathbf{q}$, accelerometer signal $\mathbf{a}$, gyroscope signal $\boldsymbol{\omega}$, time step
       $t\_step$, tuning parameter $\beta$
Output: $\mathbf{q}$
Function Madgwick($\mathbf{q}, \mathbf{a}, \boldsymbol{\omega}, t\_step, \beta$):
    $f \leftarrow \begin{bmatrix} 2(q_2q_4 - q_1q_3) - a_x \\ 2(q_1q_2 + q_3q_4) - a_y \\ 2(0.5 - q_2^2 - q_3^2) - a_z \end{bmatrix}$
    $J \leftarrow \begin{bmatrix} -2q_3 & 2q_4 & -2q_1 & 2q_2 \\ 2q_2 & 2q_1 & 2q_4 & 2q_3 \\ 0 & -4q_2 & -4q_3 & 0 \end{bmatrix}$
    $f\_grad \leftarrow J^\top \cdot F$                          // Accelerometer gradient descent
    $f\_grad \leftarrow f\_grad / \|f\_grad\|$                   // Normalize
    $\mathbf{q\_dot\_gyr} \leftarrow 0.5 \cdot \mathbf{q} \otimes [0\ \omega_x\ \omega_y\ \omega_z]$    // Change gyro plane of reference
    $\mathbf{q\_dot} \leftarrow \mathbf{q\_dot\_gyr} - \beta \cdot \nabla f^\top$    // Combine gyroscope and accelerometer
     estimation
    $\mathbf{q} \leftarrow \mathbf{q} + \mathbf{q\_dot} \cdot t\_step$    // Integrate and add to previous step
    $\mathbf{q} \leftarrow \mathbf{q} / \|\mathbf{q}\|$                  // Normalize
return $\mathbf{q}$
```

The algorithm takes in the current quaternion estimate of the device orientation ($\mathbf{q} = \begin{bmatrix} q_1 & q_2 & q_3 & q_3 \end{bmatrix}$), the accelerometer measurement ($\mathbf{a} = \begin{bmatrix} a_x & a_y & a_z \end{bmatrix}$]), the gyroscope measurement ($\boldsymbol{\omega} = \begin{bmatrix} \omega_x & \omega_y & \omega_z \end{bmatrix}$), the time interval between measurements (t_step), and a tuning parameter (β).

4-3-2 Moving Average Filtering for Data Cleaning

The moving average algorithm is a prevalent technique in signal processing employed to smooth noisy data. It involves calculating the average of a specified window of data points, which shifts along the time series. The smoothed data is then utilized for further analysis or visualization. The equation for the moving average algorithm can be expressed as:

$$MA = \frac{1}{n} \sum_{i=1}^{n} x_i, \tag{4-8}$$

where MA represents the moving average, x_i denotes the sensor input data points at step i, and N is the window size. The conventional approach to calculating the moving average involves maintaining a running sum of the last N data points. As each new data point is added, the oldest data point in the window is removed from the sum. The moving average is then computed by dividing the running sum by N. This approach necessitates the storage of all N data points and the computation of $N-1$ additions and a division for each step.

To address these limitations, a computationally efficient method has been proposed that requires no storage of previous data values and minimizes divisions. This method involves subtracting the mean at each time step and adding in the newest data point, as follows:

$$MA[i] = MA[i-1] + \frac{x[i] + MA[i-1](N-1)}{N} \tag{4-9}$$

Specifically, a single division, subtraction, and two shifts are required, making it suitable for implementation on simple microcontrollers with limited computational resources. Finally, we can implement the moving average filter into our MCU through the following algorithm:

Algorithm 4: Moving Average Filter

```
Input: Signal $x$, filter length $w$
Output: Moving average $x\_avg$
Initalize: $x\_avg \leftarrow 0$
Function MovingAverage($x, w$):
    if $i < w$ then
        $x\_avg \leftarrow (x + x\_avg * (i-1))/i$
        $i \leftarrow i + 1$
    end
    else
        $x\_avg \leftarrow (x + x\_avg * (N-1))/N$
    end
return $x\_avg$
```

The algorithm takes in an input signal x and the filter length N. It returns the moving average of the input signal, denoted by x_avg. The algorithm initializes x_avg to zero, and then iterates over each sample of the input signal.

If the index i is less than the filter length N, the moving average is computed as the weighted sum of the current sample x and the previous moving average x_avg. The weight given to the current sample is $\frac{1}{i}$, while the weight given to the previous moving average is $\frac{i-1}{i}$. The variable i is then incremented by one.

If the index i is greater than or equal to N, the moving average is computed as the weighted sum of the current sample x and the previous $N-1$ samples. The weight given to the current sample is $\frac{1}{N}$, while the weight given to each of the previous $N-1$ samples is $\frac{1}{N}$. The filter length N represents the number of samples over which the moving average is computed.

4-3-3 Peak Detection for Data Extraction

In the field of signal processing, peak detection algorithms are commonly employed to extract periodic information from signals. These algorithms detect peaks in a signal that meet certain conditions and return their absolute value and the time at which they occurred. Various peak detection algorithms exist, and they rely on different properties of signals. Some of the commonly used methods include threshold peak detection, Z-score peak detection, and wavelet-based peak detection.

Threshold peak detection is the simplest technique for identifying peaks, which involves establishing a threshold value. Any value above the threshold is considered a peak. This method is well-suited for capturing and monitoring high-speed motor rotation, as it can swiftly pinpoint signal peaks without performing complex calculations. Mathematically, threshold peak detection can be expressed as:

$$\textbf{if } x_i > threshold, \textbf{ then} \text{ peak detected at } x_i, \tag{4-10}$$

where x_i represents the data point at timestep i.

Our system's objective is to effectively capture high-speed motor rotation, wherein each cycle produces identical magnetometer signals. Given that the cycle remains relatively constant, with no significant amplitude changes, we can employ a threshold-based peak detection system. This approach is computationally less demanding compared to Z-score peak detection and wavelet-based peak detection alternatives. Considering our limited processing capabilities, we deem the threshold-based peak detection as the appropriate peak detection algorithm for our system.

4-4 Post-Processing Pipelines

Now that we have defined the data processing techniques that we want use in our sensor system, we can specifically look into the data processing pipeline for each wanted sensor output. We start with a description of the simple processing pipelines of the gamma sensor and power monitor.

4-4-1 Pipeline for Gamma Radiation, Battery Voltage and Motor Current Draw Monitoring Using PIN Diode and Power Monitor Data

As mentioned in Section 4-1-2, the raw sensor outputs of the PIN diode and power monitor are sufficiently accurate for our decision making system without the need for extensive data processing. However, we apply a moving average filter to the gamma radiation and battery voltage data to improve robustness against outliers and ensure reliable decision making. This is important because we will use threshold-based flowchart in the decision making, meaning a single outlier can result in a false positive and significantly impact the decision making system's reliability. Therefore, a moving average filter with a window size of N=10 is applied to both the gamma radiation and battery voltage data to smoothen the signals and reduce the effect of outliers.

On the other hand, the current measurement data is used for motor control, where minimizing delay is essential. In this scenario, a single outlier is less likely to significantly impact the decision making or motor control process. Instead, a quick response is more critical. Therefore, we opt to read the current data without any additional post-processing.

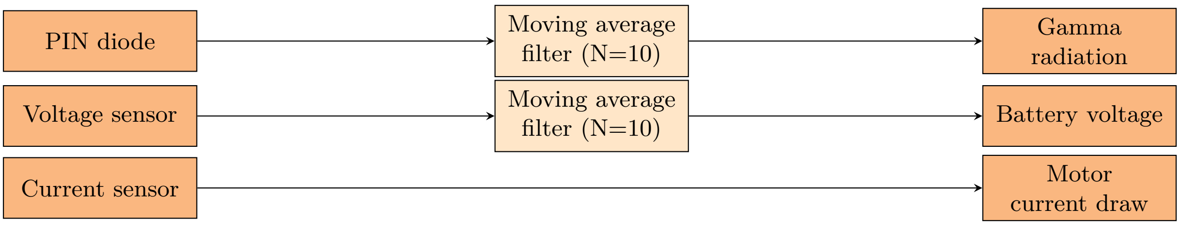

Figure 4-6: Processing pipelines for gamma radiation, battery voltage, and motor current sensing.

4-4-2 Pipeline for Orientation Tracking Using Accelerometer and Gyroscope Data

Our objective is to develop an accurate orientation tracking system for the proposed gastric retention and injection mechanism. The orientation estimation pipeline as shown in Figure 4-7 consists of a digital calibration block for bias removal and the Madgwick filter for data fusion of the gyroscope and accelerometer data. Note that we chose not to use magnetometer data due to its negligible benefits, as discussed in Section 4-3-1-3.

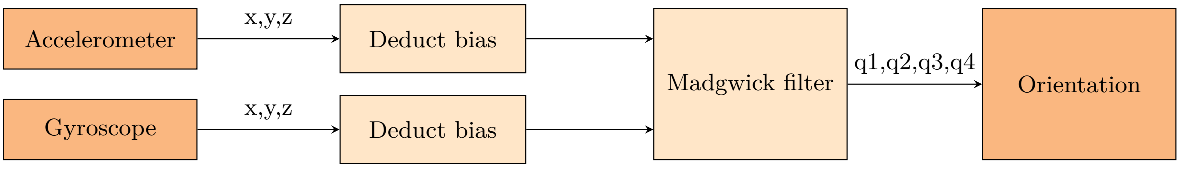

Figure 4-7: Processing pipelines pipeline orientation tracking.

Bias Removal: To ensure accurate orientation estimation, we first address the issue of bias in the IMU data. We digitally remove the calibration error before use, as described in Equation (4-4). This calibration step reduces the impact of bias on gravity direction and angular velocity estimations.

Initial Beta Value Selection: We select an initial beta value for the Madgwick filter based on the estimated mean zero gyroscope measurement error of each axis, $\tilde{\boldsymbol{\omega}}\beta$, after calibration [67]. We use the equation $\beta = \left|\frac{1}{2}\hat{\boldsymbol{q}} \quad \begin{bmatrix} 0 & \tilde{\omega}\beta & \tilde{\omega}\beta & \tilde{\omega}\beta \end{bmatrix}\right| = \sqrt{\frac{3}{4}}\tilde{\boldsymbol{\omega}}_{\beta}$, where $\hat{\boldsymbol{q}}$ is any unit quaternion. With this equation, we found a beta value of 0.0028. The low value is due to the high precision of the gyroscope, which therefore does not require much bias correction through the accelerometer gradient descent.

Test Simulation: We implement the Madgwick filter in a simulation environment with a known ground truth orientation. In this simulation, we induce motion are induced by a stepper motor attachment and manual intervention. For reorientation, we simulate a 90-degree change in pitch or yaw taking between 1 and 20 seconds, where 1 second represents the expected upper limit reorientation speed for the 136GR motor, and 20 seconds represents the lower limit for the 700 GR motor.

Tuning: We tune the Madgwick filter by iteratively adjusting the β value and evaluate the filter's performance in terms of accuracy, convergence rate, and stability. By comparing different β values, we found that higher β values $(0.1 - 0.01)$ resulted in a lower RMSE. We mainly observed that the orientation system suffered from overshoot during reorientation, which is a concern as we primarily want to use orientation estimation during reorientation to a standing position. We eventually found that a β of 0.05 effectively dampened the overshoot while still being able to distinguish linear movement from changes in orientation across all simulations.

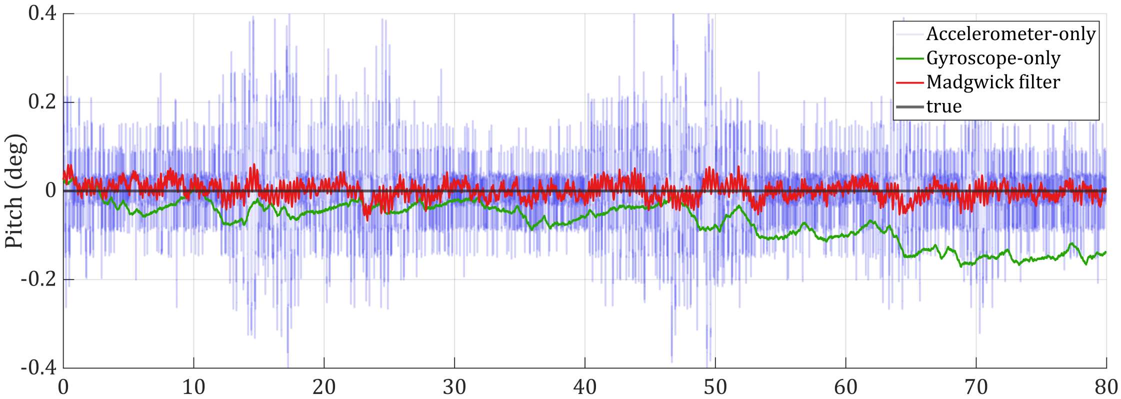

Figure 4-8: Madgwick filter pipeline output when stationary.

4-4-3 Pipeline for Motor Tracking Using Magnetometer Data

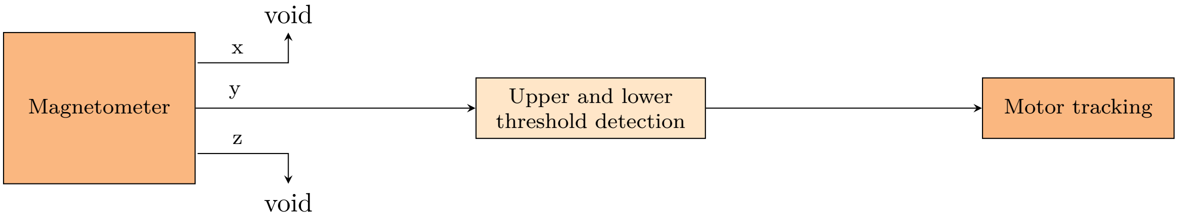

In our system, the peak detection algorithm is employed for tracking the movement of the microactuator. The magnet is strategically placed on the rod of the microactuator to facilitate the measurement of the motor's rotations. By doing so, the magnet's movement becomes relatively fixed, allowing us to employ a computationally efficient standard threshold-based peak detection algorithm.

In order to effectively prevent multiple peak detections before the completion of a full rotation, we incorporate an upper and lower threshold in the peak detection algorithm. This ensures that only when the signal exceeds both thresholds, a single peak is detected. Algorithm 5 demonstrates the proposed double threshold peak detection method.

Algorithm 5: Upper and Lower Threshold Algorithm

```
Input: Signal $x$, Lower threshold $T\_low$, Upper threshold $T\_up$
Output: Peaks $p$
Initalize: $p \leftarrow 0, state \leftarrow 0$
while $x = true$ do
    if $x < -T\_low$ and $state = 0$ then
        $state \leftarrow 1$
    else
        if $x > T\_up$ and $state = 1$ then
            $p \leftarrow p + 1$
            $state \leftarrow 0$
        end
    end
end
return $p$
```

The algorithm accepts a signal x, a lower threshold T_low, and an upper threshold T_up as inputs. It initializes the count of peaks p and a state variable, which is used to track the signal as it crosses the thresholds. The algorithm iterates through the signal, monitoring for instances where the signal goes below the lower threshold ($-T_low$) while the state is zero. Upon detecting such an instance, the state is updated to one. Following this, if the signal surpasses the upper threshold (T_up) while the state is one, a peak is detected, the count of peaks (p) is incremented, and the state is reset to zero. The process continues until the end of the signal, after which the algorithm returns the count of peaks (p).

4-5 Results and Findings

4-5-1 Orientation Tracking Accuracy Test

Table 4-1: Static and dynamic RMS error of Kalman-based algorithm and Madgwick filter.

Euler parameter	Madgwick Filter 9-DOF	Madgwick Filter 6-DOF
RMS $[\phi_\epsilon]$ static	1.204°	1.226°
RMS $[\phi_\epsilon]$ dynamic	2.432°	2.527°
RMS $[\theta_\epsilon]$ static	1.117°	1.212°
RMS $[\theta_\epsilon]$ dynamic	2.534°	2.491°

Our analysis showed no significant difference between the 9-degrees of freedom (DOF) Madgwick filter with a magnetometer and the 6-DOF Madgwick filter without a magnetometer. This flexibility allows us to repurpose the magnetometer for other applications as needed.

From the data shown in Table 4-1, the RMSE in the worst-case scenario is 2.5 degrees. As a benchmark, an error below 5 degrees should suffice to discern between a standing or falling position, implying our current system already delivers an acceptable performance.

Interestingly, there is a noticeable difference in RMSE between static and dynamic states. This is an important consideration for our decision making system, suggesting a need to pause after successful reorientation and before injection. During this pause, we can assess the orientation with greater accuracy, accounting for potential dynamic errors.

The current system design is based on literature findings, where the Madgwick filter was deemed the most computationally efficient quaternion-based filter. However, to confirm this, we should compare it with more sophisticated sensor fusion methods, such as Kalman-based quaternion filtering, in future studies [65].

4-5-2 Motor Tracking

We verified motor tracking for all three motor types using a high-speed camera. The algorithm was able to accurately track up to 50 cycles per second, which surpasses our projected need, as our system is likely to require at most 20 cycles for full unfolding.

In practice, maximizing the sampling frequency of our system would be an inefficient use of resources. According to the Nyquist-Shannon Sampling Theorem, to avoid aliasing, we should employ a sampling frequency that is at least twice the maximum frequency component of the signal we are sampling. Given that our system may reach a maximum unfolding speed of 20 rotations per second, we should utilize an update frequency of at least 40Hz in our system. This ensures accurate tracking while also optimizing computational efficiency.

Chapter 5

Actuation

In this chapter, we focus on the third research challenge described in Section 2-2-1:

- *Develop an* ***actuator control system*** *that ensures reliable and timely retention and injection, while maximizing battery operation time;*

We tackle this research challenge by modeling the actuator system and reformulating the challenge as a multi-objective optimization function in Section 5-1. Subsequent chapters focus on validating our actuator model and solving the multi-objective optimization function: Section 5-2 concentrates on the actuator constraints. Section 5-3 focuses on minimizing the energy consumption of the actuator system. Section 5-4 focuses on mitigating current peaks. Section 5-5 emphasizes enhancing control reliability. Finally, Section 5-6 presents the resulting actuator system.

To recall the content of Section 3-3-4, we provide an overview of the focus group of this chapter, depicted in green in Figure 5-1.

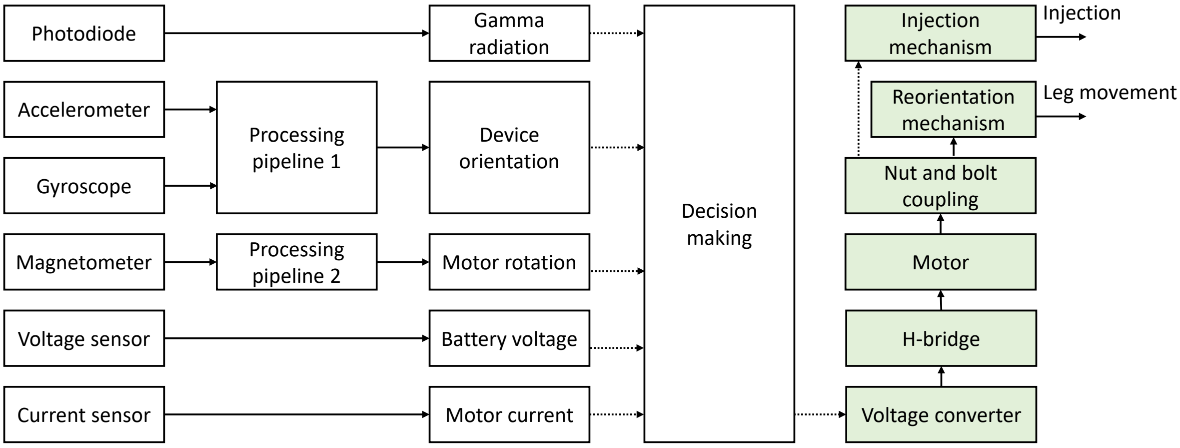

Figure 5-1: Component overview of the closed-loop reorientation and injection system, highlighting the focus of this chapter in color: the actuator system.

> **Research Contribution to the Actuator System Development**
>
> This chapter focuses on the usage and selection of the direct current (DC) geared motor for reorientation and injection. Herein, we utilize a mechanism prototype of the ingestible device for a 700GR motor developed by other researchers. The final energy estimation was carried out in collaboration with another thesis student. Apart from this aspect, the remaining content of this chapter is the exclusive contribution of the author.

5-1 Defining our Design Approach as an Optimization Problem

5-1-1 The Design Objectives and Multi-objective Optimization Problems

To provide a clear direction for the development of our actuator control system, we first break down the research question of this chapter into a set of design objectives:

1. Maximizing battery operation time, which consists of
    (a) Minimizing the actuator energy consumption from the battery $E_b \in \mathbb{R}$, measured in joules (J)
    (b) Minimizing the battery attenuation, which involves minimizing the current draw peaks $I_{b.peak} \in \mathbb{R}$, measured amperes (A)
2. Ensuring consistent retention and on-demand injection, which consists of:
    (a) Ensuring reliable actuation, such that the actuator can consistently overcome the torque applied by the environment $\tau_l \in \mathbb{R}_+$, measured Newmon-meter (Nm)
    (b) Ensuring prompt urgent care therapy, which involves minimizing the reorientation duration $t_{re} \in \mathbb{R}_+$, measured in seconds (s)

Our aim is to optimize the actuator system toward these design objectives. To do that, we must identify and adjust the free design parameters of our system such that they are optimized toward these design objectives. These free parameters are also known as the decision variables. From our component overview in Section 3-3-4, we deduce that there are three decision variables we can manipulate during the development of the actuator system:

- The motor gear ratio $n = \{5, 26, 136, 700\}$
- The motor voltage $U_m \in [0.8, 5.5] \subset \mathbb{R}$, measured in volts (V)
- The motor voltage ramp-up duration $t_{ramp} \in \mathbb{R}_+$, measured in seconds (s)

The set of available gear ratios results from the available gear ratios for the Sub-Micro Plastic Planetary Gearmotor from Pololu, discussed in Section 3-3-4-4. The voltages range results from the output voltage range of the direct current to direct current (DC-DC) converter, discussed in Section 3-3-4-6. The motor voltage and ramp-up duration can be controlled during motor operation through the DC-DC converter and H-bridge, while the motor gear ratio must be selected beforehand.

We can also describe the above-stated design objectives and parameters more formally as an optimization function. The full actuator system design process can then be described by consolidating these individual optimization functions into a multi-objective optimization problem (MOP) that we aim to solve. The mathematical formulation of an MOP is presented as follows [69]

$$\begin{aligned} \min \quad & \mathbf{F}(\mathbf{x}) = (f_1(\mathbf{x}), f_2(\mathbf{x}), \ldots, f_m(\mathbf{x})) & \\ \text{subject to} \quad & g_j(\mathbf{x}) \leqslant 0, & j = 1, 2, \ldots, p \\ & h_k(\mathbf{x}) = 0, & k = 1, 2, \ldots, q \\ & \mathbf{x} \in \mathbb{R}^n. & \end{aligned} \tag{5-1}$$

In this equation, $\mathbf{F}(\mathbf{x})$ denotes the vector of objective functions $f_i : \mathbb{R}^n \to \mathbb{R}$ for $i = 1, 2, \ldots, m$. The constraints are represented by inequality functions $g_j : \mathbb{R}^n \to \mathbb{R}$ and equality functions $h_k : \mathbb{R}^n \to \mathbb{R}$. The decision variables are given by $\mathbf{x} = (x_1, x_2, \ldots, x_n) \in \mathbb{R}^n$, which, in our case, include n, U_m, and t_{ramp}.

MOPs typically do not have a feasible solution that minimizes all objective functions simultaneously [70]. Instead, researchers focus on identifying the Pareto optimal solution, which is a solution that cannot be improved in any of the objectives without degrading at least one of the other objectives. After formulating the MOP, we will outline our approach to achieving the Pareto optimal front and justify our optimization method for reaching it.

The next step in our process is to create a model of the system that establishes a relationship between our design objectives and decision variables. Using this model, we can then fill in Equation (5-1) to obtain the MOP for our specific actuator system.

5-1-2 Modelling the Actuator System

We start by examining the energy consumption from the battery for a single full reorientation, focusing first on the energy consumption when operating under a constant motor driving voltage and assuming steady-state conditions. Later, we consider more transient aspects of actuator usage, such as initialization and end of movement.

Battery energy consumption: The energy consumption of the DC geared motor from the battery $E_b \in \mathbb{R}$ for motion from a fully closed to a standing position and injection is calculated as follows. Before electric power is delivered from the battery to the motor, it must be converted to an appropriate motor driving voltage. Efficiency losses occur during this voltage conversion by the DC-DC converter $\eta_{dcdc} \in [0, 1] \subset \mathbb{R}$, so the energy consumption from the battery by the DC geared motor can be calculated as:

$$E_b = \eta_{dcdc} E_m. \tag{5-2}$$

were η_{dcdc} can be estimated through an equivalent circuit model or measured empirically. Using the experimentally obtained values is also known as the lookup table method. Herein we chose the latter for simplicity reasons and time constraints.

The electrical energy consumption can be calculated by integrating the power consumption with respect to time $t \in \mathbb{R}$, $E = \int P(t)\mathrm{d}t$. Since we are modeling for energy consumption under steady-state conditions with a predefined duration t_{re}, we can simply calculate the energy consumption of the motor E_m as the product of the electric power consumption by the motor P_m and the time duration for reorientation t_{re}. Furthermore, P_m is a function of the motor driving voltage U_m and current $I_m \in \mathbb{R}$. Putting that all together we obtain

$$\begin{aligned} E_m &= t_{re} P_m \\ &= t_{re} U_m I_m. \end{aligned} \tag{5-3}$$

Rotation and injection duration: t_{re} is a function of the bolt thread length of the bolt-nut coupling $s_l \in \mathbb{R}_+$ in millimeter (mm), the pitch of the bolt nut coupling s_p, the angular velocity of the motor rod at the load $\dot{\theta}_l \in \mathbb{R}$ in radians per second (rad/s).

$$t_{re} = \frac{s_l}{\dot{\theta}_l s_p}. \tag{5-4}$$

From Section 3-3-4-2 we know that $s_p \in \{1, 1.5\}$, we will assume a pitch of 1mm as that is what was used in the current prototype. Furthermore, we know that s_l is directly related to the gear ratio of the motor because the motor length is located within the bolt and the longest component of the actuator system. This makes the motor the constraining factor for the length reduction of the bolt thread.

DC geared motor power consumption: To model the relationship between the energy consumption, input variables, and output variables, we utilize the full DC motor model for operation in the first and third quadrant only [71]. The quadrants of operation indicate in which direction velocity and torque are applied to the load by the motor. DC geared motors can provide motoring and break in both forward and reverse directions, thereby allowing four types of operations (Figure 5-2). When the motor is monitored it converts electrical energy into mechanical energy, which assists its motion. When the motor is breaking it converts mechanical energy into electrical energy, thus works as a generator and counteracts its motion. Because our battery system is not rechargeable we will ignore the regenerative capabilities of our motor, hence why we only consider the first and third quadrant in our DC geared motor model.

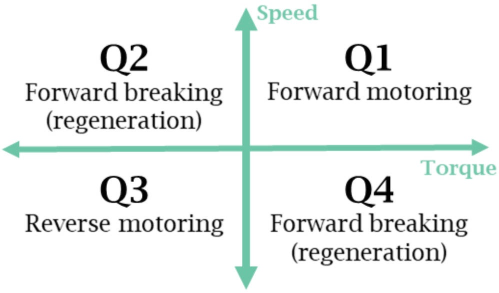

Figure 5-2: Four quadrant operations of the DC geared motor.

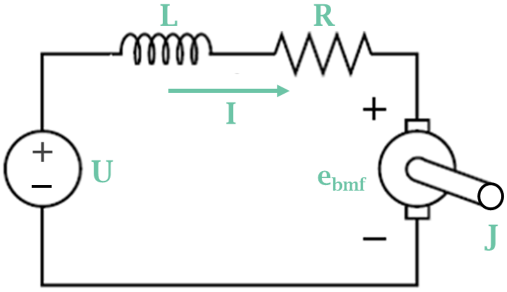

Figure 5-3: Circuit diagram of the DC geared motor.

We derive the voltage estimation equation from the circuit diagram (Figure 5-3) using Kirchhoff's law, resulting in the full motor model equation:

$$\begin{aligned} U_m &= L_m \frac{dI_m}{dt} + R_m I_m + e_{bemf} \\ I_m &= \frac{1}{k_t}(J\ddot{\theta}_m + \nu_m \dot{\theta}_m + \tau_m), \end{aligned} \tag{5-5}$$

where $L_m \in \mathbb{R}_+$ represents the inductance (H), $R_m \in \mathbb{R}_+$ represents the electrical resistance (Ω), and the back electromotive force $e_{bemf} \in \mathbb{R}$ is a force manifesting as a voltage that opposes current flow due to the motor coils moving relative to the magnetic field [72]. The back electromotive force can be estimated as $e_{bemf} = k_v \dot{\theta}_m$, with $k_v \in \mathbb{R}_+$ representing the motor speed constant and $\dot{\theta}_m \in \mathbb{R}$ as the angular velocity of the motor at the motor shaft before gearbox transmission to the load shaft. Similarly, $\tau_m \in \mathbb{R}_+$ is the torque applied on the motor shaft. $k_t \in \mathbb{R}_+$ is the motor torque constant, $J \in \mathbb{R}_+$ represents the motor's moment of inertia (kg · m^2), and $\nu_m \in \mathbb{R}_+$ represents the motor's viscous damping coefficient, estimated as:

$$\nu_m = \frac{k_t \cdot I_{nl}}{\dot{\theta}_{nl}}. \tag{5-6}$$

This ensures that in no-load conditions, a current equal to the no-load current I_{nl} is consumed when the motor is rotating at the no-load speed $\dot{\theta}_{nl}$.

As we are interested in operation under steady-state conditions, we can assume a constant velocity, meaning that we can neglect the losses due to moment of inertia J. Also, we assume a constant torque in our steady-state condition, meaning that our current will be stable, and thus the voltage loss due to terminal inductance $L\frac{dI_m}{dt}$ in the voltage equation can be neglected. Together, we obtain the steady-state motor model:

$$\begin{aligned} U_m &= R_m I_m + e_{bemf} = R_m I_m + k_v \dot{\theta}_m \\ I_m &= \frac{1}{k_t}(\nu_m \dot{\theta}_m + \tau_m) = \frac{I_{nl}}{\dot{\theta}_{nl}}\dot{\theta}_m + \frac{\tau_m}{k_t}. \end{aligned} \tag{5-7}$$

Gear ratio relationship: The motor torque and speed are functions of the gear ratio, expressed as:

$$\dot{\theta}_m = n\dot{\theta}_l. \tag{5-8}$$

Similarly, the motor torque can be estimated as:

$$\tau_m = \frac{\tau_l}{n\eta_\tau}, \tag{5-9}$$

with $\tau_l \in \mathbb{R}_+$ as the output torque at the loaded rod and $\eta_\tau \in [0,1] \subset \mathbb{R}$ as the gearbox efficiency.

Relating motor current to decision variables: To compute the MOPs, we need to relate the individual optimization function to the decision variables, constants, or other objective functions, which is currently not the case for the motor current draw I_m. For I_m we substitute the motor speed $\dot{\theta}_m$ out of the motor current equation in Equation (5-7). For that, we first rewrite the equation for $\dot{\theta}_m$ in terms of the variables in the motor voltage equation:

$$\dot{\theta}_m = \frac{U_m - R_m I_m}{k_v}. \tag{5-10}$$

We substitute this expression for $\dot{\theta}_m$ into the motor current equation to isolate I_m:

$$I_m = \frac{I_{nl}}{\dot{\theta}_{nl}}\left(\frac{U_m - R_m I_m}{k_v}\right) + \frac{\tau_l}{nk_t\eta_\tau}, \tag{5-11}$$

This allows us I_m to relate only to the decision variables (U_m, n) and constants ($\dot{\theta}_{nl}$,I_{nl}, k_v, k_t, η_τ, τ_l), where τ_l will be equal to the torque applied by the environment:

$$I_m = \frac{1}{k_v\dot{\theta}_{nl} + I_{nl}R_m}(I_{nl}U_m + \frac{\tau_l}{nk_t\eta_\tau}k_v\dot{\theta}_{nl}). \tag{5-12}$$

5-1-3 Deriving the Individual Optimization Problems

From the model above, we can now derive the objective functions f_i and constraints g_j and h_k.

Minimizing the energy consumption for reorientation from the battery As most of the energy consumption is during reorientation we will set it through:

$$\min f_1(x_1, x_2) = \min E_b(n, U_m), \tag{5-13}$$

where

$$\begin{aligned} E_b(n, U_m) &= \eta_{dcdc}(U_m) t_{re}(n, U_m) U_m I_m(n, U_m) \\ t_{re}(n, U_m) &= \frac{s_l(n)}{\dot{\theta}_l(n, U_m) s_p} \\ \dot{\theta}_l(n, U_m) &= \frac{U_m - R_m I_m(n, U_m)}{k_v n} \\ I_m(n, U_m) &= \frac{1}{k_v \dot{\theta}_{nl} + I_{nl} R_m} (I_{nl} U_m + \frac{\tau_l}{n \eta_\tau k_t} k_v \dot{\theta}_{nl}). \end{aligned} \tag{5-14}$$

Minimizing the current draw peaks to minimize the battery attenuation For the estimation of the current peak, we cannot use the simplified steady-state equivalent circuit model of the DC geared motor. This is because peak current generally occurs at the initialization of the motor when the current heavily varies, meaning that we cannot ignore the terminal inductance $L\frac{dI_m}{dt}$ without significantly impacting the estimation accuracy. Instead, we estimate the current draw peaks through the full voltage equation, from Equation (5-5):

$$I_{peak} = \max \frac{1}{R}(U_m(t) - e_{bmf}(t) - L\frac{dI_m(t)}{dt}), \tag{5-15}$$

showing that our inrush current is a factor of all three decision variables n, U_m, and t_{ramp}. making our optimization function:

$$\min f_2(x_1, x_2, x_3) = \min I_{peak}(n, U_m, t_{ramp}). \tag{5-16}$$

Overcoming the minimal torque: The model above shows us that τ_l depends on both the motor driving voltage and the gear ratio. For the actuator to operate we need to ensure that the motor voltage and gear ratio are chosen such that it can overcome the torque applied by the mechanism, specified as τ_{min}:

$$\tau_l(n, U_m) =\geqslant \tau_{min}. \tag{5-17}$$

Since this τ_{min} is a requirement, we will not optimize it directly but instead enforce it as a constraint:

$$g_1(x_1, x_2) = \tau_{min} - \tau_l(n, U_m) \leqslant 0. \tag{5-18}$$

where $\tau_l(n, U_m) = \tau_m(U_m) n \eta_\tau$.

Minimizing the reorientation duration For the reorientation duration, we need to ensure that it is within acceptable limits for urgent care therapy. For the treatment of organophosphate poisoning, we set a maximum response time of 10 minutes. Assuming direct detection, no stomach motility, and no failed reorientation this would mean that it should take a maximum of 5 minutes for reorientation, as the device has to both fold in and fold out. To ensure this 5-minute limit, we will set enforce it as a constraint:

$$t_{re}(n, U_m) \leqslant 300, \tag{5-19}$$

which we in terms of the MOP can reformulate to:

$$g_2(x_1, x_2) = t_{re}(n, U_m) - 300 \leqslant 0. \tag{5-20}$$

Additionally, we aim to minimize the reorientation duration beyond 5 minutes to account for potential delays and faults, such as delay in detection, waiting for stomach motility, and failed reorientation. We represent this minimization as:

$$\min f_3(x_1, x_2) = \min t_{re}(n, U_m). \tag{5-21}$$

Note that, in reality, the folding in from retention will not require movement full translation over the bolt thread. As accounting for this would reduce the estimated reorientation duration, it would mean that $t_{re}(n, U_m) \leqslant 300$. still holds. However, as we currently do not have an exact figure on the nut location for reorientation, we chose to use the full reorientation for safe simplification. Also, the start of the actuation will have a delay close to the voltage ramp-up duration t_{ramp}. But as this delay is expected to be less than a single second, we deemed it negligible in light of a 300 seconds requirement.

5-1-4 Formulating and Addressing the Multi-objective Optimization Problem

Now we consolidate the above described objective functions f_1, f_2, f_3 and constraints g_1, g_2 into the MOP equation of Equation (5-1):

$$\begin{aligned} \min \quad & \mathbf{F}(n, U_m, t_{ramp}) = (E_b(n, U_m), I_{peak}(n, U_m, t_{ramp}), t_{re}(n, U_m)) \\ \text{subject to} \quad & g_1(n, U_m) = \tau_{min} - \tau_l(n, U_m) \leqslant 0 \\ & g_2(n, U_m) = t_{re}(n, U_m) - 300 \leqslant 0 \\ & n \in \{5, 26, 136, 700\}, \quad U_m \in [0.8, 5.5] \subset \mathbb{R}, \quad t_{ramp} \in \mathbb{R}_+. \end{aligned} \tag{5-22}$$

To tackle this MOP we propose a hierarchical approach, which consists of the following steps:

1. We first ensure that the torque and speed constraints g_1 and g_2 are satisfied. These constraints are required for the actuator system to function properly and provide the required performance in urgent care therapy for our organophosphate and gamma radiation antidote applications. We will look into these constraints Section 5-2.
2. Next, we prioritize minimizing the energy consumption for reorientation from the battery, E_b in Section 5-3. Here we select the optimal n and U_m values which adhere to the constraints of step 1.
3. Following that, we prioritize minimizing the current draw peaks, I_{peak}. This step enables us to determine the optimal t_{ramp} value in Section 5-4.
4. Finally, if no specific n and U_m were yet found we further we will further narrow down by minimizing the reorientation duration, t_{re}. This step ensures that the actuator system operates within acceptable time limits, accounting for potential delays and faults in the treatment process. We will reflect on this in the results of the section Section 5-6.

5-2 Mechanical Characterization: Torque and Reorientation Analysis

In this section, we will examine the mechanical coupling within our system, as presented in Figure 5-4. Specifically, we will focus on addressing the constraints of our MOP. We will begin by concentrating on the torque constraint:

$$g_1(n, U_m) = \tau_{min} - \tau_l(n, U_m) \leqslant 0$$

as detailed in Section 5-2-1. Subsequently, we will consider the orientation duration constraint:

$$g_2 = t_{re}(n, U_m) - 300 \leqslant 0$$

as described in Section 5-2-2. For the reorientation duration, we will first focus on deriving $\dot{\theta} l$, before analyzing the complete rre equation.

First, we will investigate the mechanical coupling within our system presented in Figure 5-4. In this section, we will focus on solving the constraint of our MOP. First, we focus on the torque constraint

$$g_1(n, U_m) = \tau_{min} - \tau_l(n, U_m) \leqslant 0$$

in Section 5-2-1. Afterwards, we move to the orientation duration constraint of

$$g_2 = t_{re}(n, U_m) - 300 \leqslant 0$$

in Section 5-2-2. For the orientation duration we first focus on deriving $\dot{\theta}_l$, before we analyze the full r_{re} equation

In each optimization step, we must first determine the unknown values that are not provided on the manufacturer's datasheet.

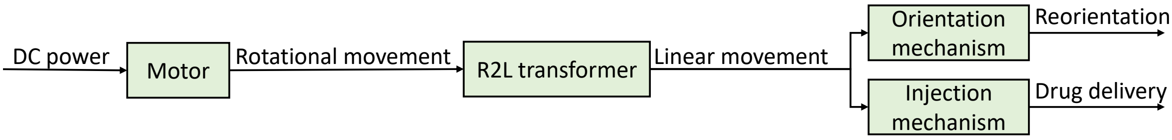

Figure 5-4: Overview of the mechanical coupling within the actuator system.

5-2-1 Overcoming Static and Dynamic Friction

Ideally, the torque constraint would be solved by deriving the values for τ_{min} and η_τ. However, due to the unavailability of suitable measuring tools in the lab, we were unable to capture these torque-related parameters. Consequently, we adopted an alternative approach, experimentally deriving voltage and gear ratios where the motor jams, essentially reformulating the constraint equation to:

$$g_1(n, U_m) = \frac{\tau_{min}}{\eta_\tau} - \tau_m(U_m)n \leqslant 0. \tag{5-23}$$

We assessed the likelihood of motor jamming at both initialization and during movement through 10 tests for the bolt and nut coupling only, as we only had a prototype with the leg system for the 700GR motor. The motor was tested at driving voltages ranging from 0.8V to 5.5V with increments of 0.1V, and gear ratios of 5, 26, 136, and 700. Separate tests were conducted for initialization and during movement since the torque required to overcome static friction during standstill is higher than the dynamic friction.

Our test results revealed that the likelihood of getting stuck decreases with higher voltages and gear ratios, and is lower during movement. Specifically, we found that:

- The 5 gear ratios were unable to overcome the torque applied in all cases, thereby reducing our options for the gear ratio to $n = 136, 700$.
- With a gear ratio of 136, the minimum voltage to consistently overcome static friction is at 1.3V, and 1.1V for dynamic friction.
- With a gear ratio of 700, the motor did not jam at any voltage in the input voltage range.

5-2-2 Adhering to the Time Duration Constraint

In this section, we focus on the time duration constraint $g_2 = t_{re}(n, U_m) - 300 \leqslant 0$, where $t_{re}(n, U_m) = \frac{s_l(n)}{\dot{\theta}l(n,Um)s_p}$. To derive this constraint, we ideally derive the individual parameters of the speed equation $\dot{\theta}l(n, Um) = \frac{U_m}{k_v n} - \frac{R_m I_m(n,U_m)}{k_v n}$. However, we did not have the necessary tools to measure R_m and k_v of the motor system individually in the lab. Therefore, we directly derived the parameters between the motor driving voltage and speed relationship empirically through experimentation.

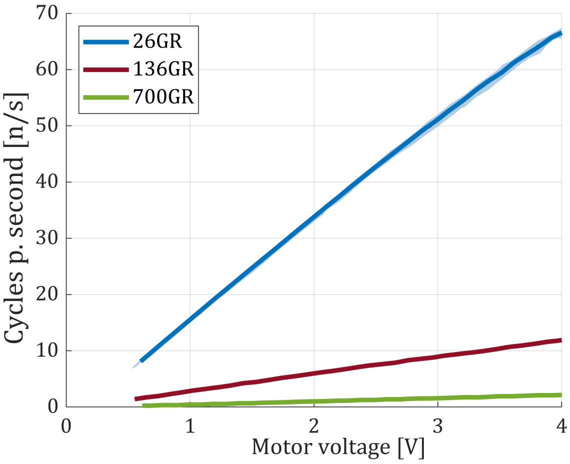

Figure 5-5: Measured motor speed for different gear ratios and voltages (n=10).

We conducted experiments with the gear ratios 26, 136, and 700, and measured the corresponding cycle speeds of the motor at different driving voltages when free of load. We performed 10 tests at increments of 0.1V. The results of these experiments are presented in Figure 5-5. The graph demonstrates a linear relationship between motor speed and driving voltage, with negligible deviation. Fitting a line on each curve, we obtain the relationship shown in Table 5-1.

Table 5-1: Approximate relationship between motor voltage U_m [V] and motor speed at the load $\dot{\theta}_l$ for different gear ratios.

Gear ratio	$\dot{\theta}_l[cycle/s]$
26	$16.5U_m$
136	$3U_m$
700	$0.55U_m$

With $\dot{\theta}l$ derived, we can analyze the relationship between motor movement and the resulting translation of the bolt and nut coupling. We also already chose $s_p = 1$, so we only need to find s_l. We know that $s_l(n)$ is determined by the length of the DC geared motor. The nut itself has a thickness of 4mm, which means that $s_l = \text{Length motor} - 4$. Putting all of the above together we can estimate the t_{re} for each gear ratio as shown in Table 5-2. Herein the slowest reorientation, which occurs at 0.8V for the 700 GR motor, takes approximately 40 seconds. This allows for multiple reorientations in case of failure. In conclusion, the time constraint is satisfied for all tested gear ratios and motor voltages.

Table 5-2: Length per gear ratio of Sub-Micro Plastic Planetary Gearmotors by Polulu [58].

Gear ratio	Motor length [mm]	s_l	t_{re}
26	16.0	12.0	$0.73 / U_m$
136	19.0	15.0	$5.0 / U_m$
700	21.0	17.0	$31 / U_m$

5-3 Electrical Characterization: Energy Optimization

In the preceding section, we investigated the relationship between voltage, speed, and torque in the actuator system. In this section, we focus on the delivery of the desired motor voltage from the battery by examining the electrical circuit of our actuator system, as shown in Figure 5-6. Our primary objective is to derive an energy optimization problem:

$$f_1(x_1, x_2) = \min E_b(n, U_m).$$

We begin by analyzing the energy consumption at the motor side $E_m = t_{re}(n, U_m)U_m I_m(n, U_m)$ in Section 5-3-1. Subsequently, we investigate the DC-DC conversion efficiency η_{dcdc} in Section 5-3-2. Putting these together, Section 5-3-3 proposes where we actively change the motor voltage according to the battery voltage

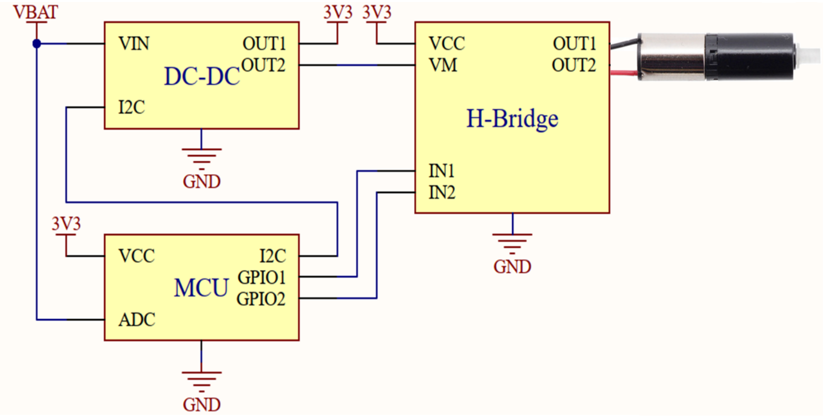

Figure 5-6: Electric circuit diagram of the actuator system.

5-3-1 Analyzing the Motor Energy Consumption

We express the motor current as $I_m(n, U_m) = \frac{1}{k_v\dot{\theta}nl + InlR_m}(I_{nl}U_m + \frac{\tau_l}{n\eta_\tau k_t}k_v\dot{\theta}nl)$. However, we encounter the issue that we cannot measure values related to torque, such as $\eta\tau$ and τ_l. Therefore, we empirically derive the current draw at various voltages in the absence of any load. As illustrated in Figure 5-7, the relationship between the motor's current draw and input voltage is nonlinear, contrasting with the linear relationship between voltage and speed. This can be attributed to internal losses, such as those resulting from friction within the motor. We observe that the most energy-efficient voltage, when the motor is free of load, is the lowest voltage. Additionally, smaller gear ratios are generally more efficient in terms of energy consumption.

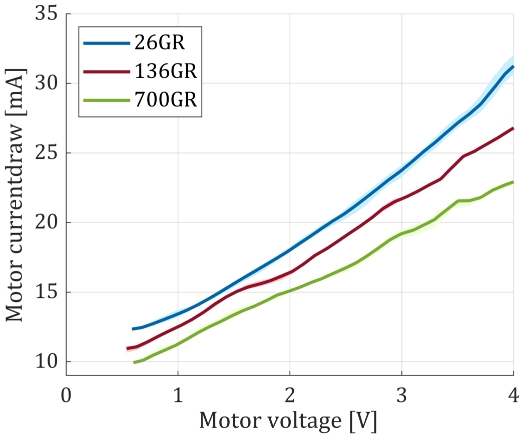

Figure 5-7: Motor current draw for different input voltages load (n=10).

5-3-2 DC-DC Converter

Next, we examine the conversion efficiency of the DC-DC converter, denoted as η_{dcdc}. Recalling Section 3-3-4-6, the conversion efficiency is influenced by the current draw, input voltage, and output voltage. In our context, the input voltage is supplied by the battery, while the output voltage drives the motor.

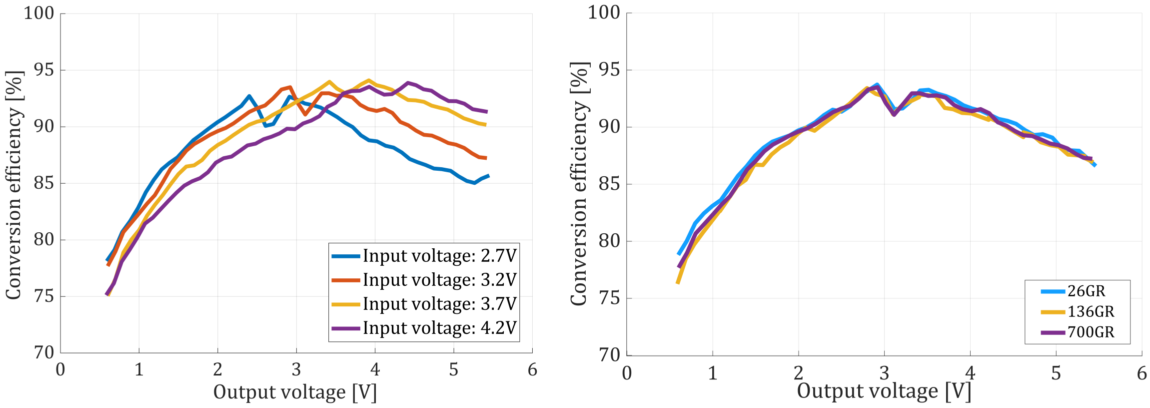

Figure 5-8: DC-DC conversion efficiency over output voltage, **(left)** for different input voltages with a 136:1 gear ratio motor and **(right)** for different gear ratios with a 3.2V input voltage (n=10).

As depicted in Figure 5-8, we empirically determined the relationship between input and output voltage for the conversion efficiency. Furthermore, we gauged the relationship between the gear ratio and output voltage to understand the effects of the current draw. The results indicated that the disparity between the input and output voltage of the DC-DC converter has a significant impact on its conversion efficiency. However, no notable differences in conversion efficiency were observed across different gear ratios.

A closer examination of the conversion efficiency measurements reveals that the DC-DC converter is most efficient when the difference between input and output voltages is minimal, barring a slight dip just below the input voltage. We could not verify what caused this dip. The efficiency losses tend to increase dramatically as the gap between input and output voltage widens. Considering the energy consumption of the motor before voltage conversion, a lower motor driving voltage would seem more energy-efficient. However, the above results suggest that this may not hold true when accounting for energy consumption from the battery, given the conversion efficiency losses.

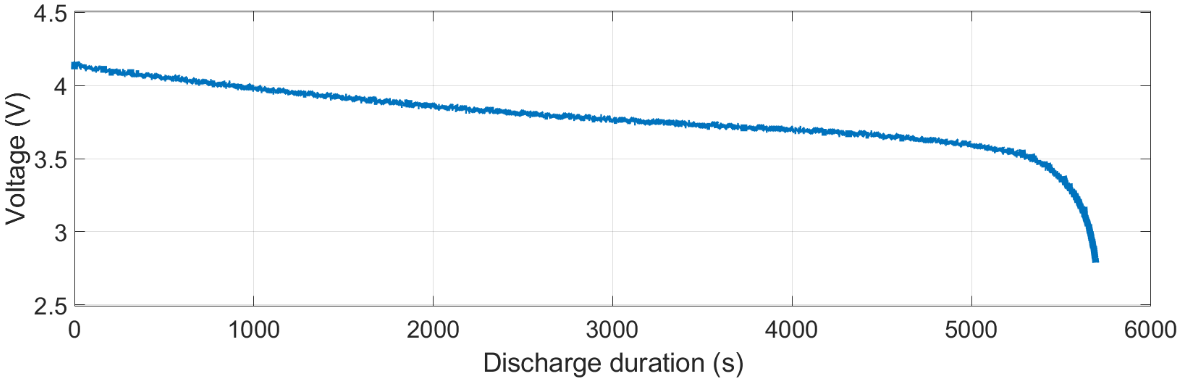

Figure 5-9: Discharge profile of a 3.7V Lithium-ion battery (CG-320A by Panasonic).

Moreover, as batteries deplete, they exhibit a decline in discharge voltage, as demonstrated in Figure 5-9 for our CG-420A/M3 lithium-ion battery. This change implies that the DC-DC converter input voltage will vary over time. Therefore, determining the optimal motor driving voltage also requires considering battery discharge characteristics. To this end, we need to formulate a model that integrates our findings from the motor efficiency curve and the DC-DC conversion efficiency curve for diverse input voltages.

5-3-3 Energy Optimization Algorithm

Traditional DC geared motor models primarily focus on the actuator's energy consumption without accounting for the voltage conversion efficiency losses [71]. However, as highlighted in the preceding section, these losses can be significant. We showed that the conversion efficiency of the DC-DC converter varies with the battery voltage, underscoring the need for a model that adjusts the motor voltage based on the battery voltage.

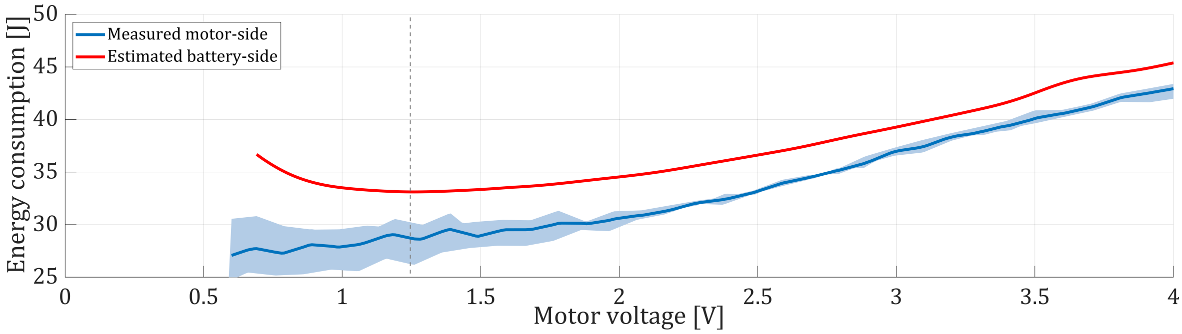

Figure 5-10: Energy consumption for a 700 gear ratio motor and 3.2V battery discharge voltage.

Figure 5-10 presents the energy consumption of a 700gear ratio (GR) motor under a battery input voltage of 3.2V. Upon incorporating conversion efficiency, we identify a different driving voltage for optimal energy efficiency. While the motor estimation suggested the minimal operable driving voltage as the most energy-efficient, the full circuit model indicates that efficiency decreases below 1.3V.

Table 5-3: Optimal motor driving voltages $U_{m.opt}$ for different DC-DC input voltages U_{in}

Gear ratio	**$U_{m.opt}$ at $U_{in} = 3.2$**	**$U_{m.uot}$ at $U_{in} = 4.2$**	Energy p. rotation [J]
26	0.9	0.95	1.2
136	1.1	1.1	5
700	1.25	1.3	34

In Table 5-3 we summarize the optimal operating voltages found for the 26GR, 136GR, and 700GR motor for different DC-DC converter input voltages. From this table, we can conclude that a 1V change in input voltage results in a maximum shift of 0.05V in the optimal motor driving voltage. Looking at Figure 5-10 near the optimum a difference of 0.05 would have no significant impact on the energy consumption per cycle. Considering that our battery system will operate in a range between 5.5V and 6V, we deem the impact of battery attenuation not worth the computational effort to estimate actively during operation. Instead, we will select a constant optimal driving voltage for a DC-DC input voltage of 5.75V.

5-4 Mitigating Inrush Current

In this section we focus on our third optimization function

$$\min f_3(x_1, x_2) = \min t_{re}(n, U_m)$$

Before we can optimize towards this we need to determine if DC-DC converter and H-bridge can provide the voltage resolution to allow for regulation over the ramp up duration. To ensure precise control of the motor, it is crucial to accurately determine the input voltage without significant delay.

5-4-1 Control Resolution of the DC-DC Converter and H-Bridge

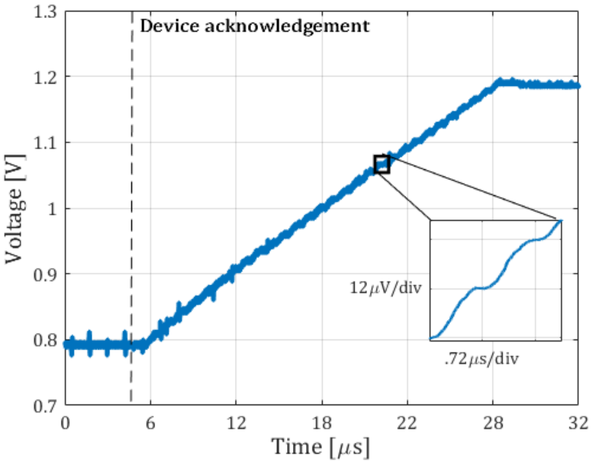

Figure 5-11: Resolution of the voltage step and time step of the DC-DC converter

By measuring the resolution of the voltage step and time step of the DC-DC converter output, we can assess this accuracy and the associated delay. Figure 5-11 indicates that the DC-DC converter has a 12 microvolt precision, and that the delay can be estimated using a linear model with a slope of 100/6, where the delay in microseconds is denoted by y and the desired voltage change in microvolts is denoted by x.

For voltages under the minimum threshold of the DC-DC converter (0.8V). we utilize the H-bridge. The H-bridge offers a control delay of as little as 60 microseconds. This level of precision is more than sufficient for our needs, as our system only requires accuracy to within a tenth of a second. By implementing this configuration, we can ensure that our motor operates with a high degree of precision over the input voltage start and stop. Knowing that both our DC-DC converter as H-bridge can provide the necessary voltage and time resolution, we can now look into how we utilize these to minimize the current peak

5-4-2 A Soft Start Approach to Inrush Current Mitigation

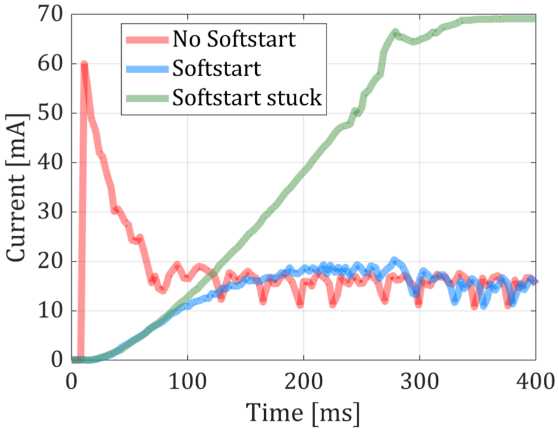

Figure 5-12: Current peaks depending on initialization for a 136GR motor under 2V.

Knowing that we control the motor at a high voltage and time resolution, we can now explore the effects of actuator inrush current. At initialization, DC motors are known to cause current peaks which can damage the battery, resulting in loss battery's energy capacity or overheating. damage. Coin-type silver oxide battery (SOB)s, such as our CR2450 Renata, are particularly vulnerable to this attenuation, as they prefer low discharge currents (< 1A).

A possible way to mitigate inrush current is through so-called soft start technique, which involves gradually ramping up the voltage to the desired level. However, this technique has its downsides. While inrush current can provide extra power to overcome static friction, it can also lead to energy loss that does not contribute to the mechanism's movement. Furthermore, settling time increases, causing a delay in motor movement. To ensure that the system can overcome static friction even when the desired voltage can only overcome dynamic friction, we propose always initializing the system to a voltage that can overcome static friction before lowering it to the desired voltage. Additionally, as shown in Figure 5-12, we observe that the inrush current can be entirely eliminated by employing a soft start duration of 200 milliseconds. For example in the case of 136GR motor operating under 2V this results in a negligible energy loss of only 0.2 mJ.

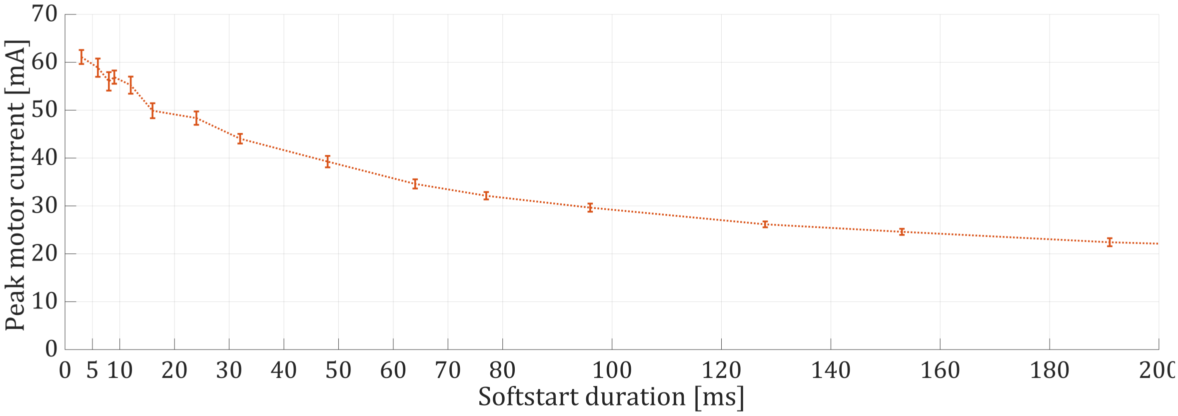

Figure 5-13: Relationship between current overshoot and rise time (to 95%) duration for a 136GR motor at 2V.

For our eventual soft start strategy, we incrementally elevate the voltage output in small, evenly spaced intervals of 5% over the soft start duration. For instance, for a 1V soft start over a period of 100ms, we break down this duration into 20 smaller intervals of 5ms each, increasing the voltage output by 0.05V at each interval. This method effectively mitigates the potentially damaging effects of inrush current. An alternate strategy commences with an initial leap to a higher voltage (e.g., 30-60% of the desired voltage), followed by an evenly spaced ramp-up period. The advantage of this approach is the provision for a shorter settling time and, as a result, reduced energy loss.

To identify the optimal soft start configuration for our system, we evaluated the inrush current for different soft start durations using increments of 0.05V. The outcomes, depicted in Figure 5-13, indicated that the majority of the inrush current mitigation is obtained before 100ms. We ultimately opted for an inrush current 10% above the steady-state current, which was achieved at 130ms.

5-5 Increasing Reliability for Actuator Jamming

During the characterization of our actuator system, we observed two risks in the reliability of the actuator system: actuator jamming and mechanism overshoot. In this section, we will propose methods to account for these two risks.

5-5-1 Actuator Safety Mechanisms

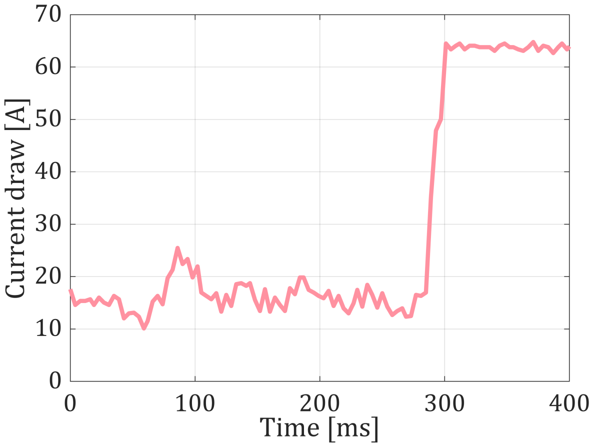

Figure 5-14: Motor current draw when getting stuck during movement.

The motor mechanism may get stuck during initialization or operation, leading to energy waste and high current draw. To address this issue, we propose the development of an algorithm capable of freeing the motor when it becomes stuck. Two types of detection mechanisms can be utilized for this purpose. One is based on measuring the alternating current (AC) components of the current draw to monitor the motor movement. When the motor gets stuck, the AC component strongly decreases, enabling us to detect the issue. The other approach is to set a threshold for the amplitude, as the current greatly increases when the motor is stuck. Both methods will require the integration of a current sensor, ideally with an update frequency in milliseconds scale to ensure early detection. A possible solution to this would be to replace our voltage sensor setup with a programmable current/voltage monitor, where we can momentarily switch to sensing current during motor operation. A good candidate for this would be the INA219 by Texas Instruments with a 500-kHz sampling rate.

We opt for the amplitude-based method due to several advantages. Firstly, it allows earlier detection of the issue, even before the value has settled. Furthermore, it is computationally less expensive, as we can directly read the current draw without the need for computation of the AC component. Therefore, the amplitude thresh hold method is more efficient and effective in addressing the issue of motor sticking, minimizing energy waste, and battery attenuation.

5-5-2 Minimizing Actuator Overshoot with Voltage Ramp Down

Overshoot in our actuator mechanism presents a significant risk, potentially leading to false triggering of the injector. This scenario could prove problematic if the device has not yet achieved the correct standing position during unfolding. The root cause of this overshoot is likely the buildup of momentum within the system.

To mitigate this issue, we propose a strategy involving a voltage ramp-down prior to a complete stop. This approach involves a three-step process: initially, the voltage is reduced to the minimum required to overcome static friction. Then, it is further decreased to the minimal level necessary to counteract dynamic friction. Finally, a complete stop is initiated using the H-bridge.

As illustrated in Figure 5-15, this technique enables a smooth and controlled stop for the actuator, effectively reducing the risk of overshoot. This method is particularly beneficial in scenarios where precise positioning is crucial, such as at the end of reorientation but prior to needle injection. Implementing this voltage ramp-down technique should enhance the reliability and accuracy of the device's operation, particularly during the critical stages of reorientation and injection.

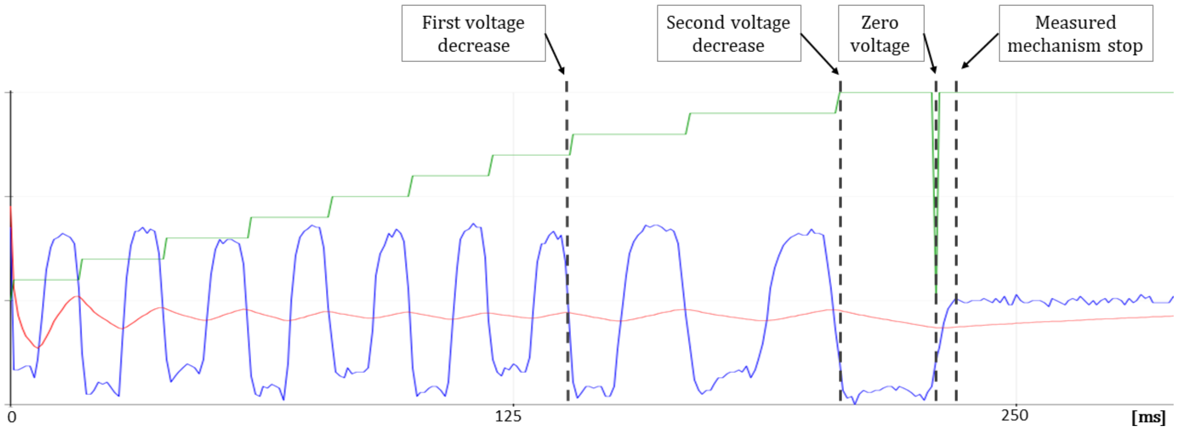

Figure 5-15: Example of the voltage ramp down for 136GR motor under a initial operating voltage of 2V.

5-6 Results and Findings

5-6-1 Final Actuator System Design

Now that we have investigated the principles behind each subobjectives of our MOP, we can finally state the Equation (5-24) and propose a final design setup:

$$\begin{aligned} \text{min} \quad & \mathbf{F}(n, U_m, t_{ramp}) = (E_b(n, U_m), I_{peak}(n, U_m, t_{ramp}), t_{re}(n, U_m)) \\ \text{subject to} \quad & g_1(n, U_m) = \tau_{min} - \tau_l(n, U_m) \leqslant 0 \\ & g_2(n, U_m) = t_{re}(n, U_m) - 300 \leqslant 0 \\ & n \in \{5, 26, 136, 700\}, \quad U_m \in [0.8, 5.5] \subset \mathbb{R}, \quad t_{ramp} \in \mathbb{R}_+. \end{aligned} \tag{5-24}$$

g_1 : In Section 5-2, we saw that only the 136GR and 700GR motor can overcome the mechanism torque. Next to that the 136GR requires an input voltage of at least 1.3V to ensure that it can always overcome the torque. The 700GR was able to overcome the torque under all available voltages.

g_2 : Additionally we saw that all gear ratios and input voltages were able to provide rotation within 5 minutes. The longest duration was 40 seconds with a 700GR motor at 0.8V.

f_1 : Section 5-3 provided us Table 5-3. From this, we can conclude that of the available 136GR and 700GR motors, the 136GR motor is preferred due to its lower energy consumption. Specifically at a driving voltage of 1.1V. Due to the constraint of g_1, we will instead opt for 1.3V driving voltage.

f_2 : In Section 5-4, we found an optimal soft start duration of 130ms.

f_3 : As we have already defined the motor gear ratio and motor driving voltage, we will not be able to further optimize towards reorientation duration.

5-6-1-1 Empirical Validation

At the time of this thesis, only a 700GR setup had been implemented, preventing us from testing our proposed setup with the 136GR motor. Thus, we proceeded with the available 700GR motor.

To evaluate energy consumption, we executed experiments to measure the motor's energy consumption in a test setup. The motor was tested at various voltages, ranging from 0.8V to 5.5V, in alignment with the capabilities of the adjustable DC-DC converter and the torque requirement.

Our analysis showed that the most energy-efficient voltage for the motor was 1.5V, with a consumption of merely 0.8Ws. When compared to the battery's energy capacity of 648Ws, each reorientation would consume a negligible 0.0013% of the battery's capacity.

The observed optimal voltage of $1.5V$ is higher than our theoretical optimum at $1.3V$. We surmise this discrepancy could be due to the increased torque exerted by the addition of the leg system. We anticipate a similar effect with the 136GR motor, but likely leading to even higher optimal voltages due to its lower torque conversion.

5-6-2 Results on Soft Start for Inrush Current Mitigation

We conducted experiments to investigate the advantages of using soft start compared to no soft start for actuating the 136GR motor under a 1.3V while free-of-load until the lithium-ion battery (LIB) was depleted. The soft start approach involves incorporating a small initial jump of 40% and a 130ms soft start duration. The results, presented in Figure 5-16, indicate that the use of soft start led to a 10% increase in the number of cycles before battery depletion. We anticipate that the advantage of using soft start will be more pronounced for the SOB due to its lower standard operating current. In this scenario, we can further enhance the soft start duration to 200ms to fully mitigate the inrush current.

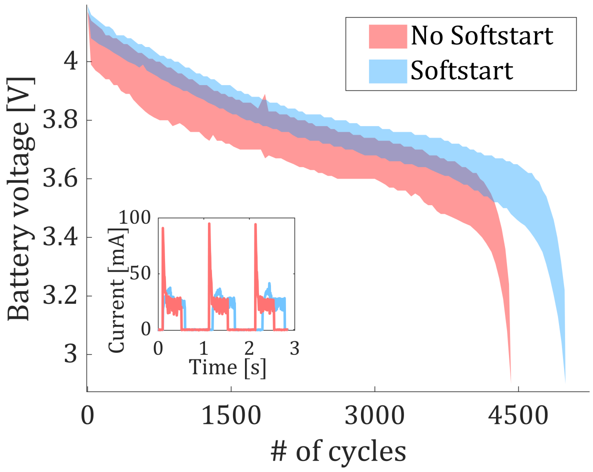

Figure 5-16: Battery attenuation, no soft start compared to soft start.

Chapter 6

Decision Making

In this chapter, we address the second research challenge presented in Section 2-2-1:

- *Develop a **decision making system** that ensures patient safety and increases injection reliability, while maximizing battery operation time.*

We start by breaking down the research challenge into two distinct decision making models in Section 6-1. From these models, we identify three key triggers that we investigate in Section 6-2. Armed with this context, we move forward to develop the decision making system in Section 6-3. Lastly, we address the limitations in evaluating the decision making system in Section 6-4 and discuss potential future work for its development.

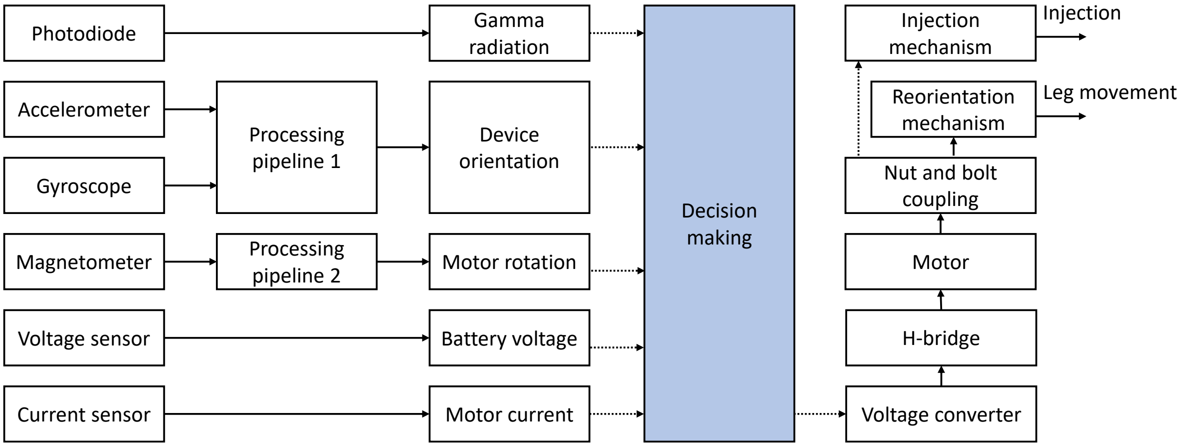

Figure 6-1: Component overview of the closed-loop reorientation and injection system, highlighting the focus of this chapter in color: the decision making system.

Research Contribution to the Decision Making System Development

This chapter details the development of a model that decides on sensor and actuator utilization. The author was solely responsible for the content of this chapter, with the exception of gamma radiation data collection for gamma radiation insights.

6-1 Introduction

We want to create our decision making system by developing it as a mathematical model of the ingestible robot. This model draws a physical or imaginary line that defines what is part of the system, and what is seen as external inputs or outputs. The model establishes relationships between these inputs and outputs, helping understand and control the system to achieve its objectives. During the development of the model, we aim to make it as simple as possible without compromising its reliability.

The inputs for our model come from the sensor system, which we covered in Chapter 4. The outputs include leg movement and injection, which we covered in Chapter 5, and the activation or deactivation of specific sensors. To address the research challenge using these inputs and outputs, we propose a two-layer decision making system:

- The first layer initiates processes such as terminating gastric retention upon battery depletion or component breakdown, activating a drug delivery procedure when detecting gamma radiation, and identifying the necessary sensing components to deactivate redundant elements and minimize energy consumption.
- The second layer involves the reorientation control, where we monitor the device orientation to decide on our motor use to increase injection reliability.

The rationale behind employing this two-layer decision making system lies in its ability to effectively separate the concerns between different states of the device. Before detecting gamma radiation, the device operates with a primary focus on energy preservation by determining sensor use. On the other hand the second layer instead it focuses on maximizing the chance for successful and timely gastric injection. Together these models should be able to realize the steps that we discussed in the initial device description in Section 3-1.

6-2 Insight into the Decision Making Triggers

Building upon the outlined decision making system, we now investigate how the sensor system data can be utilized for decision making. We first focus on preventing unwanted retention due to battery depletion in Section 6-2-1. Following this, we explore the initiation of the drug delivery procedure in response to gamma radiation detection in Section 6-2-2. Lastly, we examine fall detection as a means to verify successful reorientation in Section 6-2-3. Building on these insights, we will be able to develop our decision making model in the section hereafter.

6-2-1 Insights into Unwanted Retention Prevention

The battery voltage can accurately be tracked without significant noise disturbance. This allows us to implement a threshold-based detection system for low battery power. The battery discharge profile exhibits a nonlinear pattern, where the voltage remains relatively constant initially but declines steeply as the charge depletes, as depicted in Figure 6-2. To prevent unwanted stomach retention, we must select a voltage threshold that ensures that enough energy is left to retract the legs. Chapter 5 determined that full unfolding consumes less than 1% of the battery capacity. Based on this information, we opt for an initial threshold of 90% battery capacity, which should offer a safe margin considering other factors such as energy consumption from the MCU and the risk of actuator jamming. For our double battery setup, this translates to a bottom battery voltage threshold $V_{th} = 5$.

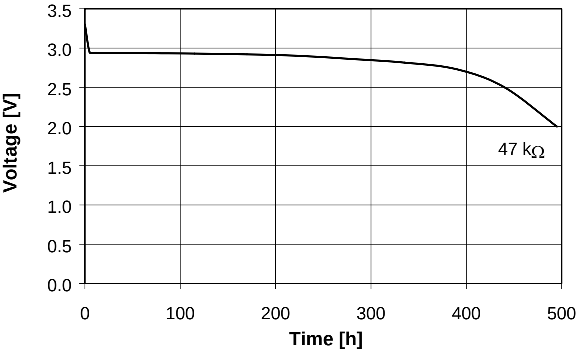

Figure 6-2: Discharge profile of the CR1025 Renata SOB battery from TI [59].

One potential concern regarding early end-of-charge detection is the voltage attenuation during the simultaneous operation of multiple electrical components. To assess this risk, we tested the voltage drop while using the most power-demanding components concurrently, including the inertial measurement unit (IMU), microcontroller unit (MCU), H-bridge, direct current to direct current (DC-DC) converter, and the direct current (DC)-geared motor, with the motor at 5V. In this scenario, we observed only a peak drop of 0.2V. As this drop is relatively small, leading to a worst-case scenario of a 5% earlier stop, we decided not to account for it.

On the other hand, we also have the chance of component breakdown caused by the harsh gastric environment, being acidity, and frequent stomach contractions. To ensure that the device does not remain in the stomach longer than components can handle, we can also set a threshold based on the duration of stomach retention. As a maximum retention duration $t_{c.th}$ we take the retention duration of Bellinger's retention system, that is 14 days or 1209600 seconds [25].

6-2-2 Insights into Gamma Radiation Detection

The gamma radiation sensor exhibits a distinct difference in output between the absence and presence of radiation. This clear distinction enables us to implement a simple threshold-based detection system. As observed in Figure 6-3, an initial gamma voltage threshold of $\gamma_{\text{th}} = 1V$ can be established as a suitable value for reliable detection in all cases.

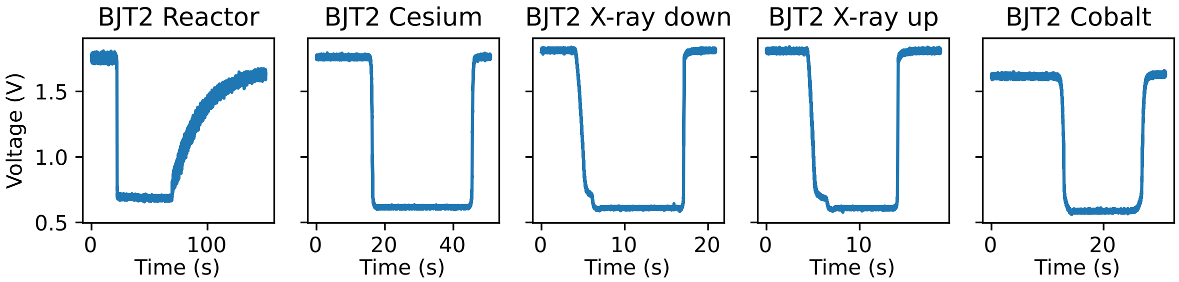

Figure 6-3: Gamma sensor output voltage for different gamma radiation sources. Captured by D. Werder and C. McLymore.

6-2-3 Insights into Fall Detection

To increase injection reliability, we developed a fall detection algorithm that monitors the movement of the ingestible device as it transitions from a lying to a standing position. The reasoning behind this algorithm is to ensure the safe and accurate reorientation of the device by detecting deviations from the expected trajectory.

The algorithm operates by continuously evaluating the orientation in terms of pitch and roll angles. These measurements are compared to the expected angles based on the progress of the reorientation. By identifying deviations from the expected orientation, the algorithm can detect if the device has toppled over. A key feature of our algorithm is the incorporation of a sliding window technique to analyze the orientation data. This approach reduces the impact of noise and fluctuations, ensuring a more accurate assessment of the reorientation. By selecting an appropriate window size, the algorithm can maintain sensitivity to sudden changes in orientation while dampening out spurious measurements.

Algorithm 6: Fall Detection Algorithm with Sliding Window

```
Input: $\mathbf{p}, \mathbf{r}, th, m, w$
Output: $y\_fall$
Initalize: $y\_fall \leftarrow$ False
$angle\_exp \leftarrow \frac{m}{M} \cdot 90$                      // Calculate expected orientation angle
$p\_win \leftarrow \mathbf{p}(\text{end} - w + 1 : \text{end})$              // Get the pitch window
$r\_win \leftarrow \mathbf{r}(\text{end} - w + 1 : \text{end})$              // Get the roll window
$p\_change \leftarrow |p\_win(\text{end}) - p\_win(1)|$       // Calculate change in pitch
$r\_change \leftarrow |r\_win(\text{end}) - r\_win(1)|$       // Calculate change in roll
$total\_change \leftarrow p\_change + r\_change$   // Calculate combined change in pitch and roll
$error\_angle \leftarrow |total\_change - angle\_exp|$    // Calculate combined error
if $error\_angle > th$ then
    $y\_fall \leftarrow$ True                               // Check if error exceeds threshold
end
return $y\_fall$
```

The algorithm takes in the current pitch $\mathbf{p}$ and roll angle data $\mathbf{r}$, combined pitch and roll thresholds th, the location of the nut according to the amount of full rotation m, and the window size w. The output is a Boolean value y_fall that indicates whether a reorientation has been detected. The algorithm also includes a constant that is the maximum number of nut rotations until reaching a standing position M, which should be determined according to the final design.

6-3 Developing the Decision Making Models

In the development of our decision making we first design the first layer in Section 6-3-1 based on the battery insight and gamma radiation insight. Afterwards, in Section 6-3-3 we focus on the second layer, focused on orientation control and based on the fall detection insight.

6-3-1 Introduction to Hybrid Automata

To model the sensor usage for gamma and low battery power detection we need to incorporate both discrete and continuous dynamics. The discrete element relates to the device's finite states, which are determined by crossing constant thresholds for gamma sensor readings or battery voltage updates. Simultaneously, based on the continuous element of time we decide when gamma or voltage sensor updates should occur. As the model transitions between a finite number of discrete states, the time value evolves continuously. Systems comprising both discrete and continuous components are termed hybrid systems. Hybrid systems are prevalent in embedded systems like ours, where computation occurs in discrete time while the environment changes continuously in time [73].

In our case, we handle a hybrid system where the continuous element tracks time to determine the sensor update time, and the transition between states is dictated by real-valued thresholds, such as gamma and voltage thresholds. These systems can be computed as timed automata, which involve simple continuous dynamics, such as $\dot{x} = 1$, and are suitable for encoding timing constraints. Alur and Dill [74] first introduced timed automata to model the behavior of real-time systems. A timed automaton is a finite automaton extended with a finite set of real-valued clock variables, and transitions are constrained by clock values. Time advances uniformly in all locations in this formalism, and transitions can be instantaneous or delayed depending on the guards controlling them. Transitions can also be labeled with actions, allowing synchronization of multiple timed automata to form more complex systems. Timed automata are used to describe hybrid systems where time serves as the continuous element, and transitions are governed by real-valued thresholds.

Formally timed automata are described through a sextuple $(L, \ell_0, \text{Act}, C, E, \text{lnv})$ where [74]

- L is the set of finitely many locations (or nodes);
- $\ell_0 \in L$ is the initial location;
- Act is the set of finitely many labeled actions;
- C is the set of finitely many real-valued clocks;
- $E \subseteq L \times \mathcal{B}(C) \times \text{ Act } \times 2^C \times L$ is the set of edges;
- Inv: $L \rightarrow \mathcal{B}(C)$ assigns invariants to locations. where $\mathcal{B}(C)$ denotes the set of clock constraints: $c \sim a$, $a \in \mathbb{Q}, \sim \in \{<, >, \leqslant, \geqslant\}$.

Furthermore, in our automaton, we want to associate individual states with an action, such as the deactivation of a sensor. A labeled timed automaton is a timed automaton where each transition is associated with a label representing an action or event. Labels are used to synchronize multiple timed automata, allowing them to communicate and coordinate their behavior.

6-3-2 Decision Making Model for Gamma Detection and Gastric Retention

Our decision-making system uses an automaton with three states: Low Power, High Power, and Exit. These states correspond to the activation of sensors and leg system positioning. The automaton transitions between states based on several conditions related to gamma radiation levels, voltage levels, and residency duration.

The automaton has the following working principles:

- It starts in the Low Power state, where the MCU is continuously powered and the gamma radiation and battery voltage sensor are activated at specified time intervals. During this position, the legs should already be positioned for gastric retention. The device remains in the Low Power state if all the specified conditions are met, such as the gamma radiation level, battery voltage level, and time constraints.
- If the gamma radiation condition is not met, it means that our device detects the presence of gamma radiation. At that point, the state will transition to the High Power state, where we continuously power the MCU, IMU, motor current sensor, and at time intervals the battery voltage. During this state, we move the motor according to the input provided from the second layer decision making system. The device will remain in this state until the battery voltage or the time constraint does not hold anymore.
- Once either the battery voltage or time constraint has passed a threshold value, the device will move to the Exit state. When entering this state the device will fully fold in the legs to exit the body and prevent unwanted retention due to an empty battery or mechanism decoration.

We can specify the values of the model as

- γ is the gamma radiation level measured by the sensor.
- γ_{th} is the gamma radiation threshold for transitioning between states.
- V is the measured voltage level.
- V_{th} is the voltage threshold for transitioning between states.
- t_1 is the time spent in the current state.
- $t_{\text{LP.th}}$ is the maximum time spent in Low Power state before updating V and t_c.
- $t_{\text{HP.th}}$ is the maximum time spent in High Power state before updating V and t_c.
- t_2 is the time since the last gamma radiation update.
- $t_{\gamma.th}$ is the maximum time interval between gamma radiation updates.
- t_c is the cumulative time spent in Low Power and High Power states.
- $t_{\text{c}.th}$ is the maximum allowed cumulative time spent in Low Power and High Power states.
- V_{in} is the initial voltage level.
- γ_{in} is the initial gamma radiation level.
- V_{upd} is the updated voltage level.
- γ_{upd} is the updated gamma radiation level.

According to Section 6-2 we can already set the $\gamma_{\text{th}} = 1$, $V_{\text{th}} = 5$, and $t_{\text{c}.th} = 1209600$. The other parameters require the testing of a prototype with an integrated printed circuit board (PCB). After its development, we can select proper values for the threshold constants and initial variables values.

Putting the above together we obtain the model:

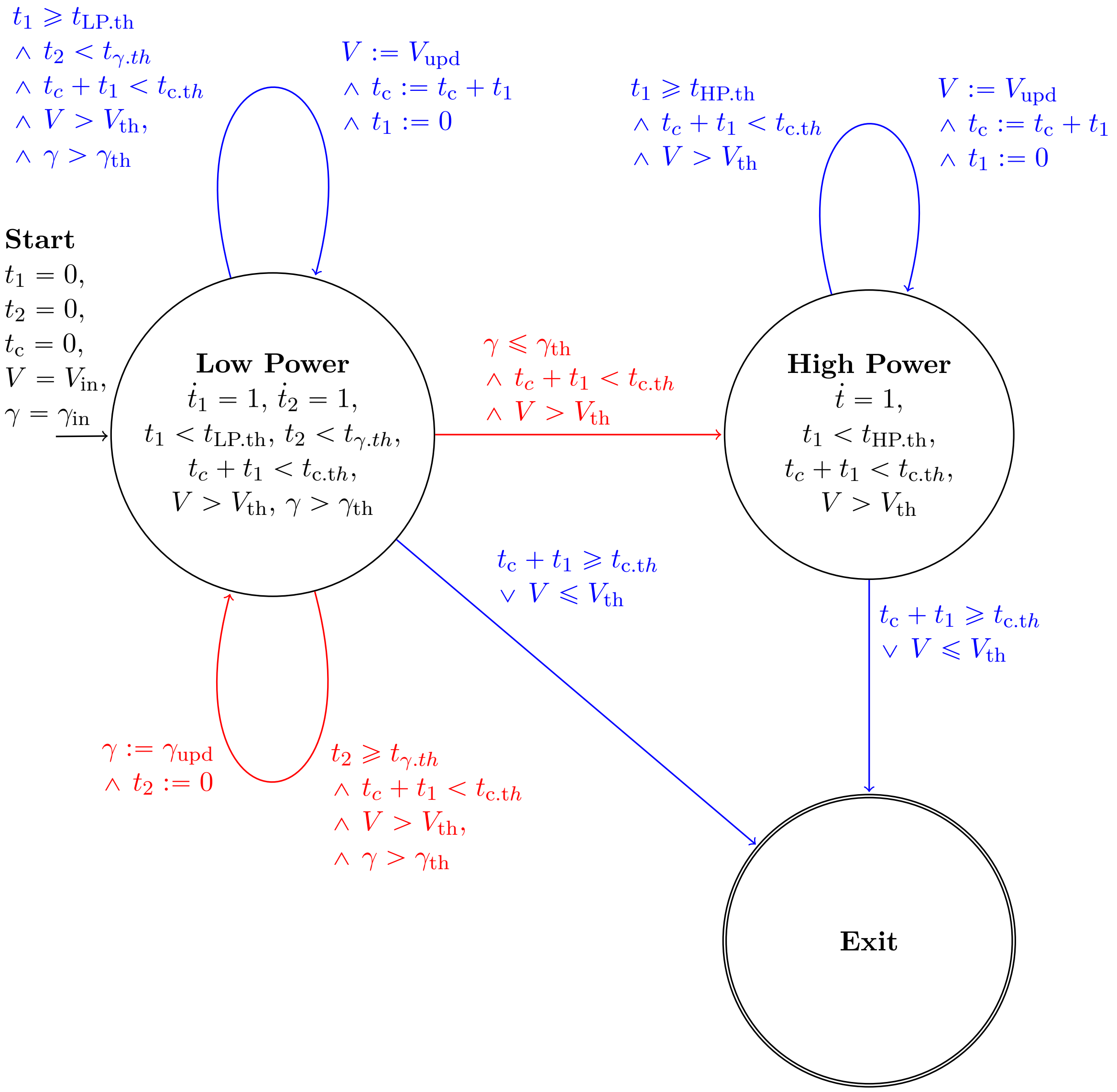

with in blue the steps related to halting retention, and in red the steps related to gamma detection. $\wedge$ denotes the logical 'and', which indicates that $X \wedge Y$ is true if logical predicates X **and** Y are **both** true. $\vee$ denoted the logical "or" which indicates that $X \vee Y$ is true if **either** logical predicates X **or** Y is true.

6-3-3 Decision Making Model for Orientation Control

Now we present the decision-making system for orientation control, which is activated when the device enters the High Power state from the primary decision making system. The orientation control automaton has the following working principles:

- The automaton starts at the beginning state when the device enters the High Power state of the primary decision-making system. In this state, the legs are positioned for gastric retention, the threshold angle difference for fall detection is set, and the time value is initialized to zero. The first action the system performs is folding in the legs by rotating the nut counter-clockwise at a constant speed. The system remains in this state until the legs have fully folded in.
- After the legs have folded in, the legs are unfolded again by rotating the nut clockwise at a constant speed. The device keeps on unfolding until a fall has been detected or the nut's estimated location for a standing position has been reached. If a fall has been detected the system returns back to the initial folding state to refold the legs. If we have been able to unfold to a standing position we move to the "check state" where we want to verify the orientation over a longer period of time.
- In the Check state, we pause the motor and measure the orientation at a more strict threshold over a larger time window. We do this to counteract problems with overshoot and to ensure that the motor is within a 10-degree angle for injection. If a fall has been detected with the stricter threshold we move back to the initial folding state to refold the legs. If no fall has been detected after a short wait we move on to injection.
- For the injection we continue to move the nut clockwise at a constant speed until it has reached the end of the bolt thread. Reaching the bolt thread means triggering the injection. After injection, we start the procedure of folding in by moving the motor counter-clockwise until the legs are at the angle for retention.

We define the following variables to model the system:

- m is the estimated location of the nut according to the number of rotations performed:
  - $m = 0$: The nut is at the start of the bolt thread with the legs fully folded in.
  - $m = m_{\text{max}}$: A constant that represents when the nut is at the end of the bolt thread, the legs are fully folded out, and the injection has been triggered.
  - $0 < m_{\text{ret}} < m_{\text{max}}$: A constant that represents when the legs are in the retention position.
  - $0 < m_{\text{ret}} < m_{\text{st}} < m_{\text{max}}$: A constant that represents when the legs are in the standing position, but the injection has not been triggered.
  - $\dot{m}_c$: A constant that gives the rotations per second of the nut, according to Section 5-6.
- F_{th}: The threshold angle difference for fall detection.
- F: A Boolean value expressed through binary values {0=No, 1=Yes} that indicates if a fall has been detected. We compute F using Algorithm 6.
- t: The time value.
- t_{th}: The time value threshold.

The decision-making process for orientation control is illustrated in the following diagram.

The system transitions between states based on the values of m, F, and t. The system is as follows:

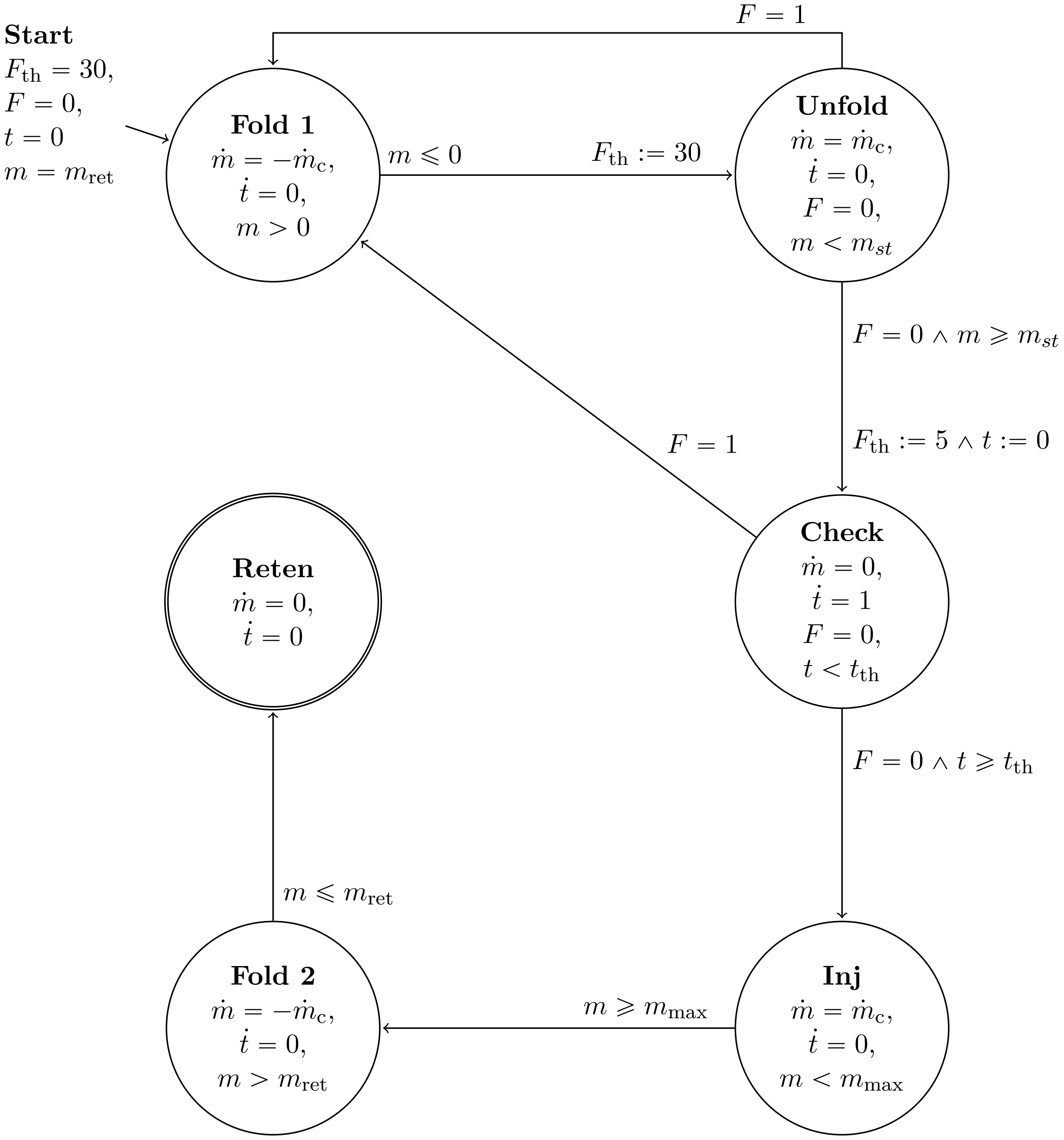

6-4 Limitations in Evaluating the Decision Making System

The gamma detection algorithm was tested through two trial runs with four distinct types of radiation sources. In all instances, our decision making system successfully identified the presence of radiation without generating any false positives.

In battery testing, our battery detection system was evaluated by continuously powering a 700GR motor until the voltage threshold. The test was performed 20 times with the use of the lithium-ion battery (LIB) with a voltage threshold of 3.7V. The same test was performed 2 times for a single coin cell with a voltage threshold of 2.7V. All cases were correctly detected without any false positives.

The evaluation of the reorientation system necessitates a fully functional prototype with control systems. Unfortunately, during the course of this thesis, such a prototype was not available for testing. Consequently, an assessment of the reorientation decision making model could not be carried out.

Chapter 7

Final System Description & Conclusion

In the design of the ingestible devices, we focused on three primary structures: a sensor system, an actuator system, and a decision making system. Chapter 4, Chapter 5, and Chapter 6 delved into each of these structures, elucidating their functions and presenting performance results. Based on these results, we can draw conclusions to assess the feasibility of the entire design by evaluating the design criteria initially established in the thesis statement found in Section 2-2. With all the results now available, we can outline the complete system design and determine the feasibility of the device as a whole.

7-1 Final System Description of the Autonomous Ingestible Urgent Care Therapy Device

In the final system, we consolidate all of the components discussed in Section 3-3 together into a single communication and power circuit as illustrated in Figure 7-1. The figure illustrates how the control system components can be powered with our silver oxide batteries. To host this communication platform on the ingestible device, a flexible printed circuit board (PCB) is shown in Figure 7-2, which can be housed within the leg system of the device. Here the inertial measurement unit (IMU) is strategically placed at the center of the PCB to simplify orientation computation. The PCB also has a battery extension that runs to the other side of the device to allow for powering.

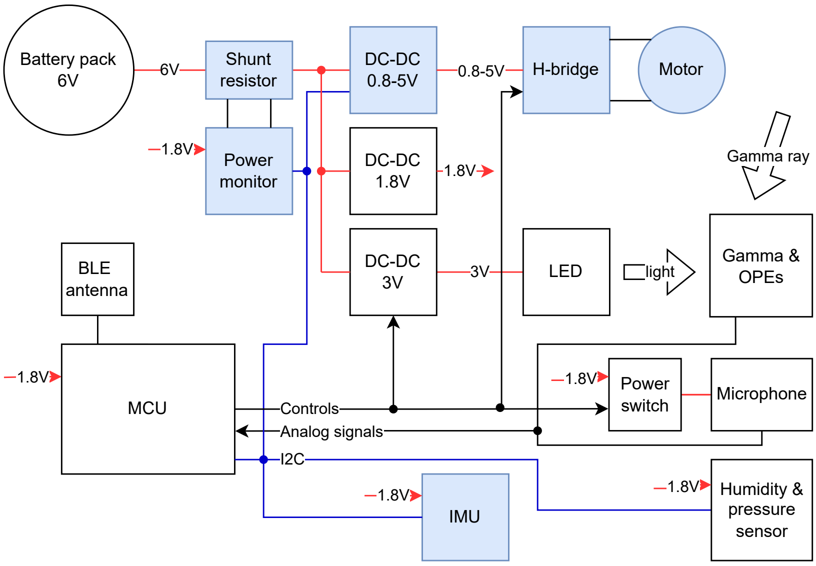

Figure 7-1: Block schematic of the PCB. Filled in blue are shown the parts that are used during reorientation. OPE is an organophosphate sensor. Designed by D. Werder.

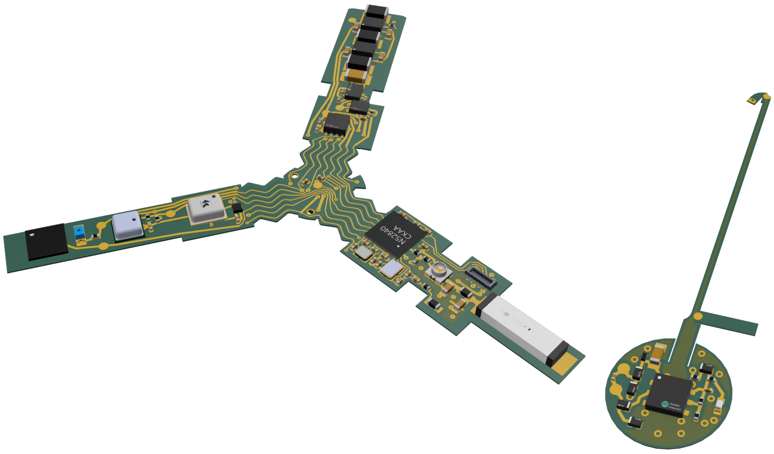

Figure 7-2: Illustration of the foldable PCB on the left with on the right the leg battery PCB. Designed by D. Werder.

7-2 Device Operation Time

Having described all components of the system in Section 3-3 and having estimated the actuator energy consumption in Section 5-6, we can now provide an estimation of the ingestible device's operation time.

Upon detailing all system components in Section 3-3 and estimating the actuator energy consumption in Section 5-6, we are now positioned to estimate the operational lifespan of the ingestible device. This involves a thorough evaluation of the power consumption for each component, distinguishing between two operating modes: low power (pre-gamma detection) and high power (post-gamma detection), as proposed in Chapter 6.

We initially estimate the energy expenditure during high power mode, which encompasses reorientation and drug delivery. Subsequently, the high power mode's energy consumption is subtracted from the total battery energy to calculate the remaining energy for the low power mode. We work on the assumption of fully utilizing the battery's energy capacity, set at $180mWh$.

The calculation of the total operational time transpires in two stages: firstly, we subtract the energy consumption for reorientation, which clarifies the remaining energy for the low power mode. Secondly, we divide the leftover battery energy by the hourly energy consumption in low power mode to ascertain the device's operational time. This calculation can be represented by the following equation, with the operational time expressed in days:

$$\text{OPERATION TIME} = \frac{\text{ENERGY CAP BATTERY} - \text{ENERGY CONS HP}}{\text{ENERGY CONS PER HOUR LP} \cdot 24}, \tag{7-1}$$

with CAP as capacity, CONS as consumption, HP as high power mode, and LP as low power mode.

Name	**Part Number**	**Power run mode**	**Run time**	**Power total**
DC-DC $0.5 - 5\ V$	MAX77533	$6\ mW$	$210s$	$0.350\ \mu Wh$
Power monitor	INA219	$540\ \mu W$	$210s$	$0.030\ \mu Wh$
MCU	NRF52840	$18\ mW$	$210s$	$1.105\ \mu Wh$
IMU	BMX180	$3\ mW$	$210s$	$0.175\ Wh$
H-bridge	DRV8210	$3\ mW$	$210s$	$0.175\ Wh$
Motor	Pololu 700GR	$40\ mW$	$210s$	$2.340\ Wh$
Total		$71\ mW$		$4.175\ mWh$

Table 7-1: Theoretical power consumption urgent therapy capsule in the lower power mode with runtime intervals of 20 seconds. Run and sleep powers are from the data sheets. H&P as humidity and pressure.

In the high power mode, we deploy the components highlighted in blue in Figure 7-1. In Table 7-1, we compile the energy consumption data of the high power mode components, which yields a total energy consumption of 71mW when operated continuously. According to the findings in Chapter 5, a single unfolding of the leg system lasts around 20 seconds. Given that we expect a total of five fold-ins and fold-outs, this results in 200 seconds of motor operation. Additionally, accounting for the initial unfolding for retention adds an extra 10 seconds to the total usage duration. Therefore, we anticipate a high power operation time of 210 seconds, leading to an estimated high power mode energy consumption of $4.175mWh$. This leaves $180 - 4.175 = 175.825$ mWh of battery capacity for the low power mode.

Name	**Part Number**	**Power run mode**	**Power sleep mode**	**Run time**	**Power total**
DC-DC 1.8 V	TPS62840DLCR	360 nW	360 nW	100 %	360 nW
DC-DC 3 V	TPS62840	360 nW	360 nW	0.5 %	360 nW
DC-DC $0.5 - 5$ V	MAX77533	6 mW	8 μW	0 %	8 μW
Power monitor	INA219	540 μW	3 μW	0.1 %	9 μW
MCU	NRF52840	18 mW	3 μW	1 %	210 μW
LED	CTL0603FPU1T	30 mW	0 W	0.5 %	150 μW
Gamma & OPEs	AFBR-S4N33C013	0 W	0 W	0.5 %	0 μW
Microphone	SPW2430HR5H-B	126 μW	180 nW	0.5 %	8 μW
H&P sensor.	BME280	3 mW	270 nW	0.5 %	15 μW
IMU	BMX180	3 mW	5 μW	0 %	5 μW
H-bridge	DRV8210	3 mW	148 nW	0 %	148 nW
Motor	Pololu 700GR	29 mW	0 W	0 %	0 W
Total	-	95 mW	29 μW		379 μW
Run time	-	1.9 *Hours*	256 *Days*		19.3 *Days*

Table 7-2: Theoretical power consumption urgent therapy capsule in the lower power mode with runtime intervals of 20 seconds. Run and sleep powers are from the data sheets. H&P as humidity and pressure.

In the low power mode, we foresee update intervals of 20 seconds for all sensors, with the exception of the power monitor, which will be activated every 2 minutes. We project that each update step will last for a full second. A potential downside of a larger update interval is the risk of delayed detection of the urgent care condition. However, even with a maximum delay of 20 seconds, we would still achieve injection within 5 minutes. Similarly to the high power mode estimation, we compile the energy consumption data of all components. In this case, however, we aim to determine the hourly energy consumption. As shown in Table 7-2, the energy consumption in the low power mode will be 0.379 mW.

By combining the above computations, we determine a total operation time of

$$\text{OPERATION TIME} = \frac{180 - 4.175}{0.379 * 24} = 19 \text{ days and 8 hours,} \tag{7-2}$$

which is beyond the wanted operation time of 14 days.

7-3 Feasibility of the Proposed Controllable Ingestible Systems for On-demand Stomach Retention and Injection

The objective of this thesis was to maximize the feasibility of the autonomous, ingestible device for urgent care therapy while ensuring a long device run time. We specifically focused on the development of the control system, which we broke down into the sensor system, decision making system, and actuator system. To evaluate the feasibility of the device, with regard to the development of the control system, we presented a list of goals in Section 2-2-2. In the coming section, we will look back at each of the research goals. To ease reading, we present the last again hereunder.

1. Assess the feasibility of the sensor-based decision making system:
   (a) Evaluate the accuracy of the onboard sensor system in monitoring needle angle, targeting an accuracy of 10 degrees or better;
   (b) Validate the decision making system's ability to guide injections, ensuring injections only occur within stomach tissue;
   (c) Validate the decision making system's ability to initiate drug delivery based on harmful agent detection without generating false positives or negatives.
   (d) Validate the decision making system's ability to prevent unwanted retention in the event of component failure;
2. Assess the feasibility of controllable gastric retention and injection:
   (a) Investigate the injection mechanism's capability to deliver medicine on-demand: within 24 hours for radiation poisoning treatment [3], and within 5 minutes for Anaphylaxis [42];
   (b) Address all safety concerns related to actuator failure;
3. Evaluate potential barriers to adoption concerning autonomy, long-term operation, and manufacturing:
   (a) Develop a control system powered by a battery deemed suitable by the United States Food and Drug Administration (FDA) for ingestible applications;
   (b) Optimize energy consumption to achieve a device run time of at least 14 days;
   (c) Ensure user-friendliness through a fully autonomous design that requires no human interaction post-ingestion;
   (d) Utilize common components for the control system to enable mass production.

7-3-1 Sensor and Decision Making System Feasibility

(a) Evaluate the accuracy of the onboard sensor system in monitoring needle angle, targeting an accuracy of 10 degrees or better. Reflecting on Chapter 4, we utilized cost-effective and low-power IMUs to achieve an orientation estimation. With a root-mean-square error (RMSE) of less than 2 degrees, the accuracy of our system is well within the desired 10-degree threshold, ensuring reliable detection of standing and falling positions.

(b) Validate the decision making system's ability to guide injections, ensuring injections only occur within stomach tissue. As mentioned in Chapter 6, the testing and validation of the decision making model's incorporation of orientation data for injection control have not been conducted during the course of this thesis. To thoroughly assess the fall detection algorithm and the effectiveness of our decision making model, a functional prototype with an integrated PCB is required. Unfortunately, such a prototype was not available for testing at the time of this thesis. Future work will need to address this limitation to ensure the device's reliability and safety in guiding injections within stomach tissue without generating false positives.

(c) Validate the decision making system's ability to initiate drug delivery based on harmful agent detection without generating false positives or negatives. Referring to Chapter 6, our initial tests demonstrated a distinct difference in gamma sensor readings before and after exposure to gamma radiation. In these preliminary tests, a threshold-based detection mechanism appeared to be sufficient without the need for data filtering. However, it is important to note that these tests were conducted under the influence of very strong radiation sources. In real-world scenarios, the distinction might not be as clear, or the radiation levels might be too high for sargramostim injection to prevent fatality effectively. To accurately evaluate the gamma detection system, further testing with lower dosages is necessary. Additionally, in-vivo testing should be conducted as a subsequent step to assess the detection rate for minimal dosages where sargramostim injection is considered beneficial.

(d) Validate the decision making system's ability to prevent unwanted retention in the event of component failure. Looking back at Chapter 6, we recognized two key scenarios that might result in undesired retention: unnoticed battery depletion and component failure. To tackle the risk of battery depletion, we introduced an algorithm designed to continuously monitor battery power levels. This threshold-based detection system proved consistently accurate in identifying low battery power instances, with no false positives recorded.

As for component failure, we can further distinguish the causes into gradual deterioration due to factors like stomach motility and stomach acid, and sudden breakdowns of components, for instance, motor malfunction or leg system failure due to unforeseen events. To counter gradual component deterioration, we implemented a time-based threshold. This mechanism enables the device to exit the stomach after a maximum set duration. The current maximum threshold is fixed at two weeks, but this should be adjusted based on a full device prototype in future work. We have yet to develop a safety system that can account for unforeseen incidents.

Once the prototype with an integrated PCB has been realized, the thresholds of the decision making system could be tailored toward the prototype. For the voltage system, this would be investigating the impact of battery attenuation. For the threshold timer, this would be investigating the rate of component deterioration in a stomach-like environment.

7-3-2 Controllable Gastric Retention and Injection Feasibility

(a) Investigate the injection mechanism's capability to deliver medicine on-demand: within 24 hours for radiation poisoning treatment [3], and within 5 minutes for anaphylaxis [42].

The ex-vivo trials conducted in Chapter 5 with a 700GR prototype revealed an approximate reorientation time of 20 seconds. Considering both the folding in and out processes, the total time required for reorientation amounts to 40 seconds. Given the gamma sensor's update interval of 20 seconds, this would result in a maximum total response time of 60 seconds prior to injection, provided that reorientation occurs correctly. In sum, the device can undergo a total of 8 trials before surpassing the 5-minute window critical for urgent conditions such as anaphylaxis. However, further tests are necessary to determine the success rate of reorientation, and subsequently, ascertain the feasibility of achieving the required response time.

(b) Address all safety concerns related to actuator failure. In Chapter 5, we identified three potential risks: actuator jamming, overshoot, and inaccuracies in motor position estimation. To counter actuator jamming, we implemented an algorithm that escalates the voltage upon detecting jamming, thereby enabling the device to overcome the static friction. To minimize actuator overshoot attributed to momentum, we devised an algorithm that ensures a gradual stop rather than an abrupt halt. While we were able to develop a motor tracking system to correct errors, we were unable to realize it within the existing prototype. This was predominantly due to challenges in magnet placement.

7-3-3 Feasability of the Overall System Concerning Ease of Use and Manufacturing

(a) Develop a control system powered by a battery deemed suitable by the FDA for ingestible applications. As detailed in Section 3-3-5, we selected silver oxide batteries as the most suitable option for our system, based on their use in FDA-approved ingestible devices. Our double-stacked 1025CR Renata silver oxide battery (SOB) setup provided the necessary voltage and current to power the system while complying with size constraints.

Figure 7-1 illustrates the use of two 3V coin batteries and multiple direct current to direct current (DC-DC) converters to supply power to our system components. Although we have mitigated inrush current through soft start-based actuation, concerns remain regarding the high constant current draw. The current 700GR motor's draw exceeds 10A at its lowest running voltage and reaches 15A at 2V, while the Renata prefers a maximum current draw of 1A. We were unable to test how the constant current draw relates to battery capacity attenuation.

(b) Optimize energy consumption to achieve a device run time of at least 14 days. Section 7-2 we estimated a device run time of 19 days and 8 hours, which is beyond the desired 14 days. In the energy consumption estimation, we assumed a total of 5 reorientations during high power mode, and a sensor update interval of 20 seconds during low power mode. In the estimation, we noticed that the operation time is mainly determined during the low power mode, with the microcontroller unit (MCU) and gamma sensor LED as main power consumers.

The primary limitation of the controllable retention and injection system is not the actuator system's energy consumption, but the reduced physical space, which significantly constrains available battery capacity. Additionally, the high current draw of the direct current (DC) motors may lead to rapid battery attenuation, potentially further diminishing battery capacity beyond energy consumption losses.

(c) Ensure user-friendliness through a fully autonomous design that requires no human interaction post-ingestion. We designed the system to require no additional steps beyond those of a regular pill, apart from initialization. The downside of this approach is that it does not allow for human calibration of the sensor system, which can be particularly important for the IMU sensors. In our studies, the sensor system met the orientation accuracy requirements, but this might not hold true when testing with different sensors that may have larger manufacturing errors or variability.

(d) Utilize common components for the control system to enable mass production. As described in Section 3-3, all components employed in this thesis were obtained from widely available vendors such as DigiKey or fabricated using 3D printing. These components include the sensors, the MCU, a DC geared motor, the reorientation mechanism, and the injection mechanism. By utilizing commonly available components, we pave the way for mass production, increasing the device's accessibility and scalability, and facilitating its widespread adoption in medical applications.

Chapter 8

Recommendations for Future Work

This thesis has successfully served as an exploratory study into the development and application of an autonomous retention and injection system for an ingestible urgent care therapy device. Alongside the assessment of its feasibility, an essential outcome of this research is the identification of recommendations for future work in this domain. This chapter aims to provide a concise overview of various research areas that warrant further investigation to enhance the performance and capabilities of the proposed device.

To facilitate a structured discussion, each of the subsections of this chapter will focus on distinct recommendations, categorized according to the primary topics of this thesis: sensing, actuation, and decision-making.

8-1 Recommendations for Future Research in Monitoring

8-1-1 Mitigating Risks of Unwanted Stomach Exit

One major concern related to our retention and injection mechanism is the potential for unwanted exit from the stomach, especially during the folding of the legs for reorientation. When the legs are folded in, the device becomes small enough to exit the stomach, which may lead to missed drug delivery or even the initiation of the injection procedure in other parts of the gastrointestinal (GI) tract. In the confined space of the intestinal area, the unfolding of the legs might not result in reorientation but could instead apply excessive force to the stomach wall and cause damage.

To address these risks, we propose three complementary strategies:

1. Detecting stomach exit to prevent harmful actuator movement
2. Designing an actuator safety mechanism
3. Preventing unwanted stomach exit

8-1-1-1 Detecting Stomach Exit

Detecting the stomach exit can be accomplished through various sensors, including those used for stomach localization. One approach involves tracking stomach exit using oxygen and pH sensing, as both values change significantly after leaving the stomach. However, this method may not guarantee safety, as the transitions in these values occur smoothly and could be detected too late [14]. Alternatively, the device could utilize heart rate and respiratory rate measurements captured by a microphone [16]. As the device exits the stomach, the distance to the heart and lungs increases, which may provide a clear distinction between the stomach area and other GI organs.

8-1-1-2 Designing an Actuator Safety Mechanism

To ensure patient safety, the actuator system should be designed to avoid applying excessive force. In Section 5-5, we developed a model to overcome motor stall torque. If a system can ensure the motor never stalls, this algorithm could be used to indicate when the legs are in a position where they should not unfold. As higher torque leads to higher current draw, this approach would help prevent the motor from exerting enough force to cause harm. However, this method has a drawback: the applicable torque might increase due to mechanism deterioration.

8-1-1-3 Minimizing Unwanted Stomach Exit

To mitigate the risk of unwanted stomach exit, the implementation of a stomach motility detection system using an accelerometer and gyroscope could be beneficial. This system would be designed to accurately identify sudden and forceful movements, such as shocks and vibrations, which could help reduce the likelihood of the device exiting the stomach unintentionally and prevent energy waste caused by the device toppling during the reorientation process. The use of an accelerometer and gyroscope would allow for seamless integration into the currently existing sensor system.

We propose the stomach motility detection pipeline illustrated in Figure 8-1. This pipeline filters accelerometer and gyroscope data and employs a peak detection algorithm to identify stomach motility events. A hybrid approach combining z-score peak detection and threshold-based peak detection algorithms is utilized in the peak detection process. The z-score peak detection algorithm is effective for identifying peaks under normal conditions, while the threshold-based approach acts as a safeguard, ensuring motility events are still detected if the z-score algorithm considers constant motility as the baseline. Motility is detected if either parameter surpasses the threshold.

Unfortunately, experimental validation of the motility performance was not feasible during the thesis due to the lack of in-vivo IMU data. Future work should focus on collecting relevant data and optimizing the filter and peak detection parameters to further refine the stomach motility detection system.

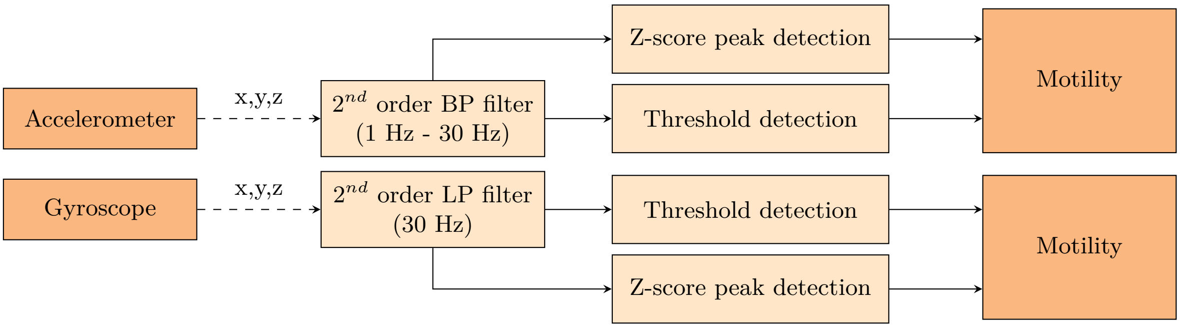

Figure 8-1: Processing pipelines stomach motility detection.

8-1-2 Investigating Alternative Sensor Fusion Techniques

The current design of our sensor system employs the Madgwick filter for estimating the device's orientation. Although this method has demonstrated effectiveness and computational efficiency, a more rigorous approach that accounts for the error characteristics and provides deeper insight into the system's performance may be advantageous. One such alternative is the exploration of Kalman-based methods, which have garnered considerable attention in the field of sensor fusion, specifically in the context of complex and uncertain systems.

Two well-established variants of the Kalman filter, the Extended Kalman Filter (EKF) and the Unscented Kalman Filter (UKF), are known for their adaptability to non-linear systems and have found applications in numerous domains, including quaternion-based orientation estimation [75]. A key strength of these methods lies in their ability to optimally estimate system states, taking into account both process and measurement noise, given accurate modeling of the system's dynamics and uncertainties. Moreover, the added advantage of quantifying the associated uncertainties allows for a more informed evaluation of the system's reliability and the potential for refining the decision making process.

It is worth noting that implementing Kalman-based methods typically involves greater computational demands and more precise modeling of the system's dynamics and noise characteristics compared to the Madgwick filter [67]. Nevertheless, the prospect of enhanced estimation accuracy and a deeper understanding of error characteristics may outweigh the increased complexity.

For future work, it would be valuable to assess the feasibility and performance of EKF and UKF techniques for orientation estimation within the context of the proposed ingestible device. This investigation should entail a comparison between these advanced methods and the Madgwick filter in terms of estimation accuracy, computational requirements, and implementation challenges. From these, we can then determine the most appropriate sensor fusion technique for our orientation estimation.

8-1-3 Distributing the IMU's Computational Load

An alternative approach to computing the quaternions from raw IMU estimates would involve directly obtaining quaternion outputs from the IMU and feeding them to the microcontroller unit (MCU). This method could offload some of the computational steps associated with quaternion conversion to the IMU, potentially reducing the processing load on the MCU.

In our current design, we did not pursue this approach due to concerns about introducing new complexities and potentially compromising the system's flexibility. Nevertheless, future research could explore the potential benefits of distributing the computational load more evenly between the IMU and the MCU.

8-1-4 Alternative Motor Tracking Methods

The inertial measurement unit (IMU) utilizes gravity to determine the capsule's orientation. To ascertain whether the capsule is open or closed, a magnet can be employed on one arm, with the IMU determining the arms' angle. This is achieved by monitoring the angular change of the magnetic field, which corresponds to the arm's angle. The IMU is positioned in the center of the Kirigami PCB on the bottom side. Another possibility for tracking motor rotations or arm angles is the use of a microphone. However, during testing, the microphone approach proved to be challenging and only functioned with a bulge as an inhomogeneity in a round disk lying on a plate to generate an acoustic signal. Another tested alternative was analyzing the motor's power consumption to determine the rotation speed, which only worked with inhomogeneities. The three possibilities—magnets, microphones, and current measurements—can be evaluated using the prototypes.

8-2 Recommendations for Future Research on Controllable Gastric Retention and Injection

8-2-1 Miniaturizing the Reorientation and Injection Mechanism

The current prototype, equipped with the 700GR motor, has dimensions of 12mm in diameter and 40.88mm in length. The largest commercially available drug-loading capsule is size 000, with dimensions of 26.1mm in length and 9.91mm in diameter. The largest ingestible device, the PillCam, measures 11mm in diameter and 26mm in length, but it is utilized by physicians and not autonomously [76]

A primary challenge in our system is the direct current (DC) motor's length, which totals 21mm when the rod is included. As mentioned in Chapter 5, the 136 gear ratio motor can also overcome the mechanism's torque, but this would only result in a 2mm reduction in length. Therefore, we should explore alternative actuation methods: 1) changing the motor and 2) changing the mechanism.

One option for a smaller motor that can still deliver the necessary power is the brushless DC motor. Similar to the brushed DC motor used in our system, brushless DC motors offer high controllability and low-voltage operation while being smaller in size. This search could be extended to brushless DC flat motors; however, the applicable torque or motor width could pose challenges. This approach would again require the motor's parameterization.

Alternatively, we could investigate different retention and injection mechanisms. In our literature review in Section 2-1-2, we highlighted several other types of retention mechanisms. One alternative idea could involve using a passive retention system and making only the actuator system active. The main challenge here would be guaranteeing correct injection. Therefore, such a system would need to be incorporated with different drug delivery systems, such as the free release of nanocarriers. However, this approach would result in slower absorption times.

8-2-2 Alternative Macromolecule Drug Delivery Methods

While the injection-based drug delivery method offers fast delivery, it limits the system to a single delivery and has relatively low efficacy. Alternative drug delivery methods could potentially overcome these limitations and improve the overall performance of the device.

One such method is jet injection, in which a fluid containing the medicine is pushed out of the system at very high pressure to facilitate passage through the gastric wall. Jet injection has been successfully incorporated into the self-orienting millimeter-scale applicator (SOMA) device, which initially inspired our design [77]. This approach has been shown to lead to even higher efficacy rates than traditional injection methods.

In addition to jet injection, several novel drug delivery methods have been proposed in the literature. For example, Byrne and collaborators [18] presented an overview of the physical modes of drug delivery to the GI tract, as illustrated in Figure 8-2. Although many of these methods are still in the early stages of development, they offer potential advantages such as dosage control or even repeated drug delivery.

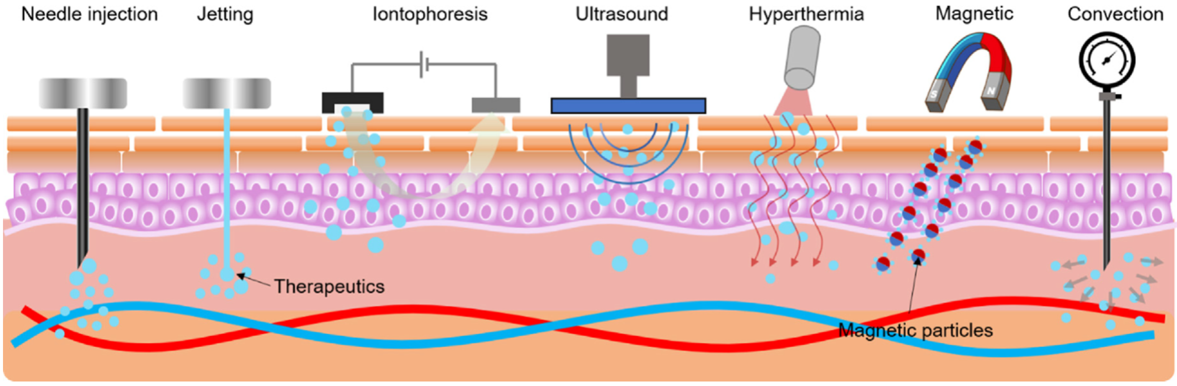

Figure 8-2: Overview of the physical modes of drug delivery to the GI tract [18].

Incorporating methods such as iontophoresis, ultrasound, hyperthermia, magnetic, and convection-based drug delivery could pave the way for tailored gastric drug delivery and potentially enable closed-loop drug therapy. Future design research could focus on investigating the feasibility of implementing these alternative drug delivery methods.

8-2-3 Alternative Applications of the Actuator Energy Optimization Model

In Section 5-3-3, we presented an algorithm that actively adjusts the motor output voltage as the direct current to direct current (DC-DC) converter input voltage changes. Although this algorithm is simple, our literature review on energy optimization of DC geared motor systems revealed that no previous studies have incorporated such a model.

This model could be easily adopted for applications beyond ingestible devices, particularly in battery-powered systems where power supply to DC actuator systems is not the main concern. The impact of actuator model optimization would be even more significant in systems with continuous actuator operation, as opposed to the single operation in our system.

An example of such a system is portable closed-loop drug delivery pump systems like in artificial pancreas devices, where energy consumption is also a concern and motor pump speed is not the primary focus [78]. Further research on the actuator energy optimization model is needed to better understand its potential applications and benefits. In particular, future work could focus on validating the model in systems with continuous actuator use. Also, the system should be tested for various microactuator systems other than DC geared motors.

8-2-4 Injection Angle and Drug Efficacy

During the definition of the design objectives for the actuator system, we investigated the relationship between injection angle error and drug efficacy. Unfortunately, we were unable to find any literature addressing this specific topic. To better validate the feasibility of our system, we need to understand the point at which drug efficacy declines due to the injection angle. We recommend conducting a study on the relationship between injection angles and drug efficacy in gastric injections. This research would help in the design of more effective and safe devices.

8-2-5 In-Vivo Mechanism Testing

Although the injection system has been evaluated using swine stomach tissue, the reorientation mechanism has only been tested outside the body on flat surfaces. To ensure the reliability and performance of the reorientation system, future research should focus on in-vivo testing. Additionally, we should test the injection functionality after achieving the standing position.

In our current design, we estimated a total of 8 reorientation trials before passing the 5-minute window critical for urgent conditions such as anaphylaxis. By taking a deeper look into the reliability of the reorientation and injection mechanism we can better determine the feasibility of achieving the required response time.

8-3 Recommendations for Future Research in Decision Making

8-3-1 Completing the Decision Making Model

Due to time constraints and the incomplete printed circuit board (PCB), we were unable to perform real tests with the leg system. Further experimentation is necessary to pick the parameters for the threshold for fall detection. Similarly, the other thresholds of the system should be adjusted according to the full design. For the battery voltage threshold, we should further look into battery attenuation and the energy consumption folding in the leg system. The gamma detection threshold should be updated according to in-vivo test data and testing with weaker gamma sources.

8-3-2 Fall Detection and Reorientation Control

It may be worth considering alternative approaches to the reorientation process. For instance, full unfolding of the legs may not be necessary, and partial unfolding could suffice. This strategy might save energy and reduce the risk of unwanted stomach exits. Future research should explore different reorientation strategies to determine the most effective and efficient method for the device's reorientation.

8-3-3 Energy Consumption

From our energy estimation in Section 7-2, we deduced that the operation lifetime is mainly determined by the energy consumption during low power mode. Herein, the availability of a sleep mode allowed us to keep the energy consumption low in between sensor updates. Consequently, the energy consumption during low power mode is mainly determined by the sensor update interval. Here it would be interesting to further explore the needs for the gamma detection update interval, such that we can tailor it to the needs of the patient and the wanted operation time of the device. Unrelated to the decision making system, we could also look into alternatives for our most energy-hungry components: the MCU and gamma sensor LED.

8-4 General Recommendations for Future Research

8-4-1 Injection Location

Despite improved accuracy through calibration, the estimation is still solely based on the capsule's orientation, meaning that the device's orientation within the human body remains uncertain. For example, the exact location of the capsule's injection within the stomach is unknown. To address this issue, it may be beneficial to consider incorporating wearable components that provide feedback on the user's orientation. Alternatively, researchers could explore other methods for orientation tracking with respect to the user's stomach, such use the cameras to localize itself with regards to the stomach wall [79].

8-4-2 Accounting for Body Temperature

Temperature can significantly impact various control system components, such as the IMU sensors, the DC-DC converter, the motor, and the battery. In the current study, all estimations and tests have been conducted at room temperature. However, the device is intended to operate in a gastric environment at body temperature (approximately 37 degrees Celsius) To improve the performance of the system, future models should adjust the estimations to account for temperature discrepancies.

A more advanced approach to temperature compensation could be inspired by the work of Lee and collaborators [80]. Their research involved deriving the battery system for four temperature points, ranging from 37 to 40 degrees Celsius at 1-degree intervals. During operation, the system interpolated between the models based on the current temperature, thus enhancing the overall performance of the device when facing temperature fluctuations. As an alternative to minimize computational load, the system could be designed to optimize performance for the nearest whole degree.

8-4-3 Identification of the Target Audience

For a more effective design, we should identify the target audience of the ingestible device and tailor it to their specific needs. Several potential audiences to consider include:

- Military personnel, who may be at risk of exposure to radioactive material during active service or training exercises.
- Workers in extreme situations, such as those involved in cleanup operations after nuclear disasters like Fukushima or Chornobyl, where they may face exposure to nuclear fallout zones.
- Employees at nuclear facilities, where they work in environments with strong nuclear forces that are shielded, making them prone to potential exposure.
- Medical professionals who work in environments with weak, unshielded nuclear forces, such as those who regularly operate X-ray machines or handle radioactive materials for medical imaging and therapy.

8-4-4 Expanding Applications Beyond Urgent Care

Although many components of the proposed ingestible device are designed specifically for gamma radiation detection and treatment, the device shows potential for use in various other scenarios where detection from the stomach could be beneficial. Some potential applications include:

- Detection and treatment of food allergies
- Detection and treatment of poisoning

In addition to immediate detection, the device's proximity to the heart and lungs allows for monitoring of physiological status, which can aid in the detection and treatment of specific conditions. For instance, a microphone could be employed to measure respiratory and heart rates from the stomach [16]. Potential applications in this area include:

- Detection and treatment of asthma exacerbations
- Detection and treatment of opioid overdoses
- Detection and treatment of cardiac arrhythmias
- Detection and treatment of acute epileptical insults

References

[1] M. S. Shaker *et al.*, "Anaphylaxis—a 2020 practice parameter update, systematic review, and Grading of Recommendations, Assessment, Development and Evaluation (GRADE) analysis", *Journal of Allergy and Clinical Immunology*, vol. 145, no. 4, pp. 1082–1123, 2020, ISSN: 10976825. DOI: 10.1016/j.jaci.2020.01.017. [Online]. Available: https://doi.org/10.1016/j.jaci.2020.01.017.

[2] M. Eddleston, N. A. Buckley, P. Eyer, and A. H. Dawson, "Management of acute organophosphorus pesticide poisoning", *The Lancet*, vol. 371, no. 9612, pp. 597–607, 2008, ISSN: 01406736. DOI: 10.1016/S0140-6736(07)61202-1.

[3] N. P. Clayton *et al.*, "Sargramostim (rhu GM-CSF) improves survival of non-human primates with severe bone marrow suppression after acute, high-dose, whole- body irradiation", *Radiation Research*, vol. 195, no. 2, pp. 191–199, Feb. 2021, ISSN: 19385404. DOI: 10.1667/RADE-20-00131.1. [Online]. Available: https://pubmed.ncbi.nlm.nih.gov/33302291/.

[4] E. W. Boyer, "Management of Opioid Analgesic Overdose", *New England Journal of Medicine*, vol. 367, no. 2, pp. 146–155, Jul. 2012, ISSN: 0028-4793. DOI: 10.1056/nejmra1202561. [Online]. Available: https://www.nejm.org/doi/full/10.1056/NEJMra1202561.

[5] B. Pintaudi *et al.*, "Minimed Medtronic 780G optimizes glucose control in patients with type 1 diabetes mellitus", *Nutrition, Metabolism and Cardiovascular Diseases*, vol. 32, no. 7, pp. 1719–1724, Jul. 2022, ISSN: 15903729. DOI: 10.1016/j.numecd.2022.03.031.

[6] J. Tang *et al.*, "Seizure detection using wearable sensors and machine learning: Setting a benchmark", *Epilepsia*, vol. 62, no. 8, pp. 1807–1819, Aug. 2021, ISSN: 15281167. DOI: 10.1111/epi.16967. [Online]. Available: https://pubmed.ncbi.nlm.nih.gov/34268728/.

[7] Jyoti, E. Redondo, O. Alduhaish, and M. Pumera, "3D-printed Electrochemical Sensor for Organophosphate Nerve Agents", *Electroanalysis*, vol. 35, no. 1, e202200047, Jan. 2023, ISSN: 15214109. DOI: 10.1002/elan.202200047. [Online]. Available: https://onlinelibrary.wiley.com/doi/full/10.1002/elan.202200047%20https:

//onlinelibrary.wiley.com/doi/abs/10.1002/elan.202200047%20https://analyticalsciencejournals.onlinelibrary.wiley.com/doi/10.1002/elan.202200047.

[8] Y. Inaba, M. Nakamura, M. Zuguchi, and K. Chida, "Development of novel real-time radiation systems using 4-channel sensors", *Sensors (Switzerland)*, vol. 20, no. 9, p. 2741, May 2020, ISSN: 14248220. DOI: 10.3390/s20092741. [Online]. Available: https://www.mdpi.com/1424-8220/20/9/2741/htm%20https://www.mdpi.com/1424-8220/20/9/2741.

[9] A. R. Syaifudin *et al.*, "Measurements and performance evaluation of novel interdigital sensors for different chemicals related to food poisoning", *IEEE Sensors Journal*, vol. 11, no. 11, pp. 2957–2965, 2011, ISSN: 1530437X. DOI: 10.1109/JSEN.2011.2154327.

[10] *Surgeons Need to Know the Cost of Implants Despite Veil of Secrecy in Healthcare - OptioSurgical*. [Online]. Available: https://optiosurgical.com/surgeons-need-to-know-implant-cost/.

[11] C. Steiger, A. Abramson, P. Nadeau, A. P. Chandrakasan, R. Langer, and G. Traverso, "Ingestible electronics for diagnostics and therapy", *Nature Reviews Materials*, vol. 4, no. 2, pp. 83–98, Dec. 2019, ISSN: 20588437. DOI: 10.1038/s41578-018-0070-3. [Online]. Available: https://www-nature-com.tudelft.idm.oclc.org/articles/s41578-018-0070-3.

[12] H. I. Works, K. Diseases, R. C. Trials, and T. Gi, *Your Digestive System and How It Works*, 2015. [Online]. Available: https://www.niddk.nih.gov/health-information/digestive-diseases/digestive-system-how-it-works%0Ahttps://www.niddk.nih.gov/health-information/digestive-diseases/digestive-system-how-it-works#food#.

[13] A. Perkins, "Life and Death Rays: Radioactive Poisoning and Radiation Exposure", *Life and Death Rays: Radioactive Poisoning and Radiation Exposure*, pp. 1–230, 2021. DOI: 10.1201/9781003028246.

[14] J. Min, Y. Yang, Z. Wu, and W. Gao, "Robotics in the Gut", *Advanced Therapeutics*, vol. 3, no. 4, 2020, ISSN: 23663987. DOI: 10.1002/adtp.201900125.

[15] M. M. Mau, S. Sarker, and B. S. Terry, "Ingestible devices for long-term gastrointestinal residency: A review", *Progress in Biomedical Engineering*, vol. 3, no. 4, p. 042 001, Aug. 2021, ISSN: 25161091. DOI: 10.1088/2516-1091/ac1731. [Online]. Available: https://iopscience.iop.org/article/10.1088/2516-1091/ac1731%20https://iopscience.iop.org/article/10.1088/2516-1091/ac1731/meta.

[16] G. Traverso *et al.*, "Physiologic status monitoring via the gastrointestinal tract", *PLoS ONE*, vol. 10, no. 11, pp. 1–13, 2015, ISSN: 19326203. DOI: 10.1371/journal.pone.0141666.

[17] C. Won, C. Kwon, K. Park, J. Seo, and T. Lee, "Electronic Drugs: Spatial and Temporal Medical Treatment of Human Diseases", *Advanced Materials*, vol. 33, no. 47, p. 2 005 930, Nov. 2021, ISSN: 15214095. DOI: 10.1002/adma.202005930. [Online]. Available: https://onlinelibrary.wiley.com/doi/full/10.1002/adma.202005930%20https://onlinelibrary.wiley.com/doi/abs/10.1002/adma.202005930%20https://onlinelibrary.wiley.com/doi/10.1002/adma.202005930.

[18] J. Byrne *et al.*, "Devices for drug delivery in the gastrointestinal tract: A review of systems physically interacting with the mucosa for enhanced delivery", *Advanced Drug Delivery Reviews*, vol. 177, p. 113 926, 2021, ISSN: 18728294. DOI: 10.1016/j.addr.2021.113926. [Online]. Available: https://doi.org/10.1016/j.addr.2021.113926.

[19] M. F. Melum and K. Kearney, "Organophosphate toxicity", *American Journal of Nursing*, vol. 101, no. 5, pp. 57–58, May 2001, ISSN: 0002936X. DOI: 10.1097/00000446-200105000-00021. [Online]. Available: https://www.ncbi.nlm.nih.gov/books/NBK470430/%20http://www.pubmedcentral.nih.gov/articlerender.fcgi?artid=PMC6387473.

[20] S. H. Sicherer *et al.*, "Epinephrine for first-aid management of anaphylaxis", *Pediatrics*, vol. 139, no. 3, Mar. 2017, ISSN: 10984275. DOI: 10.1542/peds.2016-4006. [Online]. Available: /pediatrics/article/139/3/e20164006/53753/Epinephrine-for-First-aid-Management-of%20https://publications.aap.org/pediatrics/article/139/3/e20164006/53753/Epinephrine-for-First-aid-Management-of.

[21] G. Cummins, "Smart pills for gastrointestinal diagnostics and therapy", *Advanced Drug Delivery Reviews*, vol. 177, p. 113 931, Oct. 2021, ISSN: 18728294. DOI: 10.1016/j.addr.2021.113931.

[22] *Insight - loop mode | Nederland*. [Online]. Available: https://www.accu-chek.nl/insight-loop.

[23] D. Becker *et al.*, "Novel Orally Swallowable IntelliCap®Device to Quantify Regional Drug Absorption in Human GI Tract Using Diltiazem as Model Drug", *Ageing International*, vol. 15, no. 6, pp. 1490–1497, Nov. 2014, ISSN: 1936606X. DOI: 10.1208/S12249-014-0172-1/FIGURES/10. [Online]. Available: https://link.springer.com/article/10.1208/s12249-014-0172-1.

[24] T. R. Zijp, D. J. Touw, and J. F. van Boven, "User acceptability and technical robustness evaluation of a novel smart pill bottle prototype designed to support medication adherence", *Patient Preference and Adherence*, vol. 14, pp. 625–634, 2020, ISSN: 1177889X. DOI: 10.2147/PPA.S240443. [Online]. Available: https://www.tandfonline.com/action/journalInformation?journalCode=dppa20.

[25] A. M. Bellinger *et al.*, "Oral, ultra-long-lasting drug delivery: Application toward malaria elimination goals", *Science Translational Medicine*, vol. 8, no. 365, 2016, ISSN: 19466242. DOI: 10.1126/scitranslmed.aag2374.

[26] N. Navon, "The Accordion Pill®: unique oral delivery to enhance pharmacokinetics and therapeutic benefit of challenging drugs", *Therapeutic delivery*, vol. 10, no. 7, pp. 433–443, 2019, ISSN: 2041-6008. DOI: 10.4155/TDE-2018-0067. [Online]. Available: https://pubmed.ncbi.nlm.nih.gov/31203723/.

[27] A. Melocchi *et al.*, "Expandable drug delivery system for gastric retention based on shape memory polymers: Development via 4D printing and extrusion", *International journal of pharmaceutics*, vol. 571, Nov. 2019, ISSN: 1873-3476. DOI: 10.1016/J.IJPHARM.2019.118700. [Online]. Available: https://pubmed.ncbi.nlm.nih.gov/31526838/.

[28] A. Abramson *et al.*, "An ingestible self-orienting system for oral delivery of macromolecules", *Science*, vol. 363, no. 6427, pp. 611–615, Feb. 2019, ISSN: 10959203. DOI: 10.1126/science.aau2277. [Online]. Available: https://www.science.org/doi/abs/10.1126/science.aau2277%20https://www.science.org/doi/10.1126/science.aau2277.

[29] S. Murdan, "Electro-responsive drug delivery from hydrogels", *Journal of Controlled Release*, vol. 92, no. 1-2, pp. 1–17, Sep. 2003, ISSN: 0168-3659. DOI: 10.1016/S0168-3659(03)00303-1.

[30] Y. Xu, N. Shrestha, V. Préat, and A. Beloqui, "Overcoming the intestinal barrier: A look into targeting approaches for improved oral drug delivery systems", *Journal of Controlled Release*, vol. 322, pp. 486–508, Jun. 2020, ISSN: 18734995. DOI: 10.1016/j.jconrel.2020.04.006.

[31] *Capsule Size Guide | Interactive Specification Chart*. [Online]. Available: https://www.lfacapsulefillers.com/capsule-size-chart.

[32] S. Y. Yang *et al.*, "Powering Implantable and Ingestible Electronics", *Advanced Functional Materials*, vol. 31, no. 44, p. 2 009 289, 2021, ISSN: 16163028. DOI: 10.1002/adfm.202009289. [Online]. Available: https://onlinelibrary-wiley-com.tudelft.idm.oclc.org/doi/full/10.1002/adfm.202009289.

[33] I.-M. Chen, S. Jay PHEE, Z. Luo, and C. Kian LIM, "Personalized biomedical devices & systems for healthcare applications", DOI: 10.1007/s11465-011-0209-z.

[34] G. M. Eisen *et al.*, "Complications of upper GI endoscopy.", *Gastrointestinal endoscopy*, vol. 55, no. 7, pp. 784–793, 2002, ISSN: 00165107. DOI: 10.1016/S0016-5107(02)70404-5. [Online]. Available: https://pubmed.ncbi.nlm.nih.gov/12024128/.

[35] I. P. Vazharov, "Perforation As a Complication of the Diagnostic Upper and Lower Endoscopy of the Gastrointestinal Tract", *Journal of IMAB - Annual Proceeding (Scientific Papers)*, vol. 18, 3, no. 2012, pp. 273–275, 2012. DOI: 10.5272/jimab.2012183.273.

[36] A. Chevance *et al.*, "Acceptability of and Willingness to Take Digital Pills by Patients, the Public, and Health Care Professionals: Qualitative Content Analysis of a Large Online Survey", *Journal of Medical Internet Research*, vol. 24, no. 2, e25597, Feb. 2022, ISSN: 14388871. DOI: 10.2196/25597. [Online]. Available: https://www.jmir.org/2022/2/e25597.

[37] B. Perry *et al.*, "Patient preferences for using mobile technologies in clinical trials", *Contemporary Clinical Trials Communications*, vol. 15, p. 100 399, Sep. 2019, ISSN: 24518654. DOI: 10.1016/j.conctc.2019.100399.

[38] C. Vaz *et al.*, "Formative acceptance of ingestible biosensors to measure adherence to TB medications", *BMC Infectious Diseases*, vol. 22, no. 1, pp. 1–11, Dec. 2022, ISSN: 14712334. DOI: 10.1186/s12879-022-07756-x. [Online]. Available: https://link.springer.com/articles/10.1186/s12879-022-07756-x%20https://link.springer.com/article/10.1186/s12879-022-07756-x.

[39] F. Forma, K. Chiu, J. Shafrin, D. H. Boskovic, and S. P. Veeranki, "Are caregivers ready for digital? Caregiver preferences for health technology tools to monitor medication adherence among patients with serious mental illness", *Digital Health*, vol. 8, 2022, ISSN: 20552076. DOI: 10.1177/20552076221084472. [Online]. Available: https://us.sagepub.com/en-us/nam/.

[40] C. M. Klugman, L. B. Dunn, J. Schwartz, and I. G. Cohen, "The Ethics of Smart Pills and Self-Acting Devices: Autonomy, Truth-Telling, and Trust at the Dawn of Digital Medicine", *American Journal of Bioethics*, vol. 18, no. 9, pp. 38–47, Sep. 2018, ISSN: 15360075. DOI: 10.1080/15265161.2018.1498933. [Online]. Available: https://www.tandfonline.com/doi/abs/10.1080/15265161.2018.1498933.

[41] M. Aldeer, M. Javanmard, and R. P. Martin, "A review of medication adherence monitoring technologies", *Applied System Innovation*, vol. 1, no. 2, pp. 1–27, May 2018, ISSN: 25715577. DOI: 10.3390/asi1020014. [Online]. Available: https://www.mdpi.com/2571-5577/1/2/14/htm%20https://www.mdpi.com/2571-5577/1/2/14.

[42] A. Dodd, A. Hughes, N. Sargant, A. F. Whyte, J. Soar, and P. J. Turner, "Evidence update for the treatment of anaphylaxis", *Resuscitation*, vol. 163, p. 86, Jun. 2021, ISSN: 18731570. DOI: 10.1016/J.RESUSCITATION.2021.04.010. [Online]. Available: /pmc/articles/PMC8139870/%20/pmc/articles/PMC8139870/?report=abstract%20https://www.ncbi.nlm.nih.gov/pmc/articles/PMC8139870/.

[43] C. Langhans, *PIN Photodiode – a,b,y Radiation Sensor*, 2015.

[44] *Gammamikrofon*. [Online]. Available: https://www.b-kainka.de/bastel131.html.

[45] *Motion basics: How to define roll, pitch, and yaw for linear systems.* [Online]. Available: https://www.linearmotiontips.com/motion-basics-how-to-define-roll-pitch-and-yaw-for-linear-systems/.

[46] I. M. Unit, "IMU Errors and Their Effects. Report APN-064 (Rev A)", pp. 1–6, 2014. [Online]. Available: http://www.novatel.com/assets/Documents/Bulletins/APN064.pdf.

[47] V. M. Passaro, A. Cuccovillo, L. Vaiani, M. De Carlo, and C. E. Campanella, "Gyroscope technology and applications: A review in the industrial perspective", *Sensors (Switzerland)*, vol. 17, no. 10, Oct. 2017, ISSN: 14248220. DOI: 10.3390/s17102284. [Online]. Available: /pmc/articles/PMC5677445/%20/pmc/articles/PMC5677445/?report=abstract%20https://www.ncbi.nlm.nih.gov/pmc/articles/PMC5677445/.

[48] H. Fourati and D. E. C. Belkhiat, "Multisensor attitude estimation: Fundamental concepts and applications", *Multisensor Attitude Estimation: Fundamental Concepts and Applications*, no. June, pp. 1–580, 2016. DOI: 10.1201/9781315368795.

[49] Bosch, "BMX160 - small , low power 9-axis sensor Datasheet", pp. 1–113, 2019. [Online]. Available: https://ae-bst.resource.bosch.com/media/_tech/media/datasheets/BST-BMX160-DS000.pdf.

[50] BOSCH, *Datasheet - sensor BNO055*, 2021. [Online]. Available: https://www.bosch-sensortec.com/media/boschsensortec/downloads/datasheets/bst-bno055-ds000.pdf.

[51] T. D. K. InvenSense, "ICM-20948: World's Lowest Power 9-Axis MEMS MotionTracking Device", *URl: https://invensense. tdk. com/wp-content/uploads/2016/06/DS-000189-ICM-20948-v1*, vol. 3, pp. 1–89, 2017. [Online]. Available: `http://www.invensense.com/wp-content/uploads/2016/06/DS-000189-ICM-20948-v1.3.pdf`.

[52] L. Ada, "Adafruit INA219 Current Sensor Breakout", *Adafruit learning system*, pp. 1–28, 2015. [Online]. Available: `https://learn.adafruit.com/adafruit-ina219-current-sensor-breakout`.

[53] Nordic Semiconductor, "Datasheet: nRF52840 Product Specification V1.1", vol. v1.7, pp. 21–22, 2018, ISSN: 0961-3218.

[54] R. Pereira *et al.*, "Energy efficiency across programming languages: How do energy, time, and memory relate?", *SLE 2017 - Proceedings of the 10th ACM SIGPLAN International Conference on Software Language Engineering, co-located with SPLASH 2017*, pp. 256–267, 2017. DOI: `10.1145/3136014.3136031`. [Online]. Available: `https://doi.org/10.1145/3136014.3136031`.

[55] *US20220142566A1 - Closed-loop detection and treatment of radiation and toxic agents - Google Patents*. [Online]. Available: `https://patents.google.com/patent/US20220142566A1/en`.

[56] *Standard Of Machine Screw Pitch and Thread Rolling Blank Diameter and.* [Online]. Available: `https://ever-hardware.com/standard-of-machine-screw-pitch-and-thread.html`.

[57] *Bolt Depot - Metric Nut Size Table - Diameter and Height.* [Online]. Available: `https://www.boltdepot.com/fastener-information/nuts-washers/Metric-Nut-Dimensions.aspx`.

[58] *Pololu - 700:1 Sub-Micro Plastic Planetary Gearmotor 6Dx21L mm.* [Online]. Available: `https://www.pololu.com/product/2359`.

[59] IOLITEC, C. Properties, and T. Properties, *Technical data sheet Technical data sheet [C4MIM][NTf2]*, 2005.

[60] *365 Renata Batteries | Battery Products | DigiKey Marketplace.* [Online]. Available: `https://www.digikey.com/en/products/detail/micropower-battery-company/365/16529321`.

[61] D. Linden and T. B. Reddy, *Handbook of Batteries. 4th.* McGraw-Hill Education, 2010, p. 1200, ISBN: 0071624198. [Online]. Available: `https://www.accessengineeringlibrary.com/content/book/9780071624213`.

[62] C. A. Vincent, "Lithium batteries: A 50-year perspective, 1959-2009", *Solid State Ionics*, vol. 134, no. 1-2, pp. 159–167, Oct. 2000, ISSN: 01672738. DOI: `10.1016/S0167-2738(00)00723-2`. [Online]. Available: `www.elsevier.com/locate/ssiLithiumbatteries:a50-yearperspective,1959-2009`.

[63] J. T. Jang, A. Santamaria-Navarro, B. T. Lopez, and A. A. Agha-Mohammadi, "Analysis of State Estimation Drift on a MAV Using PX4 Autopilot and MEMS IMU during Dead-reckoning", *IEEE Aerospace Conference Proceedings*, Mar. 2020, ISSN: 1095323X. DOI: `10.1109/AERO47225.2020.9172736`.

[64] J. Diebel, "Representing Attitude: Euler Angles, Unit Quaternions, and Rotation Vectors", 2006.

[65] L. Wang, Z. Zhang, and P. Sun, “Quaternion-Based Kalman Filter for AHRS Using an Adaptive-Step Gradient Descent Algorithm”, *International Journal of Advanced Robotic Systems*, vol. 12, no. 9, 2015, ISSN: 17298814. DOI: 10.5772/61313.

[66] R. Mahony, T. Hamel, and J. M. Pflimlin, “Complementary filter design on the special orthogonal group SO(3)”, *Proceedings of the 44th IEEE Conference on Decision and Control, and the European Control Conference, CDC-ECC ’05*, vol. 2005, pp. 1477–1484, 2005. DOI: 10.1109/CDC.2005.1582367.

[67] S. O. Madgwick, A. J. Harrison, and R. Vaidyanathan, *Estimation of IMU and MARG orientation using a gradient descent algorithm.* 2011, ISBN: 9781424498628. DOI: 10.1109/ICORR.2011.5975346.

[68] S. A. Ludwig, K. D. Burnham, A. R. Jiménez, and P. A. Touma, “Comparison of Attitude and Heading Reference Systems using Foot Mounted MIMU Sensor Data: Basic, Madgwick and Mahony”,

[69] M. Ehrgott, *Multicriteria optimization.* 2005, ISBN: 3540213988. [Online]. Available: https://books.google.com/books?hl=en&lr=&id=8wGyB5Sa2CUC&oi=fnd&pg=PA1&ots=ag3IDY-pgW&sig=vLt2EzUog97XZobHPCAGdvBiN_w.

[70] N. Gunantara, “A review of multi-objective optimization: Methods and its applications”, *http://www.editorialmanager.com/cogenteng*, vol. 5, no. 1, pp. 1–16, Jan. 2018, ISSN: 23311916. DOI: 10.1080/23311916.2018.1502242. [Online]. Available: https://www.tandfonline.com/doi/abs/10.1080/23311916.2018.1502242.

[71] T. Verstraten, R. Furnemont, G. Mathijssen, B. Vanderborght, and D. Lefeber, “Energy Consumption of Geared DC Motors in Dynamic Applications: Comparing Modeling Approaches”, *IEEE Robotics and Automation Letters*, vol. 1, no. 1, pp. 524–530, Jan. 2016, ISSN: 23773766. DOI: 10.1109/LRA.2016.2517820.

[72] D. J. Griffiths and C. Inglefield, “ Introduction to Electrodynamics ”, *American Journal of Physics*, vol. 73, no. 6, pp. 574–574, 2005, ISSN: 0002-9505. DOI: 10.1119/1.4766311.

[73] J.-F. Raskin, “An Introduction to Hybrid Automata”,

[74] R. Alur and D. L. Dill, “A theory of timed automata”, *Theoretical Computer Science*, vol. 126, no. 2, pp. 183–235, Apr. 1994, ISSN: 0304-3975. DOI: 10.1016/0304-3975(94)90010-8.

[75] P. Bernal-Polo and H. Martínez-Barberá, “Kalman Filtering for Attitude Estimation with Quaternions and Concepts from Manifold Theory”, *Sensors (Basel, Switzerland)*, vol. 19, no. 1, Jan. 2019, ISSN: 14248220. DOI: 10.3390/S19010149. [Online]. Available: /pmc/articles/PMC6339217/%20/pmc/articles/PMC6339217/?report=abstract%20https://www.ncbi.nlm.nih.gov/pmc/articles/PMC6339217/.

[76] S. N. Adler and Y. C. Metzger, “PillCam COLON capsule endoscopy: Recent advances and new insights”, *Therapeutic Advances in Gastroenterology*, vol. 4, no. 4, pp. 265–268, Jul. 2011, ISSN: 17562648. DOI: 10.1177/1756283X11401645. [Online]. Available: http://www.pubmedcentral.nih.gov/articlerender.fcgi?artid=PMC3131168.

[77] A. Abramson *et al.*, “Oral delivery of systemic monoclonal antibodies, peptides and small molecules using gastric auto-injectors”, *Nature Biotechnology 2021 40:1*, vol. 40, no. 1, pp. 103–109, Aug. 2021, ISSN: 1546-1696. DOI: 10.1038/s41587-021-01024-0. [Online]. Available: https://www.nature.com/articles/s41587-021-01024-0.

[78] F. H. El-khatib, S. J. Russell, D. M. Nathan, R. G. Sutherlin, and E. R. Damiano, "A bihormonal closed-loop artificial pancreas for type 1 diabetes", *Science Translational Medicine*, vol. 2, no. 27, Apr. 2010, ISSN: 19466242. DOI: 10.1126/scitranslmed.3000619. [Online]. Available: https://www.science.org/doi/10.1126/scitranslmed.3000619.

[79] S. S. Vedaei and K. A. Wahid, "A localization method for wireless capsule endoscopy using side wall cameras and IMU sensor", *Scientific Reports*, vol. 11, no. 1, May 2021, ISSN: 20452322. DOI: 10.1038/s41598-021-90523-w. [Online]. Available: https://www-nature-com.tudelft.idm.oclc.org/articles/s41598-021-90523-w.

[80] K. T. Lee, M. J. Dai, and C. C. Chuang, "Temperature-Compensated Model for Lithium-Ion Polymer Batteries With Extended Kalman Filter State-of-Charge Estimation for an Implantable Charger", *IEEE Transactions on Industrial Electronics*, vol. 65, no. 1, pp. 589–596, Jan. 2018, ISSN: 02780046. DOI: 10.1109/TIE.2017.2721880.

Glossary

List of Acronyms

AC	alternating current
DC	direct current
DC-DC	direct current to direct current
DOF	degrees of freedom
ED	emergency department
FDA	United States Food and Drug Administration
GI	gastrointestinal
GPIO	general-purpose input/output
GR	gear ratio
HMS	Harvard Medical School
I^{2}C	inter-integrated circuit
IMU	inertial measurement unit
I/O	input/output
LIB	lithium-ion battery
MCU	microcontroller unit
MEMS	microelectromechanical systems
MIT	Massachusetts Institute of Technology
MOP	multi-objective optimization problem
PCB	printed circuit board
PWM	pulse width modulation
RAM	random-access memory
RMSE	root-mean-square error
SOB	silver oxide battery
SOMA	self-orienting millimeter-scale applicator
SPI	Serial Peripheral Interface
SMA	shape-memory alloy
TI	Texas Instruments™